Politecnico di Milano
Department of Aerospace Engineering
Doctoral Program in Rotary Wing Aircraft

Design optimization of wind turbines

Doctoral Dissertation of:
Federico Gualdoni

Supervisor:
Prof. Carlo L. Bottasso

Tutor:
Prof. Pierangelo Masarati

The Chair of the Doctoral Program:
Prof. Luigi Vigevano

Year 2014 – XXVII Doctoral Cycle

“Kinderspiele”

Acknowledgments

The interest from the academic field and the industrial subjects has supported the current work, providing relevant advices and verification tools. These significant contributions are really appreciated and they are here acknowledged with gratitude.

This project has been accomplished by the valued help of Dr. D. Todd Griffith of Wind and Water Power Technologies Department at Sandia National Laboratories. The collaborations with Gurit and Leitwind have provided a useful perspective of the industrial methodologies and approaches.

Many of fundamental ideas here reported have been conceived by my supervisor, Prof. Carlo L. Bottasso. Also his colleague Alessandro Croce has had a key role in developing this project, providing a qualified supervision.

Several support activities have been supplied by various master's thesis students, that assisted me in time consuming procedures and support activities.

A special thought goes to my special Cisalpine and Bavarian colleagues, their inestimable help has been an unlimited source of motivation and inspiration.

Vorrei infine ringraziare la mia famiglia e le persone a me vicine per aver condiviso pazientemente le mie difficoltà, aiutandomi nei momenti difficili e condividendo le mie soddisfazioni.

Abstract

This thesis aims at investigating the constrained aero-structural optimization of horizontal axis wind turbines. Various aspects of the design process are presented, focusing on the improvement of the classical configuration but also considering innovative solutions to extend the opportunities of design. The requirements are naturally included by constraint equations, providing feasible configuration at the end of the process. The developed methods are based on a general approach that recreates the real operative conditions. For this reason a high-fidelity simulation environment is employed to evaluate the numerous situations imposed by the international standards, making the reported procedures attractive for industrial applications.

The attention is focused on the design of rotor blades and support tower, that are the most important aero-structural components in terms of cost of energy. The first chapter presents the development and implementation of the aero-structural optimization techniques. At first an introduction to the simulation environment is reported, highlighting the modeling approach shared by all of the procedures. Then the aerodynamic design of rotor blades is considered, showing how the maximization of the annual energy production can be achieved.

Subsequently the optimization of the structural layout of rotor blades and tower is considered, looking for the minimum cost of energy. In order to increase the computational efficiency, a multi-layer method is adopted. The optimization is performed at coarse-level that involves efficient geometrically exact beam models, cross-sectional analyses and multibody techniques. When the optimal configuration is achieved, a refinement can be applied at fine-level by the 3D FE models. The modeling of the CAD geometry, the meshing and the definition of the FEM is a fully automated procedure performed by a dedicated tool. The interaction between the coarse and fine-layer is performed iteratively, by heuristic scaling of design requirements.

Finally the attention is focused on the aero-structural design of the rotor blades. Two innovative algorithms are presented and compared with a tested one. Each method involves different user's participation and computational cost. Each design procedure is validated by meaningful test cases and the pros and cons of each approach are reported. Various test cases are reproduced, looking at different classes of wind turbines that encompass standard industrial applications and future concepts.

At the end, load alleviation capabilities of passive flap are investigated. This element is a passive aeroelastic system appended to the rotor blade. An appropriate tuning of aero-structural properties forces the passive flap with the loads generated by the blade movement. Therefore no additional active components are required, limiting the negative effects on the reliability of the entire wind turbine. Moreover, the passive flap is a distributed mechanism, able to react to localized noise due to the turbulence. Preliminary analyses are performed by simplified models, intending to understand the key parameters that maximize the passive flap effectiveness. The entire operative range is explored, identifying the advantages in term of load alleviation and limiting the interference with the standard wind turbine components.

Contents

Acronyms

1D one-Dimensional

2D two-Dimensional

3D three-Dimensional

AEP Annual Energy Production

AOE Annual Operating Expenses

BEM Blade-Element Momentum

BTC Bend-Twist Coupling

CAD Computer Aided Design

CFD Computational Fluid Dynamic

CLT Classical Lamination Theory

CoE Cost of Energy

DEL Damage Equivalent Load

DLC Dynamic Load Cases

DTU Danmarks Tekniske Universitet

EA Elastic Axis

EAIS External Aerodynamic/Internal Structure

FE Finite Element

FEM Finite Element Model

FCR Fixed Charge Rate

FT Fourier Transform

GL Germanischer Lloyd

HAWT Horizontal Axis Wind Turbine

HL Hinge Line

ICC Initial Capital Cost

IEC International Electrotechnical Commission

IGES Initial Graphics Exchange Specification

LE Leading Edge

LLC Land Lease Cost

LQR Linear Quadratic Regulator

LRC Levelized Replacement Cost

LTI Linear Time Invariant

MB MultiBody

MIMO Multi-Input Multi-Output

MLU Monolithic with Load Updating

MW MegaWatt

NPL Null-Pitch-Line

NREL National Renewable Energy Laboratory

NTM Normal Turbulence Model

NURBS Non-Uniform Rational B-Spline

OH OverHang

PAAS Pre-Assumed Aerodynamic Shape

PID Proportional-Integral-Derivative

QS Quasi-Steady

RWT Reference Wind Turbine

SQP Sequential Quadratic Programming

TE Trailing Edge

WT Wind Turbine

CHAPTER 1

Introduction

Wind energy has been subjected to an exponential growth during the last years, occupying a key role among the various renewable energy systems. The success of the wind turbine is based on different reasons. The first one is the efficiency that turns out to be comparable or superior to the other renewable energy sources. Furthermore the governmental funding in several countries and the positive mood of the public opinion have further incentivized the developing of these technologies, that provides an environmental friendly option to limit the consumption of fossil fuels.

The modern wind turbine is the results of a joint effort between the academic word and the industries. The currently configuration has been achieved by an all-comprehensive research that encompasses all the technologies involved in the today's layout. Aerodynamics, structure, control laws and electrical systems are only some aspects that are interconnected in the complete configuration.

Despite the academic efforts and the success in industrial field, the solution of the optimal design problem of a wind energy system is far to be solved. The multidisciplinarity of the wind turbine and the stochastic nature of the wind make the design process difficult to tackle. The cooperation of various qualified teams is usually required to merge the essential skills to achieve a successful result. Generally, this interaction is performed by successive iterations. This standard approach proves to be uneconomic and time consuming, diverting the attention from the principal objective: the design. Therefore, new methods are required to engineer the wind turbine design process, increasing the efficiency of the entire framework.

This thesis contributes to define new methodologies to solve the optimal aero-structural wind turbine design, aiming at a holistic approach to ensure the achievement of the best performance. The current section will be organized as follow. A simplified description of a typical wind turbine is considered in Sec. 1.1, followed by a review

of the available publications about wind turbine design, Sect. 1.2. The topics and the contributions of the current thesis are reported in Sect. 1.3, while some technical notes are reported in Sect. 1.4.

1.1 Description of a Horizontal Axis Wind Turbine

Essentially, a wind turbine is a system that converts kinetic energy of the wind into electrical energy. Two diagrams that display the topology of a typical Horizontal Axis Wind Turbine (HAWT) are reported in Fig. 1.1 and 1.2, highlighting the main constitutive components.

Figure 1.1: *Wind turbine diagram (source: www.wavege.com)*

The blades and the hub form the rotor assembly, the most important part of wind turbine in term of performance and cost. The rotor with three blades can be considered the most common layout today [1], that is usually adopted in large scale production of electrical energy. This configuration achieves a high efficiency and it ensures a more regular operation than a wind turbine with one or two blades [2].

The blades are usually made by fiber reinforced plastic material such as glass fiber or carbon fiber, exploiting the orthotropic properties of the material to increase the

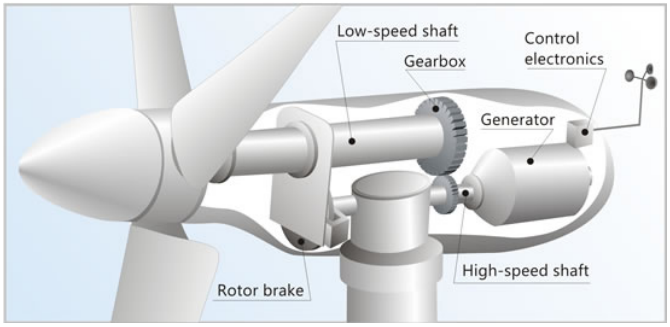

Figure 1.2: *Wind turbine nacelle diagram (source: www.wavege.com)*

performance and to reduce the cost. The hub is linked by a bearing to the structural part of the nacelle, it connects the blades to the generator and it is usually made of steel. The link between the rotor and the generator can be direct or through a gearbox. The first case is defined as direct-drive and it requires specific electrical generator able to produce electrical power at low rotational speed. In the second case a gearbox links the low speed shaft, on the rotor side, to the high speed shaft, on the generator side. The gearbox speeds up the angular velocity of the rotor, around tens rpm, to a value suitable for a standard generator, hundreds of rpm. Therefore the double-shaft configuration allows the use of a standard generator but it requires the installation of extra components, such as the gearbox. In both cases the drive-train has to manage the significant variations of the power input, so it is a critical component of the design. A mechanical brake is installed along the drive train to ease the maintenance of the wind turbine.

The nacelle and the rotor assembly are mounted at the top of the tower. An orientation system is required to align the rotor to the wind direction. The main component is a bearing that allows the relative rotation between the nacelle frame and the tower. The nacelle-tower connection is defined upwind or downwind, depending on the relative position of the rotor assembly and the tower during the operative condition. The upwind configuration is the most common layout for the multi-MegaWatt (MW) machines. It is an unstable solution because the rotor assembly tends to be rotated by the aerodynamic forces in a stable downwind configuration. Therefore this layout requires the installation of one or more yaw motors to point the rotor properly. On the other hand a downwind configuration is a stable solution that tends to be aligned to the wind field by the aerodynamic forces, so it could be designed as a free yaw system. In this case a yaw brake can be installed to fix the position of the nacelle when required.

The tower can be made by steel tubes, metal lattice or reinforced concrete and it is based on a reinforced concrete foundation, if an on-shore installation is considered, or on a concrete-metallic floating or non-floating platform, if an off-shore installation is taken into account. The tower layout depends on the characteristics of the installation site. During the design, special attention is focused on the modal properties of the tower to avoid dynamic coupling with the rotor.

The power production and the machine operation are managed by the control system. This component is fundamental to maximize the energy production and to alleviate the operative loads on the structural elements. For this reason, the control logic and the tuning procedure influence the structural design of the overall wind turbine. The

control system includes sensors, computers and actuators. Reliability considerations limit the number and the heterogeneity of the constitutive components. Usually classical controller architectures are adopted, aiming at maximization of the durability to the detriment of the performance.

Various electrical components, such as transformer, power electronic converter and cables connect the generator to the electrical grid. These components stabilize the power output, getting rid of the oscillations related to the turbulent fluctuations of the wind field.

The concept of wind turbine, briefly reported here, is the most common industrial configuration. However, other solutions can be considered, as Darrieus or Savonius type vertical axis wind turbine. None of these alternative concepts has never been able to achieve the cost of energy ensured by the HAWT, but it is possible that in the future they will be successfully employed for other purposes. Focusing on production of the electrical power, the HAWT configuration is considered and studied.

1.2 Aero-structural design of horizontal axis wind turbines

The extreme working condition and the remote installation site make the reliability the most important requirement for a wind turbine. The active components and the complexity of the constitutive systems are usually limited to minimize the fault probability and to maximize the durability of the entire configuration. In such a framework, the aero-structural design of the wind turbine is crucial to achieve the best performance because it refers to the intrinsic nature of the components, without relying on the installation of extra elements.

The aero-structural design problem of wind turbines concerns the definition of the optimal external aerodynamic shape and of the structural components that realize some desirable compromise among several figures of merit, including aerodynamic efficiency, weight, manufacturing costs, transportability, etc. All necessary trade-offs are usually considered and ultimately finalized within the more general problem of designing the whole wind turbine, where the goal is typically the minimization of the Cost of Energy (CoE).

The most important aero-structural elements can be identified by analyzing the invested capital of each component and by considering the effects on the global performance. Usually the rotor blades are acknowledged as the most important aeroelastic elements because of their key role in power production process. Furthermore, they are the main source of the applied loads on the wind turbine, so they influence the entire structural design. The maximization of the performance suggests to apply optimization techniques to asses the blade design problem. This choice implies the the definition of a merit figure that is usually identified by a CoE model, allowing the right trade off between different parameters and pointing out the best compromise [3]. Notice that the global optimum can be identified only by a holistic procedure, able to include the fundamental couplings from the initial phases of the project. However, the difficulties related to a multidisciplinary approach are usually solved by splitting the blade aero-structural design in multiple mono-disciplinary problems, involving the aerodynamics and the structure separately.

Considering the structural design of the blade, the engineering approach relies on

multiple modeling levels. After a first coarse-level preliminary sizing performed using beam-like models, one performs a fine-level verification using 3D FEM and corrects any possible deficiency. This two-stage analysis is typically performed "by hand", revealing to be an high consuming procedure. Possibly, the result of the fine-level verification is used to update the coarse-level dynamic model and the process is iterated until convergence. Clearly, this procedure is time consuming and labor intensive. Furthermore, the design is not conducted as an integrated multi-level optimization, and might lead to sub-optimal results since there is not a consistent way to reflect the results of the fine-level analysis into modifications of the coarse-level models.

The design of wind turbine blades has been the subject of several investigations, and software packages are available that can support the process at the various necessary description levels. In the following some of the relevant literature is reviewed, first for preliminary coarse-level sizing and then for detailed fine-level verification.

As previously stated, a coarse beam model is often sufficient for preliminary analysis as it is capable of providing fast and accurate results for primary parameters such as natural frequencies, deflections, loads and the estimation of the overall dynamic behavior of the machine. At this stage, multibody procedures are routinely adopted, using geometrically exact beam formulations as in [4] and as in the nonlinear finite-element-based multibody dynamics wind turbine simulation code `Cp-Lambda` (Code for Performance, Loads, Aero-Elasticity by Multi-Body Dynamic Analysis) [5, 6] used here, or with Timoschenko beam elements as in [7]; modal representations of the flexible elements are also in widespread use, as in the wind turbine aero-elastic codes `FAST` [8] and `GH-Bladed` [9].

The use of such tools for preliminary design of rotor blades has been described in a few publications. In particular, the codes `RotorOpt` [10, 11] and `FOCUS6` [12] implement integrated design environments. A suite of design tools is described in [13], providing the facilities for preliminary blade design, although the various software modules do not appear to be integrated in a unified optimization framework. Recently, the multidisciplinary wind turbine design code `Cp-Max` (Code for Performance Maximization) was described in [14]. In that work, the structural blade design problem is formulated as a constrained optimization based on a two-level modeling system. The first level is represented by a parametric aero-servo-elastic multibody model, while the second level by 2D finite element parametric models of the blade cross sections. The integration of the two models allows for the synthesis of a beam given its cross sections, and for the evaluation of the sectional loading given the beam one, which are the two crucial steps of the design problem. In fact, from the sectional models, fully-populated stiffness matrices are computed using the code `ANBA` (Anisotropic Beam Analysis), based on the anisotropic beam theory formulated in [15]. The stiffness matrices obtained in this way are used for defining geometrically exact shear and torsion-deformable beams [16] in `Cp-Lambda`. On the other hand, recovery relations provided by `ANBA` allow for the computation of local sectional stresses and strains based on internal stress resultants computed with `Cp-Lambda`.

The formulation described in [14] enables the structural optimization of rotor blades through the integration of 2D cross sectional analysis and 1D spatial beam models. Although that paper mentioned the link towards a detailed fine-level 3D FEM verification of the design, the formulation lacked the ability to close the loop from fine-level analy-

sis back to coarse-level representation, which is the only way one can generate a design that is optimal and constraint satisfying at the finest description level. Another example of multi-level optimization approach is performed in [17], using meta-models to include in the optimization procedure geometric wind turbine parameters, for example rotor diameter and hub height. Considering large wind turbine, a complete presentation of a design procedure can be found in [18].

Different algorithms can be applied to rotor optimization. Sequential quadratic programming techniques are exploited in [14], allowing to include large amount of constraints in efficient way. Particle swarm algorithm is applied to optimize composite blade structure and position of spar caps in [19]. Multiobjective aerostructural optimization techniques are performed in [20], focusing on rotor thrust, annual energy production and blade mass. Also structural topology can be optimized as reported in [21], where an unconventional spar cap configuration is introduced.

Considering the fine-level verification, several tools have been produced for the detailed structural analysis of wind turbine blades, typically developed in the form of pre- and post-processing software interfaced with commercial FE solvers. For example, `NuMAD` [22] serves as a pre-processor for the commercial FE software `ANSYS`. Given an externally generated Computer Aided Design (CAD) model, the code produces a mid-thickness model of the blade, meshes it using shell elements, and lets the user define all necessary material properties, loading and boundary conditions for the required analyses. Similarly, `FOCUS6` is also capable of generating detailed structural models of rotor blades using lay-up shell elements, while `NSE-blade-mesher` [23] exploits a combined solid and shell element mesh in connection with the FE solver `ABAQUS`. This code was used for confirming the bending and twisting behavior of a blade predicted by sectional analysis in [24], while a full structural multi-criteria optimization for a given aerodynamic shape is performed in [25] by utilizing a parametric FE model using `ANSYS`.

The attention of the scientific community for the structural design of the rotor blades is clearly highlighted by the various papers herein reported. The potentialities of the structural design can be smartly enhanced by looking at the contributions of the different components to the Initial Capital Cost (ICC) of a wind turbine. The ICC can be considered as the summation of the expenses to realize and make operative a wind turbine. The contribution of the tower to the ICC is comparable to the rotor cost and it is around 16% of the total price for a land-base installation. Considering an off-shore solution, the wind turbine cost is a lower fraction of the ICC, but the cost of support structures increases considerably [26]. This fact highlights the importance of the tower, and the support structures in general, and it suggests to pay attention also to tower design.

Different approaches concerning the structural design of the single tower are investigated by the available publications. Classical tubular steel tower optimization is performed considering different structural properties as merit figures [27] or measuring the optimality by a cost model [28]. Different degree of detail can be found in the design procedure, ranging from global structure analysis to local details as reported in [29] and [30], where local opening and welding joints are considered. Also different architectures are explored: steel lattice towers optimization are analyzed in [31], while a solution based on fiber-reinforced composites is reported in [32] and a comparison be-

tween the use of steel and concrete is shown in [33]. Despite the variety of the reported methods for the tower structural design, a general approach to design the rotor blades and the tower structure is missing. Since these components are strictly connected by aerodynamic and structural couplings, it is assumed that only a monolithic procedure is able to identify the best configuration, achieving the minimum CoE.

Despite the interdisciplinary nature of the wind turbine, the pure structural design has been considered up to now. Nevertheless, the design of wind turbine rotors is an inherently multidisciplinary activity that requires the complex integration of several different optimization processes. On one hand, the external shape of a wind turbine blade is driven by aerodynamic considerations that ultimately aim at maximizing the power extraction from the wind. This implies the use of very efficient and thin aerodynamic profiles along the span of the blades and the design of a very low solidity rotor. On the other hand, structural efficiency requires a high distribution of area moment of inertia to achieve a satisfactory bending stiffness of the blades. This means both the use of thick airfoils and for a given aerodynamic shape high chords throughout the span of the blades. Looking at the figure of merit of a wind turbine rotor design optimization problem, the minimization of the CoE produced by a wind turbine is identified as being the strategy to be pursued. However, in the CoE formulation the Annual Energy Production (AEP) and the cost of the rotor drive the design in opposite directions. In this context, a coupled aero-structural optimization process is seen as an important development in the research context of wind energy.

Looking at the available scientific literature, large efforts have been recently carried out towards the aero-structural optimization of wind turbines and wind turbine rotors in particular. Current research programs are for instance being conducted at the U.S. National Renewable Energy Laboratory (NREL). In [3], the effect of using different cost functions for the same optimization problem is analyzed, concluding that the CoE as merit figure leads to the most correct results, but also highlighting the need for high-fidelity cost models, which are generally unavailable to the public. Important studies have also been conducted at Politecnico di Milano, highlighting the strong contrasts between aerodynamic and structural efficiency. In [14], high fidelity models have been used for either aerodynamic or structural optimizations and a coupling of the two procedures was tempted. A recent development [34] used lower fidelity models to include the capability of simultaneously designing airfoils, chord and twist distributions and internal structure as done for the optimization of modern wings for high efficiency aircrafts. Several other studies have also been conducted with many other tools with a varying degree of model fidelity. In [17], a multi-level framework is developed to coordinate multiple optimizations, involving different disciplines and modeling techniques. The ultimate goal is to perform a top-level optimization that provides a feasible aero-structural design according to all disciplines. A simultaneous design of aerodynamic properties and Bend-Twist Coupling (BTC) is carried out by [35]. Airfoil shapes, chord and twist distribution and degree of structural coupling are considered as optimization variables, while a CoE model provides the merit figure. The reduction of the CoE, achieved by the authors, is due to a decrease of the blade loads, keeping constant the aerodynamic performance. A site-specific aero-structural design is instead achieved in [36], aiming at a reduction of the CoE for a specific wind turbine location. The effects of the site-specific wind distribution are highlighted comparing the optimal de-

signs for different locations. It is also particularly notable the recent work performed by Ashuri et al. [37], which aims at achieving a good trade-off between model accuracy and computational costs to reach the minimum CoE. In [37], a global reduction of the CoE is reported thanks to an optimal coupling between rotor aerodynamic performance and rotor and tower structures. Notice that, if a CoE model is not adopted as merit figure, multi-objective optimization technique can be applied. An example is reported in [20], where aerodynamic properties and structural properties are optimized by considering as objective functions turbine trust, AEP and blade mass.

Until now the attention has been focused on the optimal design of aero-structural properties of the rotor blades and the structural characteristics of the tower. Obviously the classical concept of the aerodynamics and the structure is fundamental to maximize the performance, as emerged by the review of the scientific literature. However, the classical configuration could merge with innovative solutions, aiming at a further improvement in terms of CoE. In this case, the main requirement of each extra-component is a limited reduction of the reliability of the wind turbine.

An important example is represented by the load alleviation techniques. They aim at the reduction of the loads acting on the wind turbine, allowing a more efficient structural design, that turns out in a reduction of CoE. In the last years, a remarkable interest has been focused on these techniques as shown by the various research papers, for example [38,39]. Notice that it is not possible to provide a broad-spectrum investigation of load alleviation methods because it would require a remarkable amount of time due to the extension of the topic. For this reason, the attention is focused only on a specific application that appears to be innovative in wind energy field, as shown hereinafter.

A decreasing of the load value could be achieved by active or by passive techniques. The active techniques rely on active control systems. These solutions can drive actuators that move the entire blade, i.e. the pitch actuator, or they can employs distributed devices, such as active flaps or plasma actuators placed along blade span, or they can deals with a combination of these systems [40]. In this case a reduction of reliability of the wind turbine is expected for various reasons. The first one is the increase of the actuator duty cycle due to the load alleviation activity required by the control law. The second reason is the existence of extra components, as sensors and actuators, that increase the maintenance activity. This issue is magnified by considering the distributed systems that are installed along the blades. Both aspects are usually unbearable in wind energy, implying a poor success of the active techniques for load mitigation in real industrial applications.

On the other hand, passive load alleviation techniques affect the system reliability partially, so they seem to be more suitable to wind energy applications. The traditional techniques, such as BTC and geometric coupling, have proved their effectiveness [41]. These techniques usually encompass a large span-wise extension of the blade, so they operate like an individual pitch actuator installed at the blade root. Therefore, these solutions are unable to react to local noise due to turbulent fluctuations of the wind field. The gap between these passive solutions and a distributed active configuration can be filled by a passive distributed device. An example of this system could be a passive control surface with limited span-wise extension, installed on each blade. The passive control surface is forced by the loads due to the motion of the blade, so no active components are required. This concept, here defined as passive flap, merges

the advantages of the distributed control with the reliability of a passive device. The calibration of the aerodynamic and structural properties of the passive element is crucial because it determines the interaction with the overall wind turbine. The main goal of the tuning is the load alleviation, minimizing the interference with active control system and other standard wind turbine components.

The passive load alleviation by appended devices has been employed in aeronautic applications, especially before the developing of the active control systems. A first example of a gust-alleviating passive flap can be found in aeronautical field [42]. The experimental setup shows the effects of a long-period dynamically overbalanced flap on an aircraft wind tunnel model. A reduction of the acceleration due to an atmospheric gust is displayed but also a decrease of airplane stability is reported.

Considering rotorcraft applications, an analytic investigation of aeroelastic devices appended to rotor blades is cited in [43]. Among different devices, a passive trailing edge tab concept is shown. The importance of the tuning is highlighted, since the tab motion must be correctly phased to delete the blade harmonic airloading that induces vibrations to the mast. A preliminary simplified analysis is provided, showing promising results. However the device appears to be counter-productive if examined in a more complex framework. The authors do not identify the causes of this mismatch and they suppose that the tab is not tuned properly.

Another passive rotorcraft appended device, similar to the passive flap, is the free tip rotor [44]. The free tip rotor is a conventional rotor except that the blades are modified in the outer part to embed a free pitching tip. This device improves the aerodynamic efficiency, smoothing the airload distribution in the blade tip region when the blade azimuth position is varied. Also in this case the tuning is crucial, as the position of aerodynamic and mass center of the tip relative to the blade pitch axis. Passive control strategies are applied to modulate the torsional moment applied to the free-tip. Different solutions are shown in [45], reporting the sketches of the design concepts.

These studies have shown that the advantage, ensured by a passive device, is overcome by the increase of weight. Therefore, the installation is not convenient in aeronautical and rotorcraft applications, where active systems are preferred despite the loss of reliability. Different requirements characterize wind energy solutions, where the maximum reliability request is stressed, making the passive flap idea still attractive. A first application in wind energy of passive distributed system for load alleviation is analyzed in [46]. A passive camber control concept is investigated, considering 2D aeroelastic typical section. The variation of airfoil camber is imposed by local aerodynamic load, while the original shape is restored by concentrate spring and damper. Three simplified load cases are evaluated, showing a significant decrease of load fluctuations.

Passive load alleviation can also be achieved by structural morphing concept as reported in [47]. A bi-stable specimen is designed, tailoring orthotropic material. When the applied load exceed a threshold value, the structure switches from the reference state to the other statically stable state that generates less lift. This process does not require moving parts, but the main drawback is that an active component should be installed on the blade to restore the original shape [48]. For this reason the solution cannot be considered as a purely passive solution.

1.3 Contributions of the Present Work and Outline

Two macro-areas of research are considered: the first one is the aero-structural optimization of wind turbines while the second one is the application of the passive load alleviation techniques in wind energy field. These research topics are considered as two common parts of the aeroelastic design of wind turbine. Therefore the differences should be only apparent because only a monolithic approach can ensure the maximization of the performance, merging load alleviation techniques with an holistic wind turbine design. This project moves in this direction, developing and validating the required methods for a holistic aero-structural wind turbine design that will consider passive load alleviation techniques.

1.3.1 Research approach

As shown by the cited literature, the design of the aerodynamic and structural properties of the wind turbine has been widely considered by the scientific community. However, in most cases, the optimal design problem has been solved taking into account simplified case studies that are distant from the operative conditions defined by the international standards. This limitation is overcome by the current project, where a general approach is always pursued, using a reliable simulation environment to evaluate the wind turbine working conditions.

The analyses are based on in-house developed software, such as `Cp-Lambda` and `ANBA`, commercial package, like `MSC.Nastran`, and open-source codes, as `TurbSim`. A detailed description of the modeling approach will be reported below, but it is here remarked that the developed techniques are tailored to this general approach. The hypotheses and the approximations are compliant with a real operative framework. Turbulent and deterministic working conditions can be considered, furthermore specific situations can be reproduced by the flexibility ensured by the analysis tool.

The complications, involved by the generality, force to develop the design methods by an incremental approach. At the beginning the problem of optimal design is solved by considering the monodisciplinary optimization of the standard components of wind turbine. This approach allows to identify the potentialities of each procedure, before increasing the tool complexity. After that, a multidisciplinary design tool is developed, providing different techniques to face the aero-structural design of a wind turbine. The validated design procedures are finally extended by an innovative concept for load alleviation. This research approach is followed by the structure of this thesis, as it is clearly stated by the next section.

1.3.2 Treated Topics and Presentation Outline

The first research activities are concerned with the structural design of wind turbine rotor blades for given aerodynamic shape. Although this is only one aspect of the general problem of designing a wind turbine, as mentioned above, it is nevertheless a highly complex and challenging task. In fact, the design should identify optimal structural layout, choice of materials and proper sizing of all structural members to ensure a cost-effective, safe and efficient operation throughout the lifetime of the machine. Given layout and materials, the sizing problem should be performed in such a way that all blade components (from webs, skin and spar caps, to root bolting and all the way down

to glued connections, reinforcements, etc.) can withstand extreme loads and the effects of fatigue due to deterministic cyclic and stochastic turbulent excitations. Furthermore, the blade should be designed in such a way to avoid resonant conditions, which would increase vibrations and fatigue, be stiff enough to avoid striking the tower even under extreme operating conditions, be flutter-free in all of its operating envelope including emergency conditions, and also free from local instabilities such as skin buckling, wrinkling, etc. The design should also be able to fully exploit the anisotropic properties of composite materials, for example for inducing load mitigating couplings between blade bending and twisting [49]. Clearly, these goals should be met with the minimum possible cost, while satisfying all necessary manufacturing constraints.

The main challenge of this design problem comes from the need to marry the unsteady nature of loading in a wind turbine, which requires transient analyses, with the need to capture local effects such as stress concentrations and instabilities in complex 3D structures made with anisotropic composite materials. Transient analyses are routinely performed with beam-like models of the machine dynamics, coupled to suitable aerodynamic models and control laws that enable the simulation of the whole spectrum of unsteady operating conditions defining extreme loads and deflections, as well as fatigue. On the other hand, the verification of the local state of stress and strain and its stability are typically conducted with detailed 3D static finite element models, under loading conditions obtained from the ones computed with the transient models.

The scope of the first project phase is to improve on the current design method of rotor blades, by proposing a multi-level design procedure that conducts the design in a fully integrated and automated manner. The method includes 2D finite element models for the characterization and analysis of the blade cross sections, aero-servo-elastic multibody models for load calculation according to certification guidelines [50, 51], and detailed 3D finite element models for detailed stress-strain, fatigue and buckling analysis. The design optimization is conducted by iterating among the various levels, so as to deliver a cost-minimizing design solution that also satisfies all desired design constraints at the finest description level, i.e. the detailed 3D model.

A new tool is described for the automatic generation and analysis of 3D FE structural blade models. First, a detailed CAD model is generated in terms of Non-Uniform Rational B-Spline (NURBS) surfaces directly from the blade geometry obtained at the coarse description level. Next, the CAD model is associated with material properties, boundary as well as extreme and fatigue loading conditions, and meshed into shell or solid elements to enable the execution of the necessary analyses.

Static deflection and fatigue analyses are conducted on the fine-level 3D model, with the goal of verifying the satisfaction of the stress, strain and fatigue constraints, since the 3D model can represent effects that sectional and beam models cannot capture. Furthermore, a buckling analysis is performed under the most severe loads conditions.

A heuristic approach is used for incorporating the effects of the 3D FEM level analyses back into the coarse-level model. This way, new 2D sectional models are generated which in turn define a new 1D spatial beam model, and the complete process is repeated. Typically, very few iterations between the coarse and fine levels are necessary for convergence.

Through the new procedure described herein, a multi-level optimization is used to determine cost-minimizing design solutions that satisfy all desired constraints at the

finest description level within reasonable computational costs. In particular, the loop closure between fine 3D FEM static and coarse multibody dynamic and cross sectional models is a valuable contribution of the present work.

Having examined the multi-level structural optimization of the rotor blades, the attention is focused on other structural components of the wind turbine, especially on the tower. In scientific publications, a clear separation appears between the rotor and the tower design. This gap is filled by the current project, unifying in a common procedure the optimal sizing of these components. This approach turns out to be of primary importance for multi-MegaWatt (MW) machines, when the requirement of the blade-tower clearance becomes essential. The clearance parameter is the minimum distance between the blade tip and the tower structure that can be encountered in the wind turbine operating range. It depends on the aero-servo-elastic behavior of the wind turbine, establishing a strict connection between blade and tower structures. The best compromise, that ensure the minimum CoE, can be achieved only by an unified optimization procedure where blade and tower are sized in a high fidelity modeling environment. This part of the project exploits the state of the art simulation techniques to define a general design environment where blade and tower structures can be sized by a unique optimization. Furthermore, the developed procedure can be useful applied to perform trend studies, identifying the optimal value of parameters that are not included into the optimization procedure. In this case trend studies allow to optimize the layout of the wind turbine, considering the parameters that affect directly the clearance, such as the rotor cone angle and the nacelle uptilt angle.

Once the structural optimization capabilities of the design tool are increased, different optimization algorithms are proposed to achieve an optimal aero-structural design of a wind turbine rotor. The final configuration is identified by the minimum CoE value, evaluated by a model that merges all the characteristics of the wind turbine in a single value, representative of the entire machine. Compared to all the works just referenced by the literature analysis, in this project higher fidelity models are used, following an industrial approach. This approach is coherent with the pure structural optimization of the rotor blades and of the tower. This means that the final design needs to survive to the long list of Dynamic Load Cases (DLC) specified by international standards, like the ones released by the International Electrotechnical Commission (IEC) [50] and by Germanischer Lloyd (GL) [51]. Moreover, a long set of constraints is accurately taken into account in the optimization process. On one side, aerodynamic constraints, as maximum blade tip speed, maximum chord or chord and twist maximum tapering values, must be respected. On the other side, the rotor structure needs to satisfy stress, strain and fatigue constraints, but also the placement of blade natural frequencies, minimum tower clearance and others. All these constraints have a crucial effect in the optimization and only their inclusion from the initial steps of the process ensures to achieve a correct identification of the minimum CoE. In this work two aero-structural optimization approaches are developed and compared to an existing method.

Considering the structure of the thesis, the optimal design methods are reported in Chap. 2, while the results, provided by the Chap. 3, shows the applications and the potentialities of the developed approaches. Notice that the division of the different topic is related to the exposition, while the design procedures are developed in an integrated tool that reflects the multidisciplinarity of the problem.

The literature analysis has also shown that the passive distributed control has been employed by aeronautical applications but it has not extensively been studied in wind energy. Considering the wind turbine, the design drivers are different than the aeronautical ones. Furthermore different design approaches can be exploited, making passive distributed load alleviation interesting with a view to the CoE reduction. This project aims at exploring the potentialities of a passive flap, in the frame of blade aero-structural design. Obviously the maximization of the performance is ensured only by a global approach that unify the standard blade configuration with this appended device. This approach will be pursued in the future if the passive flap will prove to be a interesting solution.

Since the appended device is passive, the aero-elastic characteristics are fundamental to obtain an effective operation. The tuning process of the passive flap provides further flexibility to the analyst in term of design parameters and it can be considered as an extension of the aero-structural design of wind turbine. In this thesis simplified models and analysis are developed, aiming at a full comprehension of the passive flap system.

A hybrid model is considered at first, merging the classical typical section theory with the input data provided by a comprehensive wind turbine simulation environment. This model allows to tune the passive flap, to assess the system stability and the load reduction capabilities. The interaction with standard wind turbine behavior is investigated by another reduce order model that considers the entire rotor, allowing the estimation of the interference between the controller and the passive device. These models are successfully applied to explore the potentialities of this concept, as reported in Chap. 4. Notice that the current analysis aims at highlighting the pros and cons of such devices in a simplified framework. For this reason the provided results are preliminary and they will be validated by a general simulation environment.

1.4 Technical Notes

The current project is based on data of realistic wind turbines provided by collaborations with industries and research centers. When these data are covered by industrial secrecy, they are provided in non-dimensional form. For the same reason, only a brief description of the wind turbines models are reported, citing the source when the data are public available.

The cited code `MSC.Nastran` is a trademark of MSC.Software Corporation, `Hypermesh` is a licensed product of Altair Engineering, Inc.. `Matlab` is a licensed software of The MathWorks Inc.. The software `TurbSim` is a open source code distributed by National Renewable Energy Laboratory (NREL). `Cp-Lambda` is a licensed product of the Dipartimento di Scienze e Tecnologie Aerospaziali of Politecnico di Milano.

CHAPTER 2

Optimization Procedures

In the current chapter the development of the optimization procedures oriented to wind turbine design is reported. Last years activities have led to the development and improvement of the tool `Cp-Max` (Code for performance Maximization). `Cp-Max` allows the multidisciplinary design optimization of wind turbines using high-fidelity models and different figures of merit. The multidisciplinary approach is due to the intrinsic nature of the problem that involves aerodynamics, structure and control laws in a unique coupled system, while the different merit figures are related to the considered design, as will emerge clearly during the chapter. The research project aims at a holistic procedure, able to design the overall machine in a monolithic approach. This is obviously the final goal pursued by wind turbine design and it is the only way to achieve the minimum CoE configuration. In this thesis the attention is focused on the wind turbine components that most affect the CoE of a classical HAWT layout: the rotor blades and the tower. The contribution of these elements to the initial investment is fundamental. Furthermore, other components, for example the hub, the drive train and the foundations, are designed by considering the boundary conditions imposed by the blades and the tower. This consideration shows that a good design of the rotor blades and the tower influences positively the overall structural design of the wind turbine. Moreover the aerodynamic performance is mainly related to the blade characteristics, affecting the energy harvested during the operative life. This parameter is really important because it influences considerably the CoE through the AEP value. This means that the aerodynamic and the structural design of the rotor blades and tower are crucial to maximize the performance of overall wind turbine, justifying the adopted approach.

The implemented methods exploit a parametric aeroservoelastic model that allows a realistic simulation of the operative conditions. Since the same simulation environment is adopted by the different optimization techniques, a description of the modeling ap-

proach is provided at first in Sect. 2.1. State of the art modeling techniques are reported, focusing on the details that characterize the wind turbine simulation.

Among the different procedures, the mono-disciplinary design is considered at first. The current project starts from the original aerodynamic and structural optimization capabilities of `Cp-max`, that refer to the single blade only. The original version of `Cp-max` is entirely reviewed, leading to the current edition reported in this chapter, where the `Cp-max` features are shown to provide a global overview of the design tool.

The attention is focused on the aerodynamic design in Sect. 2.2. The aerodynamic properties of the blade are optimized to maximize the AEP, while the structural parameters are constant. At the beginning a global description of the approach is reported, then the algorithmic form of the method shows the details of the implementation. After that, some details about the model parametrization are explained, describing the selection of the optimization variables. Finally the cost function calculation is considered, giving some details regarding the evaluation of the aerodynamic performance and the regulation policy of the wind turbine.

Section 2.3 is about the structural optimization of the rotor blades and tower. The method minimizes the CoE of the wind turbine, keeping constant the aerodynamic parameters. In this case the AEP can be considered constant too, so the optimization directly affects the Initial Capital Cost, a single parameter that measures the optimality of the blade and tower structural design. The section is organized as the description of the aerodynamic optimization. A general overview of the method and the algorithmic form show how the design is performed. Then, the structural parametrization of the model describes the layouts that can be optimized. After that, a description of the CoE model is considered. Although in this case the AEP is constant, a general overview of the CoE model is provided because all the features of the same model will be exploited to define the merit figure of the aero-structural optimization procedures. After the merit figure characterization, a brief description of the automatic tuning of the wind turbine controller is reported. The process is based on the aerodynamic performance and the regulation policy defined in the Sect. 2.2. Notice that the controller is essential to evaluate the DLC, boundary conditions of the structural design, so a robust procedure to update the control laws in conjunction with the aeroelastic model should be provided. Finally, since the structural design procedure is developed on different modeling levels, the interaction between these levels is reported. Notice that the current section is focused on the coarse-level, while the refinement levels will be reported separately in Sect. 2.5–2.6.

After the description of the mono-disciplinary optimization of the aerodynamic and structural properties, the aero-structural design is considered. The procedures, reported in Sect. 2.4, merge the aerodynamic and the structural optimization variables, minimizing the CoE value. At the beginning a practical example shows the limits of mono-disciplinary optimizations, highlighting the restrictions of a sequential design that separates the aerodynamics and structure. After that, the attention is fixed on the developed aero-structural procedures. Since different approximations and hypotheses can be set, various algorithms are developed. The robust Pre-Assumed Aerodynamic Shape (PAAS) approach is presented at first. The External Aerodynamic/Internal Structure (EAIS) approach is then reported. Finally the Monolithic with Load Updating (MLU) approach is shown. Each formulation of the algorithms entails different

computational cost and requires various skills of the blade designer. These differences are emphasized by the description of each method and they are clarified by the analyzed test case in Sect.3.4.

At the end of structural or aero-structural optimization, a refinement analysis can be applied to the optimal configuration obtained by the coarse-level design. The refinement analysis allows to introduce small corrections to the optimization loop, including the effects that are not modeled at the coarse-level. Essentially, the refinement analysis implies the generation of a three-Dimensional (3D) Finite Element Model (FEM) that encompasses the entire blade or zooms on critical regions. The creation of the 3D FEM of the overall blade is reported in Sect. 2.5, while the detailed analysis is considered in Sect. 2.6. The fine-level model is generated by a similar procedure in both cases, so the structure of these sections can be summarized as follow. After some general consideration about the modeling aspects, the CAD geometry is generated by the model parametrization provided by the coarse-level. Then the FEM is created, considering the CAD geometry. Finally all the requested analyses can be computed, providing the required measurements to the closure of the multi-level optimization loop.

2.1 Wind Turbine Aeroelastic Modeling

Optimization techniques of complex aero-servo-elastic system, such as wind turbines, are strictly related to the capability of parametrizing a high fidelity model in an omni-comprehensive simulation environment. A general description of modeling techniques is here reported to better understand the following sections. The interested readers can find further details in [14], [52] and [53]. On the other hand, the choice of the optimization variables and the model parametrization will be considered consistently with the corresponding optimization technique.

The core of the wind turbine simulator is `Cp-Lambda` (Code for Performance, Loads, Aero-Elasticity by Multi-Body Dynamic Analysis [6]). Originally developed for rotorcraft applications, the software has been validated through numerous comparisons with other industrial simulation software, wind tunnel experimental results and field measurements.

`Cp-Lambda` is a MultiBody (MB) aero-servo-elastic simulator software able to describe general topology systems. For this purpose a broad library of elements is provided to the user, including rigid bodies, nonlinear flexible elements, joints, actuators models and aerodynamic models. The constitutive components are described by Cartesian coordinates, large displacements and three dimensional rotation are correctly modeled by referring all the degrees of freedom to a unique inertial frame.

General models of joints are available, furthermore stiffness and damping properties can be provided to each joint as nonlinear lumped parameters. The constraint equations due to the joints are enforced by scaled Lagrange multipliers [54].

Rotor blades and tower are usually described by nonlinear geometrical exact shear and torsion deformable beam models [16]. Different features are allowed, including a general description of cross sectional properties, generic 3D shape and finite motion simulation. Arbitrary beam geometry can be considered as well by curved and twisted beam axis. Flexible components are discretized in space by finite element method, leading to a system of differential algebraic equations in time. Time integration is

performed by an unconditionally stable scheme that enables to include high frequency dissipation [55].

An example of topological description of multibody model is reported in Fig. 2.1. Rotor blades, tower, flexible shaft and nacelle are modeled by beams. The inertial properties of the rotor hub, generator and nacelle are included by rigid bodies. Pitch, torque and yaw actuators are also provided to ensure the wind turbine regulation. The foundations are modeled by lumped springs and damper associated to revolute joints. Obviously a system with a generic topology can be modeled, exploiting the high generality of the MB techniques.

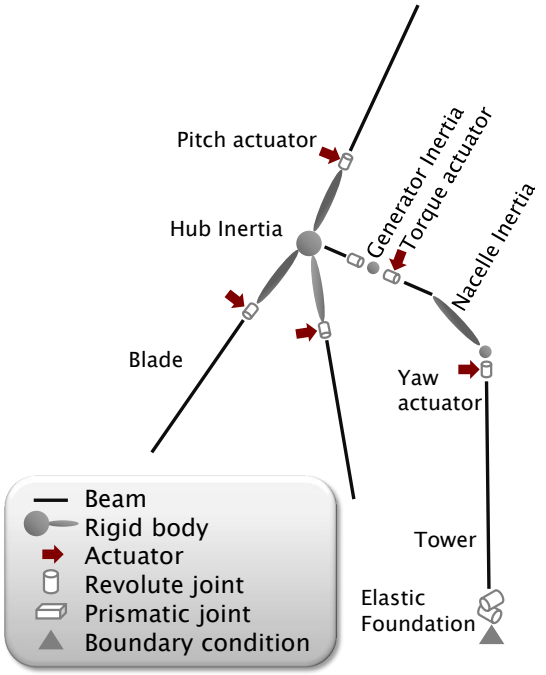

Figure 2.1: *Topological representation of multibody model of the wind turbine*

The aerodynamic properties are defined by lifting lines based on sectional blade aerodynamic coefficients given in tabular form. Root and blade tip loss models, dynamic corrections and dynamic stall model can be taken into account. Aerodynamic loads are modeled by Blade-Element Momentum (BEM) model, based on anular stream tube theory with wake swirl [56]. Dynamic inflow models are also available when model fidelity must be increased [57] [58]. Rotor aerodynamic model is reported in Fig. 2.2, showing the most important properties of the aerodynamic modeling. Notice that the blade lifting lines are not coincident with the beams axes, increasing the model generality. The aerodynamic properties vary along the blade span and they can be tabulated taking into account different Reynolds numbers.

The wind field is computed by external tools: deterministic gusts are obtained by in-house routines, while turbulent time histories are supplied by the open source software `TurbSim` [59]. The frozen turbulence hypothesis is applied, allowing the evaluation of the wind field on a three-dimensional grid before the simulation starts. During the simulation, the motion of the grid towards the wind turbine is imposed. The wind field

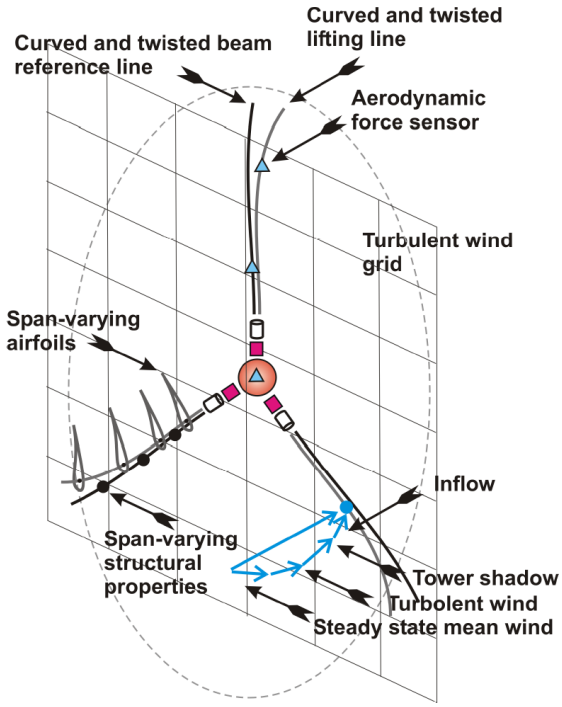

Figure 2.2: *Representation of rotor aerodynamic model of the wind turbine*

is spatially interpolated at each time step on each airstation, i.e. point of the lifting line where the aerodynamic loads are evaluated. Deterministic effects, such as wind shear and tower shadow, can be included too as specified by [50] and [51]. All the aerodynamic effects, that define the relative wind speed on each air station, are shown in Fig. 2.2. The resulting velocity takes into account these contributions but also the blade motion to perform a fully coupled aeroelastic analysis. When the aerodynamic loads are evaluated on the lifting lines, they are moved to the corresponding beam axis by a rigid interface.

In order to ensure regulation over the entire operative range, pitch-torque control strategies are provided by external dynamic libraries. This configuration is flexible and modular, once the interface between the model and the control system has been standardized. Supervisory unit can be included to manage the machine behavior at some specific events, such as start up and shut down in standard and emergency conditions.

All operative situations prescribed by international standard can be simulated, [50] [51]. Various analysis types are considered: static, dynamic and eigenvalues analysis are computed depending on the quantities required by each optimization techniques. Automatic procedures post-process all the results, defining the generalized load envelope. This envelope takes into account the sectional envelopes, that consider the maximum and minimum values of the internal forces on each blade section. The time histories obtained by DLC 1.2, [50] [51], useful to estimate the fatigue damage, as well as the minimum blade-tower clearance loads are also included into the generalized load envelope. This data structure is essential to structural and aero-structural optimization and it deserves special attention during the development of the design techniques as will be shown hereinafter.

All the optimization approaches developed by the current project involves the aeroe-

lastic modeling techniques herein reported. In the next sections `Cp-Lambda` features will be exploited and further details about the modeling approach will be given, depending on the considered optimization procedure.

2.2 Aerodynamic Optimization of Rotor Blades

The aerodynamic optimization of the rotor blades is taken into account in the current section. The considered approach is well established among the scientific community, however a brief description is here reported to better understand the development of the other procedures that involve the aerodynamic design of the wind turbine.

A global overview of the algorithm is reported at first in Sect. 2.2.1. After that, the algorithmic form of the procedure is reported in Sect. 2.2.2, even if the method is quite simple. This description is reported for completeness, introducing the nomenclature and the conventions applied to describe the other optimization method. The aerodynamic parametrization is described in Sect. 2.2.3 and finally the cost function evaluation is reported in Sect. 2.2.4.

2.2.1 General overview of the optimization method

The pure aerodynamic optimization of the wind turbine rotor consists of identifying, for a given set of airfoils, the optimal chord and twist distributions to achieve the maximum AEP. Obviously this approach could be extended by considering the airfoil shape as optimization variable. The resulting approach is usually called free-form optimization and it allows to design family of airfoils oriented to specific wind turbine. Even if this approach would be more general, it is chosen to postpone it to a further project phase to limit the problem complexity, especially in the aero-structural approach.

The optimization procedure relies on a parametrization of the aerodynamic properties of the blade by perturbation functions. This choice allows to limits the number of optimization variables and the resulting computational time.

The AEP is considered as merit figure to investigate the entire power production range. The AEP evaluation is based on a `Cp-Lambda` multibody model of the wind turbine. During this process, it is important to consider the overall wind turbine to take into account the all the possible couplings during the performance evaluation.

The design requirements are expressed by a set of nonlinear constraints that is included in the optimization problem. Gradient based optimization techniques are applied, ensuring the best performance through an efficient inclusion of the constraints [60].

Although gradient base techniques are applied, the local minima are not a concern for several reasons. First of all, the initial guess provided to the optimizer is a credible configuration, not too far from the optimal one. This initial layout can be obtained by analogy or by a scaling procedure from an existing HAWT. Various case studies are available in literature, so this kind of information is easy to find. Furthermore, no severe transformation of the conventional configuration is expected, when a classical HAWT is considered, so the optimal solution is supposed to be next to a good initial guess. Finally the solution space is considered smooth, especially near to the optimum, ensuring good convergence properties. This is a reasonable assumption due to the technological constraints, that impose a regular blade shape, and due to the operative conditions

of the blade airfoils, that are usually characterized by a high aerodynamic efficiency and by attached flow conditions. Notice that the smoothness of the merit function is mandatory when gradient base optimization methods are applied, so these considerations legitimate also the approach here reported.

2.2.2 Optimization algorithm

The optimization methodology has been developed in detail in [14], however a summary will be here reported. The algorithm can be expressed as follows:

$$\textbf{Function } (\boldsymbol{p}_a^*, P_y^*) = \texttt{MaxAEP}(\boldsymbol{p}_a, \boldsymbol{p}_s, D) : \tag{2.1a}$$

$$P_y^* = \max_{\boldsymbol{p}_a} \texttt{AEP}(\boldsymbol{p}_a, \boldsymbol{p}_s, D) \quad (\text{and } \boldsymbol{p}_a^* = \arg\max_{\boldsymbol{p}_a} AEP), \tag{2.1b}$$

$$\text{s.t.:} \quad \boldsymbol{g}_a(\boldsymbol{p}_a) \leq \boldsymbol{0}, \tag{2.1c}$$

$$v_{\text{tip}} \leq v_{\text{tip}_{\max}} \tag{2.1d}$$

Here and in the following, functions are indicated with the notation

$$(O) = \texttt{FunctionName}(I), \tag{2.2}$$

where I are the input variables, while O the output ones.

In equation 2.1, $\boldsymbol{p}_a$ and $\boldsymbol{p}_s$ are the aerodynamic and structural variables of the optimization problem. $\boldsymbol{p}_a$ is the union of $\boldsymbol{p}_{a,t}$ and $\boldsymbol{p}_{a,c}$, which are the vectors of the shape functions that modify twist and chord distributions respectively.

D is a field containing a list of given data:

$$D = \{P_r, V_{in}, V_{out}, R, H, AF, C, v_{tip_{max}}, ...\}. \tag{2.3}$$

The list includes, among others, the rated power P_r, the cut-in and cut-out wind velocities V_{in} and V_{out}, the rotor radius R, the tower height H, the airfoil types used along the span AF, the wind turbine class C, the maximum tip speed $v_{tip_{max}}$. The maximum AEP, denoted P_y^*, is obtained at the corresponding $\boldsymbol{p}_a^*$. Finally, $\boldsymbol{g}_a$ represents a set of linear and nonlinear constraints applied to $\boldsymbol{p}_a$. The set is flexible and can be tailored to specific needs, but it generally includes values for maximum chord, upper bound for the first and/or second derivatives of chord and twist distributions, a tapering parameter and minimum or maximum rotor solidity. This set is useful to express the technological constraints, related to chord and twist variability, but also transportability requirements can be included, for example due to the maximum chord value if an onshore wind turbine is considered. Furthermore the equations (2.1c) can be exploited to parametrize the optimal aerodynamic result by some macro-parameters useful to explore the solution domain as it will be shown by Sect. 2.4.2.

The optimization routine `MaxAEP` is implemented in `Matlab` [61]. The core of the code is the gradient-based optimization function `fmincon`, which uses a Sequential Quadratic Programming (SQP) algorithm.

`MaxAEP` has proved good robustness and convergence is generally achieved in few iterations. The computational cost of the aerodynamic optimization routine is limited compared to the other optimization processes later described.

2.2.3 Model Parametrization

The aerodynamic properties of the MB model are parametrized by considering the chord and the twist span-wise distributions. These measurements are related to the blade lifting line that provide the definition of the aerodynamic properties of the MB model. The geometry of each lifting line is defined by a Non-Uniform Rational B-Spline (NURBS) curve, so maximum flexibility is ensured, allowing the creation of arbitrary three-dimensional curved and twisted lines. Span-wise varying data are associated to each lifting line, allowing the exact reproduction of the local chord length, chord-wise position of the aerodynamic center and the other characteristics of the airfoil.

Since only chord and twist span-wise distributions are modified by the parametrization, the other data required to express the aerodynamic characteristics of the blade are kept constant. As reported above, the airfoils type is fixed for sake of simplicity, but also the airfoils span-wise position is kept constant. Since the airfoil types turns out to be important in the blade design, it is possible to include the choice of the airfoils, performing trend studies with different airfoil groups. The airfoil family, or the combination of airfoil type that ensures the best performance, can be selected. In contrast with the airfoils shape, the airfoils span-wise position is a minor parameter, as shown by in-house trend studies, and it can be neglected without affecting the optimality of the result.

The current parametrization aims at a good description of the blade properties limiting the number of the degrees of freedom. Multiplicative and additive shape functions are considered to deform the original baseline distributions. The twist $\theta(\eta)$ and chord $c(\eta)$ distributions are expressed as:

$$\theta(\eta) = s_\theta(\eta) + \theta_{bl}(\eta) \tag{2.4}$$

$$c(\eta) = s_c(\eta) c_{bl}(\eta) \tag{2.5}$$

where η is a nondimensional span-wise coordinate, that assume zero value at blade root and unitary value at blade tip. $\theta_{bl}(\eta)$ and $c_{bl}(\eta)$ are the baseline distributions, provided as initial guess. The deforming functions $s_\theta(\eta)$ and $s_c(\eta)$ are expressed as:

$$s_\theta(\eta) = \boldsymbol{n}_\theta(\eta)\boldsymbol{p}_{a,t} \tag{2.6}$$

$$s_c(\eta) = \boldsymbol{n}_c(\eta)\boldsymbol{p}_{a,c} \tag{2.7}$$

where $\boldsymbol{n}_\theta(\eta)$ and $\boldsymbol{n}_c(\eta)$ are the shape functions and $\boldsymbol{p}_{a,t}$ and $\boldsymbol{p}_{a,c}$ are the optimization parameters $\boldsymbol{p}_a = [\boldsymbol{p}_{a,t}, \boldsymbol{p}_{a,c}]$. A necessary smoothness is achieve by the use of cubic splines for the shape functions $\boldsymbol{n}_\theta(\eta)$ and $\boldsymbol{n}_c(\eta)$.

Since the parametrization relies on deformation functions, a multiplicative approach can be used only for chord because it is ensured that this distribution always assumes nonzero values. On the other hand, this condition is not valid for the twist, so an additive deformation function gives the variability all along the blade span.

Obviously the unknown distributions can be directly described by assumed function, as Bézier curve, with minor modifications. However, in general, a larger number of degrees of freedom is required by this approach than the number requested by the deformation shapes technique.

2.2.4 Cost Function

The cost function `AEP` evaluates the AEP of the wind turbine by the following steps. Firstly, the lifting lines describing the aerodynamic properties of blades of `Cp-Lambda` model are updated, based on the given $\boldsymbol{p}_a$ from the baseline configuration. Then the aerodynamic performance, in terms of power coefficient C_P, are evaluated, varying the tip speed ratio λ and pitch angle β. Considering the aerodynamic performance, it is possible to evaluate the regulation policy. This strategy defines the reference conditions of the wind turbine along the operative range, according to [62, 63]. The whole process to compute the regulation trajectory just described is doubled and it is first performed on a coarse λ-β grid mesh and then on a more refined grid. This allows a more accurate computation of the states of the machine at limited computational costs. From the regulation trajectory, it is then possible to compute the power curve of the current configuration, weight it with the Weibull distribution for the prescribed wind turbine class [50, 51] and finally compute the AEP as:

$$\text{AEP} = T \int_{V_{in}}^{V_{out}} P(V) p_{Weibull}(V) dV \tag{2.8}$$

where T is the number of hours in one year, V_{in} and V_{out} are cut-in and cut-out wind speed, P is the power and $p_{Weibull}$ is the probability density function of the wind.

To better understand the evaluation of the AEP, further information is provided in the next paragraphs, focusing on the evaluation of the aerodynamic coefficients and the regulation policy.

Evaluation of Aerodynamic Performance

The wind turbine aerodynamic coefficients define the global aerodynamic performance of the rotor. Various techniques are available to estimate the power coefficient in term of tip speed ratio λ and pitch angle β. The simplest approach deals with an ideal rigid rotor in axial flow condition, neglecting the aeroelastic effects and the interactions with the other wind turbine elements. However this approach introduces a lot of approximations that cause an overestimation of the performance.

Basically, a lot of effects can downgrade the characteristics of the ideal rigid model. A first element is the wind field that is not axially oriented and it is not homogeneous due to the presence of the wind shear. Furthermore the elastic deformation of the wind turbine components can modify the configuration, altering the working conditions. For example the bending of the tower can alter the nacelle uptilt angle, modifying the alignment of the rotor axis toward the wind direction. Other effects are related to the deformation of the blades that influences the force distribution on the overall rotor. For these reasons, a more advance model should be used than the ideal rigid one.

In the current project the evaluation of the $C_P(\lambda, \beta)$ surface is performed by an aeroelastic `Cp-Lambda` model of the entire wind turbine. Static simulations are run to evaluate the aerodynamic performance of the machine for a two-dimensional grid of different states, described by different values of tip speed ratio λ and pitch angle β. These simulations take into account the aero-elastic effects of the flexible bodies of the MB model and include the computation of aerodynamic, inertial, gravity and also centrifugal loads. These simulations represent snap shots of the wind turbine configuration at a

certain operative condition. The aerodynamic performance is then evaluated by extracting the internal forces acting on the hub shaft, and particularly the torsional moment. If this value is nondimensionalized, it is possible to draw the power coefficient C_P of the wind turbine toward λ and β and from these curves, the regulation trajectory can be computed as reported by the next section.

Evaluation of the regulation policy

The regulation trajectory is accurate and includes the definition of regions II, II$\frac{1}{2}$ and III to respect a potential constraint on maximum tip speed [62]. It may here be useful to point out that region II$\frac{1}{2}$ is function of the rated rotational speed, which is in turn dependent on the solidity of the rotor. Therefore, during the different iterations of the aerodynamic optimization loop, region II$\frac{1}{2}$ may become a requirement or not based on the variations of $\boldsymbol{p}_a$.

The region II ranges from the cut-in wind speed to the appearance of the region II$\frac{1}{2}$, due to the v_{tip} constraint, or to the achievement of the rated power, where the region III starts. In region II, the wind turbine operates at maximum value of C_P, obtained by the solution of the following optimization problem:

$$C_P^{II} = \max_{\lambda,\beta} C_P(\lambda,\beta) \tag{2.9}$$

$$\lambda^{II},\beta^{II} = \arg\max_{\lambda,\beta} C_P(\lambda,\beta) \tag{2.10}$$

where C_P^{II} is the maximum value of the power coefficient and λ^{II} and β^{II} are the associated tip speed ratio and pitch angle values, constant with respect to the wind speed.

If the constraint equation (2.1d) is active, the region II$\frac{1}{2}$ divides the region II and the region III. This is a transition zone where the rotor speed is imposed to the maximum allowable value $\Omega_{max} = v_{\text{tip}_{\text{max}}}/R$ until the power rated is achieved. The power coefficient is obtained by the following optimization problem, solved for each wind speed:

$$\forall V \in \left[V_{II\frac{1}{2}}, V_r\right] \quad C_P^{II\frac{1}{2}} = \max_{\beta} C_P\left(\lambda\left(V\right),\beta\right) \tag{2.11}$$

$$\forall V \in \left[V_{II\frac{1}{2}}, V_r\right] \quad \beta^{II\frac{1}{2}} = \arg\max_{\beta} C_P\left(\lambda\left(V\right),\beta\right) \tag{2.12}$$

In this case the pitch varies along the wind speed, maximizing the extracted power and keeping constant the rotor angular velocity Ω_{max}. The subscript $_r$ identifies the value of the variables when the rated power is attained.

When the rated power P_r is obtained, the region III starts. The regulation sets a power value equal to P_r towards the wind speed, while the power coefficient is varied as:

$$C_P = C_{P_r}\left(\frac{\lambda}{\lambda_r}\right)^3 \tag{2.13}$$

where λ is a function of the wind speed: $\lambda = \overline{\Omega}R/V$, with $\overline{\Omega} = v_{\text{tip}_{\text{max}}}/R$ if constraint (2.1d) is active, or $\overline{\Omega} = \Omega_r$ otherwise. The region III ends at the cut out wind speed or at a wind speed where a down-rated is applied. This last case is not here considered for simplicity.

Although the current section is focused mainly on the evaluation of the AEP, the regulation policy is fundamental to assess also the reference control input to trim the wind turbine. Considering the dynamic simulations, the control input provided by the controller is composed by two parts. The first one is contribution related to the regulation policy that provides the reference conditions. The second one aims at the annulment of the external noise and it is usually related to the gap between the current conditions and the trimmed ones. The tuning of the control system will be briefly considered in Sect. 2.3.5, where the reference conditions are computed by a reduce order model and the automatic evaluation of the gains of a specific control law is reported.

2.3 Structural Optimization of Rotor Blades and Tower

The rotor blade and tower structural design is investigated by the current section. Since the methods are not generally known, a self-contained explanation is reported, highlighting all the characteristics of the approach. Furthermore, the subject of this section is essential to understand the development of the aero-structural design algorithms, reported in Sect. 2.4, where the aerodynamic and the structural design are unified by a monolithic approach.

The structural design procedure is formulated on multiple modeling layers. In the current section, a coarse aeroelastic level is considered. This level relies on numerical efficient models, allowing the application of optimization techniques. At the end of optimization process, a refinement can be applied by a fine modeling level. This level will be reported separately in Sect. 2.5–2.6 because it is not actually an optimization procedure, but it is a useful tool available to the analist.

The exposition is coherent to the description of the aerodynamic optimization of the rotor blades. At the beginning a general overview of the method is reported in Sect. 2.3.1, then the algorithmic form is highlight in Sect. 2.3.2, showing the style of the approach. The structural model parametrization is reported in Sect. 2.3.3, while the cost model is highlighted in Sect. 2.3.4. Since the tuning of the control system is mandatory to evaluate the DLC during structural optimization, Section 2.3.5 focuses the attention on this procedure. Finally the connection between coarse and fine-level is provided by Sect. 2.3.6.

2.3.1 General overview of the optimization method

The structural optimization procedure aims at obtaining the lightest structure that satisfies a set of design requirements, fixing the aerodynamic characteristics, i.e. the external shape of each component and the wind turbine configuration. This procedure can be applied to the rotor blades, the most challenging components at the core of the design process. Obviously, the method can be extended to other structural elements, for example an integrated design of the rotor blades and the tower structure is here reported, completing the discussion of [53]. The structure of the algorithm that pertains only the rotor blades can be easily inferred, excluding from the procedure all the parameters related to the tower.

The algorithm is developed on multiple layers. A coarse aeroelastic level, or “Coarse” level in Fig. 2.3, based on quasi-3D efficient models is applied during the load estimation and the optimization phase, while 3D finite element models are used to refine the

coarse solution in a fine-level, or "Fine" level in Fig. 2.3. The connection between the two levels is performed iteratively, as it will emerge from the following explanation. A parametrized model for blade and tower structure is defined by optimization variables that determine structural properties at a finite number of control stations. The model characteristics between these control stations are obtained by interpolation. The blade optimization variables are the thickness distributions of the constitutive elements along blade span, i.e. external shell, spar caps, shear webs and different reinforcements. A classical tubular solution is considered for the tower: diameter and thickness distribution along the tower height parametrize this component.

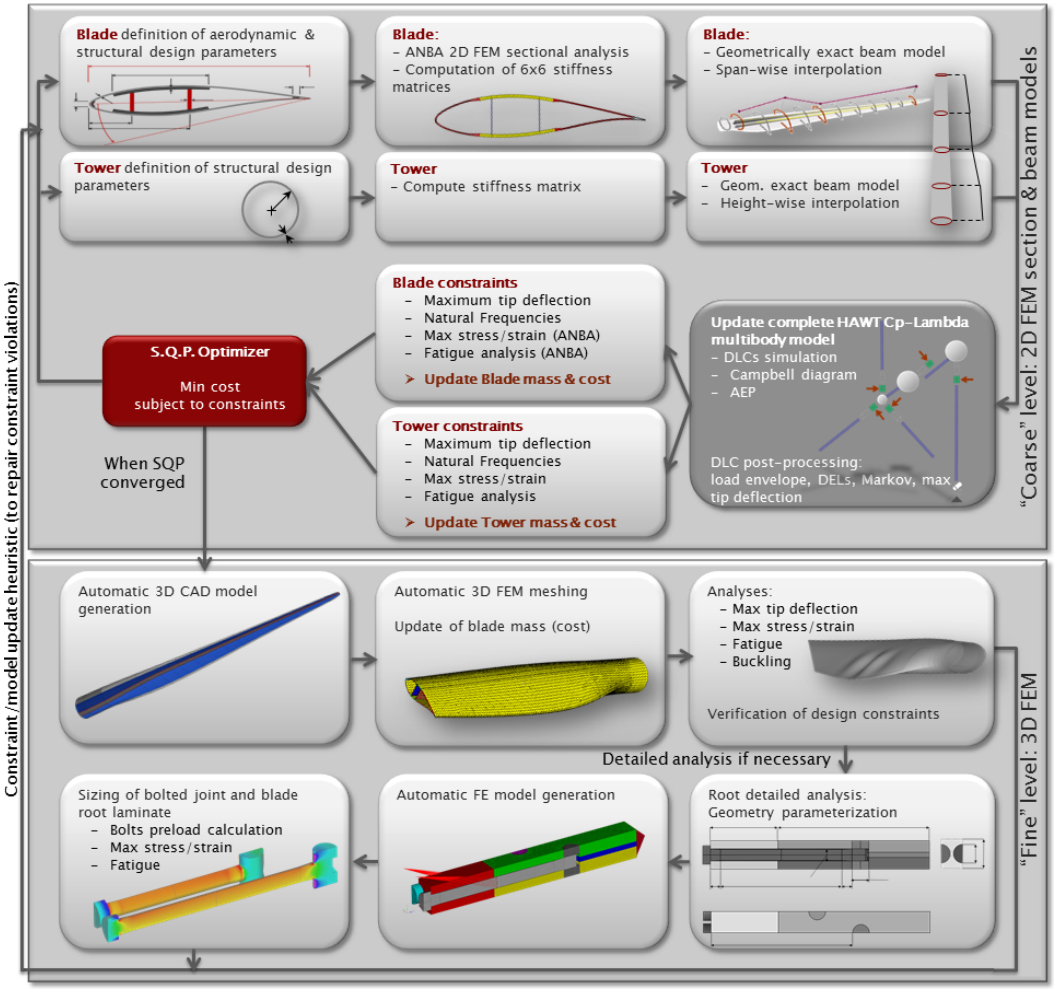

Figure 2.3: *Multi-level structural blade-tower optimization for given aerodynamic shape*

Blade section properties are computed by finite element cross sectional analysis by the software `ANBA` [15]. The discretization is performed by orthotropic equivalent panels. The code computes the fully populated stiffness matrix, accounting for all possible coupling due to the use of composite materials. Moreover, multiplicative coefficients that allow the evaluation of the stress and strain distributions on the blade sections are evaluated. Due to the basic geometry of the tower, the properties and the stress distributions are obtained by classical analytical theory of beam sections. Structural properties are included in the `Cp-Lambda` model, which allows high fidelity simulations as re-

ported in Sect. 2.1.

All Dynamic Load Cases (DLC) prescribed by international standards, [50] or [51], are computed by the simulation environment. The quantities necessary for sizing are obtained automatically by post-processing routines. Ultimate stress and strain distributions are evaluated from the load envelope by `ANBA` on each designed section. Rainflow counting algorithm and damage accumulation rules estimate the fatigue life from stress time histories. It is possible to prevent resonant conditions by placing modal characteristics of the system. The clearance between blade tip and tower is also evaluated, considering machine configuration and blade tip deflection. All these quantities and manufacturing requirements are expressed as inequality constraints enforced during the optimization procedure.

The CoE model is considered as merit figure, allowing the correct scaling of heterogeneous parameters that define the wind turbine [64]. The cost model links the weight to the cost of the blades and tower by statistical coefficients, so a light design turns out to be also cheap. Blade mass is computed considering the structural masses by `ANBA` sectional analysis and different type of nonstructural masses: adhesive, resin uptake, bonding plies, lightning protection system. Also core thickness distribution is estimated by analytical formula as reported in [65] and it is included in the nonstructural mass evaluation. Tower mass is computed summing the contributions due to the external tubular, the flanges that connect different sections and nonstructural masses distributed along tower height. Also the AEP affects the CoE, representing the return obtained by the wind turbine installation. The AEP value is estimated by `CpLambda` from the aerodynamic characteristic of the rotor and the wind turbine configuration as reported in Sect. 2.2.4.

Sequential Quadratic Programming (SQP) techniques are applied to optimize blade and tower structure. During the optimization, the generalized load envelope obtained from DLC is kept constant to reduce computational time and to increase problem regularity. Smoothness of the merit function and constraint equations is a strict requirement when gradient base algorithms are applied. As reported previously, when the aerodynamic optimization is considered, Sect. 2.2, the optimization problem is expected to be smooth in the neighborhood of the optimal solution. This assumption is based on the hypothesis that the optimal blade aerodynamic properties are expected to be regular due to manufacturing constraints. Furthermore in optimal operative condition the aerodynamic loads exhibit a regular behavior with regard to the angle of attack, because the angle of attack is limited and the airfoils are in an operative condition far from stall. The smoothness of the input data and the loads, that characterize the optimal configuration, allow to infer the regularity of the aerodynamic design.

Some problems may arise in the structural optimization, where a non-smooth behavior can be induced by the load envelope evaluation. The sectional load envelope collects maximum and minimum loads conditions acting on each section and it is useful to express requirements on the ultimate stress and strains. The selection of the most severe conditions is carried out for each load component by applying `max` and `min` functions to the load time histories. If the wind turbine model is modified, there is no guarantee that the dimensioning conditions remain identical to the ones of the original model, involving the same time instant and DLC type. A swap into load ranking between DLC type would lead to a discontinuos behavior of the constraint equations, increasing the level

of numerical noise when gradients are evaluated by finite differences, and downgrading the algorithm performance.

The hypothesis of constant load envelope solves the problem of discontinuities in this case but it forces to recover the load variations by an iterative procedure. When an optimal solution is found by SQP algorithm, the wind turbine parametric model is updated and loads are evaluated. A new step of the iterative process is so performed estimating a new optimal configuration from SQP results at the previous iteration and boundary conditions defined by the new load envelope. Usually, the convergence is achieved after few steps, showing a good behavior of the algorithm in different case studies.

The coarse aeroelastic solution is improved by the fine-level reported in Fig. 2.3. At the moment, the refinement analysis can be applied to the blade structure only, but the extension to the tower structure can be implemented directly. A three dimensional CAD blade model is automatically generated, considering the constitutive elements. The CAD model is meshed and it allows to repeat the verifications performed at coarse aeroelastic level. If some differences emerge, the 3D FEM results are used to correct the constraints applied during the Coarse aeroelastic optimization. Corrections are usually identified at the beginning or at the end of blade structural components and where steep chord modifications are reported, i.e. in blade root region. 3D FEM allows also the verification of buckling requirements and it highlights if small corrections of the estimated core thickness are necessary. This process refines the values of nonstructural mass distribution and the blade global mass measure, directly connected to CoE estimation. In the current version of `Cp-Max` the possibility of performing a detailed fully 3D finite element structural analysis is included. The creation of a detailed model is essential to increase the resolution of the analysis, allowing the sizing of structural details that, despite their limited extension, directly affect the global blade configuration. As example, Figure 2.3 considers the blade root bolted joint design that defines the thickness of blade laminate in the root region, affecting blade total mass significantly due to large laminate thickness required to embed the bolts. The connection between the fine-level and the coarse-level is created by scaling the constraints and by updating the merit figure, as reported in Sect. 2.3.6.

2.3.2 Optimization algorithm

The combined algorithm for optimizing the blade-tower structure is shown by the block diagram of Fig. 2.4. The aerodynamic shape is provided by the parameters $\boldsymbol{p}_a$, and it is fixed during the optimization. The DLC estimation and the structural optimization are performed iteratively, as shown by the diagram. The DLC are estimated at first, then the optimization problem is solved, providing a new structural configuration. The DLC can be updated with the new layout, giving new boundary conditions to the optimization problem and so on. When the procedure converges, the optimal structural parameters $\boldsymbol{p}_s$ are provided.

The minimization of the blade-tower cost can be precisely posed in this algorithmic

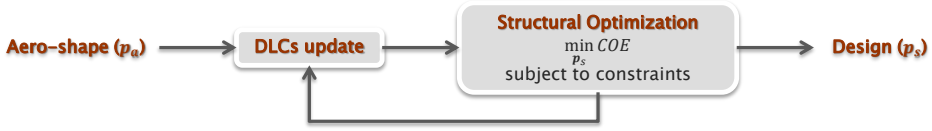

Figure 2.4: *Block diagram of the structural optimization*

form:

$$\textbf{Function } (\boldsymbol{p}_s^*, CoE^*) = \texttt{MinBladeTowerCost}(\boldsymbol{p}_a, \boldsymbol{p}_s, D, \boldsymbol{\Gamma}_s) : \tag{2.14a}$$
$$(\boldsymbol{E}) = \texttt{LoadEnvelope}(\boldsymbol{p}_a, \boldsymbol{p}_s, D), \tag{2.14b}$$
$$\textbf{do} \tag{2.14c}$$
$$(\boldsymbol{p}_{s1}, \boldsymbol{p}_{s2}) = \boldsymbol{p}_s, \tag{2.14d}$$
$$(\boldsymbol{p}_{s1}^*, CoE^*) = \texttt{MinCostBladeTowerFrozenLoads}(\boldsymbol{p}_a, \boldsymbol{p}_{s1}, D, \boldsymbol{E}, \boldsymbol{\Gamma}_s), \tag{2.14e}$$
$$(M) = \texttt{3DCADAndFEMeshGeneration}(\boldsymbol{p}_a, \boldsymbol{p}_{s1}^* \cup \boldsymbol{p}_{s2}, \boldsymbol{E}), \tag{2.14f}$$
$$(\boldsymbol{p}_{s2}^*, w_2^*, \Gamma_s') = \texttt{3DFEAnalysis}(M, \boldsymbol{p}_{s2}, D, \boldsymbol{E}, \boldsymbol{\Gamma}_s), \tag{2.14g}$$
$$\boldsymbol{p}_s^* = \boldsymbol{p}_{s1}^* \cup \boldsymbol{p}_{s2}^*, \tag{2.14h}$$
$$(\boldsymbol{E}') = \texttt{LoadEnvelope}(\boldsymbol{p}_a, \boldsymbol{p}_s^*, D), \tag{2.14i}$$
$$\Delta p_{s1} = \left\| \boldsymbol{p}_{s1}^* - \boldsymbol{p}_{s1} \right\|, \quad \Delta CoE = \| CoE^* - CoE \|, \tag{2.14j}$$
$$\boldsymbol{p}_s = \boldsymbol{p}_s^*, \quad \boldsymbol{\Gamma}_s = \boldsymbol{\Gamma}_s', \tag{2.14k}$$
$$\textbf{while } (\Delta p_{s1} \geq \text{tol}_{p_{s1}} \textbf{ and } \Delta CoE \geq \text{tol}_{CoE}). \tag{2.14l}$$

The inputs of function `MinCostBladeTowerFrozenLoads` are the known parameters $\boldsymbol{p}_a$ describing the aerodynamic shape of the blade, the initial structural parameters $\boldsymbol{p}_s$, the data structure D analogous to (2.3), the load envelope $\boldsymbol{E}$ and a list of parameters $\boldsymbol{\Gamma}_s$ used to impose the design requirements, defined as

$$\boldsymbol{\Gamma}_s = \left(\boldsymbol{\sigma}_{\text{adm}}, \boldsymbol{\epsilon}_{\text{adm}}, \boldsymbol{\delta}_{\text{tip}_{\text{adm}}}, [\boldsymbol{\omega}_{\text{L}}, \boldsymbol{\omega}_{\text{U}}], ... \right) \tag{2.15}$$

where $\boldsymbol{\sigma}_{\text{adm}}$ and $\boldsymbol{\epsilon}_{\text{adm}}$ are the admissible values for ultimate stress and strain, $\boldsymbol{\delta}_{\text{tip}_{\text{adm}}}$ is the allowable blade-tower clearance, $[\boldsymbol{\omega}_{\text{L}}, \boldsymbol{\omega}_{\text{U}}]$ are the bounds for modal frequencies placement and so on.

The outputs of the function are optimum values for the parameters $\boldsymbol{p}_s^*$ that produce minimum Cost of Energy CoE^*. The primary structural parameters $\boldsymbol{p}_{s1}$ are directly included into optimization procedure, while the secondary structural parameters $\boldsymbol{p}_{s2}$, for example blade core distribution, are determined during the refinement cycle (2.14f, 2.14g).

The coarse-level constrained optimization (2.14e), which is solved using the SQP

algorithm, takes the form:

$$\textbf{Function } (\boldsymbol{p}_s^*, CoE^*) = \texttt{MinCostBladeTowerFrozenLoads}(\boldsymbol{p}_a, \boldsymbol{p}_s, D, \boldsymbol{E}, \boldsymbol{\Gamma}_s) : \tag{2.16a}$$

$$\boldsymbol{p}_s^* = \min_{\boldsymbol{p}_s} CoE(\boldsymbol{p}_s, D) \quad (\text{and } CoE^* = \arg\min_{\boldsymbol{p}_s} CoE), \tag{2.16b}$$

$$\text{s.t.:} \quad \boldsymbol{g}_s(\boldsymbol{p}_{s,b}, \boldsymbol{p}_{s,t}) \leq \boldsymbol{0}, \tag{2.16c}$$

$$\boldsymbol{\omega}_b(\boldsymbol{p}_{s,b}, D) \in [\boldsymbol{\omega}_L, \boldsymbol{\omega}_U], \tag{2.16d}$$

$$\boldsymbol{\sigma}_b(\boldsymbol{p}_{s,b}, \boldsymbol{E}, D) \leq \boldsymbol{\sigma}_{\text{adm}}, \tag{2.16e}$$

$$\boldsymbol{\epsilon}_b(\boldsymbol{p}_{s,b}, \boldsymbol{E}, D) \leq \boldsymbol{\epsilon}_{\text{adm}}, \tag{2.16f}$$

$$\boldsymbol{d}_b(\boldsymbol{p}_{s,b}, \boldsymbol{E}, D) \leq \boldsymbol{1}, \tag{2.16g}$$

$$\boldsymbol{\delta}_{\text{tip}_{\text{max}}}(\boldsymbol{p}_{s,b}, \boldsymbol{p}_{s,t}, \boldsymbol{E}, D) \leq \boldsymbol{\delta}_{\text{tip}_{\text{adm}}} \tag{2.16h}$$

$$\boldsymbol{\omega}_t(\boldsymbol{p}_{s,t}, D) \in [\boldsymbol{\omega}_L, \boldsymbol{\omega}_U], \tag{2.16i}$$

$$\boldsymbol{\sigma}_t(\boldsymbol{p}_{s,t}, \boldsymbol{E}, D) \leq \boldsymbol{\sigma}_{\text{adm}}, \tag{2.16j}$$

$$\boldsymbol{d}_t(\boldsymbol{p}_{s,t}, \boldsymbol{E}, D) \leq \boldsymbol{1}. \tag{2.16k}$$

The structural variables $\boldsymbol{p}_{1s}$ are divided into the variables pertaining the blade structure and the variables that describe the tower and each group is identified by the subscript b and t respectively. The same notation is applied to the set of design requirements expressed by inequalities (2.16c – 2.16k), among which different constraints can be identify:

- (2.16c): requirements applied during constructive process. For example limits on the tower cone angle or thickness variations in the same tower sectors can be imposed. Considering the blade, span-wise ply tapering rates in lamination sequences can be limited, due to manufacturing considerations.
- (2.16d, 2.16i): resonant conditions are avoided placing significant natural frequencies within a desired interval $[\omega_L, \omega_U]$. This could be a requirement for the first flap-wise blade eigenfrequency to lie above the three-per-rev frequency at the rated rotor speed, or a requirement for a suitable gap between two consecutive blade frequencies. If the tower is considered, the first fore-aft and side-side bending modes could be located above one-per-rev frequency at the rated rotor speed. Usually the other per-rev frequencies do not concern the tower design since the gap with the lower eigenfrequencies of the tower is significant.
- (2.16e,2.16f, 2.16j): sufficient structural strength is obtained for the blade imposing bounds on stress and strain components $\boldsymbol{\sigma}$ and $\boldsymbol{\epsilon}$, respectively, at a selected number of points on cross sections of interest, according to [50, 51]. The considered components on each blade section are the longitudinal, the transversal and the shear stresses or strains. Von Mises stress is considered for the tower instead, as suggested in [66]. The stress and strain measurements depends on the optimization parameters $\boldsymbol{p}_s$, the input data D and the generalized load envelope $\boldsymbol{E}$. Safety factors on material and on loads are included consistently with [50, 51].

- (2.16g, 2.16k): bounds on fatigue induced damage when DLC 1.2 turbulent wind field is applied [50]. At the beginning the fatigue analysis is performed on overall verification points on each blade section. Then the most critical points are selected by a user defined tolerance to limit the computational cost during the optimization. On each verification point the fatigue damage d_{σ_r} due to single stress component is computed according to [51]:

$$d_{\sigma_r} = \sum_{i,j,k} F_{V_k} \frac{n\left(\sigma_{m_i}, \sigma_{a_j}, V_k\right)}{N\left(\sigma_{m_i}, \sigma_{a_j}, \sigma_{adm}, \gamma\right)} \tag{2.17}$$

  where F_{V_k} is given by the ratio between the time spent by the wind turbine during the entire operative life at wind speed V_k and the simulated time. $n\left(\sigma_{m_i}, \sigma_{a_j}, V_k\right)$ is the number of cycles obtained by the rain-flow counting algorithm at mean stress σ_{m_i}, amplitude stress σ_{a_j} and wind speed V_k. The admissible number of cycles is $N\left(\sigma_{m_i}, \sigma_{a_j}, \sigma_{adm}, \gamma\right)$, corrected by the safety factor γ, [51]. From the value of d_{σ_r} of each stress component, a multi-axial damage index is defined in agreement with [67, 68]:

$$d_b = d_{\sigma_1}^{2/m} + d_{\sigma_1}^{2/m} - (d_{\sigma_1} d_{\sigma_2})^{1/m} + d_{\sigma_6}^{2/m}, \tag{2.18}$$

  where m is the inverse slope of the Wöhler curve and the longitudinal, transverse and shear stress components are identified by indices 1, 2 and 6. For the tower the fatigue constraint implies the computation of the d_t index as stated by [69]:

$$d_t = \left(\frac{\gamma_{Ff} \Delta\sigma_{E,2}}{\Delta\sigma_c / \gamma_{Mf}}\right)^3 + \left(\frac{\gamma_{Ff} \Delta\tau_{E,2}}{\Delta\tau_c / \gamma_{Mf}}\right)^5 \tag{2.19}$$

  where $\Delta\sigma_c$ and $\Delta\tau_c$ are reference values of fatigue strength, $\Delta\sigma_{E,2}$ and $\Delta\tau_{E,2}$ are equivalent constant amplitude stress ranges related to 2 million cycles and γ_{Ff} and γ_{Mf} are safety factors. The damage indices for all verification points are stacked in vectors, $\boldsymbol{d}_b$ and $\boldsymbol{d}_t$ and are all bounded to unity. Also for the fatigue the dependency on the $\boldsymbol{p}_s$, D and $\boldsymbol{E}$ is highlighted. It should be remembered that the generalized load envelope $\boldsymbol{E}$ includes also the DLC 1.2 turbulent conditions, essential to evaluate $\boldsymbol{d}_b$ and $\boldsymbol{d}_t$.

- (2.16h): ensures the blade-tower clearance during operative life. Before performing the blade structural optimization, the load condition, that generate the minimum clearance, is identified among the DLC. Considering this snapshot, the equivalent static load approach is applied to evaluate a static load distribution useful to evaluate the minimum clearance requirement. This distributed load generates a displacement of the blade axis equal to the measured one, when it is applied together with the inertial and gravitational load of the minimum clearance condition. This procedure can be useful employed in optimization of mechanical systems to reduce the computational cost, performing static analyses instead of dynamic analyses [70, 71]. In this project the equivalent static loads are evaluated as follow. The span-wise loads $\boldsymbol{l}(\eta)$ are expressed as product between shape functions $\boldsymbol{n}_l(\eta)$ and nodal values $\boldsymbol{l}$. The optimal nodal values $\boldsymbol{l}^*$ are computed minimizing the difference between the internal forces $\hat{\boldsymbol{s}}$, of the equivalent static

problem, and the internal forces $\boldsymbol{s}$, measured during the dynamic analysis. Solving the optimization problem, it is imposed that the beam axis displacement $\hat{\boldsymbol{\delta}}$ of the equivalent static problem is similar to the measured displacement $\boldsymbol{\delta}$ by a user define tolerance ϵ. The optimization problem can be stated as:

$$\boldsymbol{l}^* = \arg\min_{l} \sum_{j=1}^{N} \frac{\left\|\hat{\boldsymbol{s}}^j(\boldsymbol{l}) - \boldsymbol{s}^j\right\|}{\|\boldsymbol{s}^j\|}, \tag{2.20}$$

$$\text{s.t.} \quad \frac{\left\|\hat{\boldsymbol{\delta}}^j(\boldsymbol{l}) - \boldsymbol{\delta}^j\right\|}{\|\boldsymbol{\delta}^j\|} \leq \epsilon, \quad j = 1 \dots N \tag{2.21}$$

where j identifies the sections at different blade span location and N is the total number of blade sections. The equivalent static loads are included into the generalized load envelope $\boldsymbol{E}$, as suggested by the arguments of $\boldsymbol{\delta}_{\text{tip}_{\text{max}}}$. At each modification of the structural model, a static analysis is performed applying the equivalent static loads together with the inertial and gravitational loads due to the rotor angular velocity and azimuthal position of the maximum tip displacement condition. During $\boldsymbol{\delta}_{\text{tip}_{\text{max}}}$ estimation, the inertial and gravitational loads are updated taking into account the mass variation of the blade.

At the end of coarse structural optimization, a refinement analysis can be applied. This analysis starts with the generation of refined three-Dimensional (3D) Finite Element Model (FEM) as reported by the function (2.14f) that returns the model M as output. A complete description of the creation of 3D FEM is reported in Sect. 2.5–2.6, explaining the procedure of `3DCADAndFEMeshGeneration`. The refinement analysis is represented by (2.14g) and it can be stated in the following algorithmic form:

$$\textbf{Function } (\boldsymbol{p}^*_{s2}, w^*_2, \Gamma'_s) = \texttt{3DFEAnalysis}(M, \boldsymbol{p}_{s2}, D, \boldsymbol{E}, \Gamma_s) : \tag{2.22a}$$

$$(\boldsymbol{p}^*_{s2}, w^*_2) = \texttt{MinSecondaryWeight}(M, D, \boldsymbol{E}), \tag{2.22b}$$

$$\Gamma'_s = \texttt{ConstraintVerificationAndUpdate}(M, D, \boldsymbol{E}, \Gamma_s), \tag{2.22c}$$

and comprises of two main steps.

The first, (2.22b), concerns the design of secondary structural parameters, in this case represented by the skin core thickness with respect to local buckling. A buckling free-configuration is obtained, refining core thickness distribution along the blade span. This problem yields the optimal values of the secondary variables $\boldsymbol{p}^*_{s2}$, as well as an improved estimate for the blade mass $w^* = w^*_1 + w^*_2$, so the CoE^* measurement. The buckling analysis in itself can be formulated as the following constrained optimization:

$$\textbf{Function } (\boldsymbol{p}^*_{s2}, w^*_2) = \texttt{MinSecondaryWeight}(M, D, \boldsymbol{E}) : \tag{2.23a}$$

$$\boldsymbol{p}^*_{s2} = \min_{\boldsymbol{p}_{s2}} W_2(M, D) \quad (\text{and } \; w^*_2 = \arg\min_{\boldsymbol{p}_{s2}} W_2), \tag{2.23b}$$

$$\text{s.t.:} \quad \boldsymbol{\lambda}(M, D, \boldsymbol{E}) \geq 1, \tag{2.23c}$$

where $\boldsymbol{\lambda}$ are the eigenvalues of the linearized buckling problem associated with the loading conditions stored in the generalized envelope $\boldsymbol{E}$. Further details on the solution of this problem are given in Sect. 2.5.4, where the method applied to estimate the core distribution at coarse-level is also reported.

The second step, (2.22c), implies the evaluation of the all design verifications included in the coarse optimization procedure. If some violations are identified, the constraint equations bounds are updated by the generation of the vector Γ'_s, as reported in Sect.2.3.6. The 3D FEM verifies the following design requirements:

- verification of the eigenfrequency related to the coarse-level inequalities (2.16d, 2.16i);
- limits on stress and strain components, connected to the coarse-level requirements (2.16e, 2.16f, 2.16j);
- fatigue damage index, related to the coarse-level level verification (2.16g, 2.16k);
- minimum blade-tower clearance, associated to the coarse-level requirement (2.16h).

Resolution of 3D FEM might not be sufficient and further examinations might be required in highly critical regions of the blade. Some examples of these regions are the blade root bolted joint, the trailing edge and the shear webs start. Increasing the resolution is possible by fully three dimensional detailed finite element analysis, as briefly reported in Sect. 2.6. The results of these analyses can be included in the coarse-level by the same procedure described for the 3D FEM of the entire blade.

2.3.3 Model Parametrization

The structural parametrization provides a description of the geometry and the definition of the structural properties of the materials. Considering the blade the following data must be provided:

- the airfoils type and span-wise position along the blade axis. This information is complemented by the definition of the three-dimensional shape of the lifting line and by the distributions of chord and twist along the blade span.
- a description of the internal geometry of the blade section. The chord-wise and span-wise position of the structural components, such as spar caps, shear webs and internal reinforcements, must be defined. Three different sectional layouts are reported in Fig. 2.5, where distinct configurations of the spar caps and the shear webs are shown. Furthermore, the orientation of the shear webs must be defined. Usually straight shear webs, orthogonal to the line of the maximum chord section, are preferred, but also twisted webs can be created, orthogonal to the local sectional chord. Each section is modeled by equivalent panels provided by the cross-sectional analysis software [15], so parameters that manage the mesh density are provided too. The mesh density is related to the estimation of the structural properties and it defines the number of points where the evaluation of the stress and strain on each section is performed.
- the lamination sequence of each component and the necessary material properties. Also nonstructural mass is considered, including contributions per-unit of span and per-unit of surface.

The geometry and the material properties must be provided also for the tower. Considering a classical steel tubular tower, the diameter and the thickness of the tubular

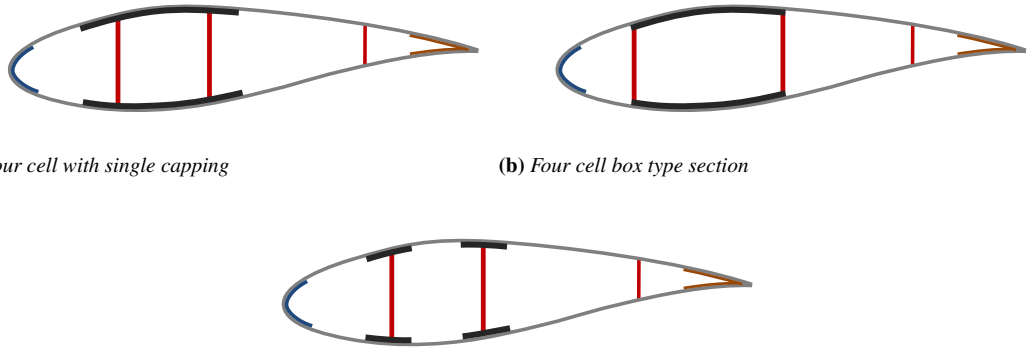

(a) *Four cell with single capping*

(b) *Four cell box type section*

(c) *Four cells with double spar caps and three shear webs*

Figure 2.5: *Rotor blade cross section layouts*

shell describe the geometry of the structure. The tower structure is defined as a finite number of sectors due to portability considerations. The inertial properties of the connection flanges between tower sectors can be provided as input data. Nonstructural mass is expressed as function of the span coordinate, while the material is linear and isotropic.

The optimization parameters pertaining the blade $\boldsymbol{p}_{s,b}$ are the thickness of the external shell, spar caps, shear webs and reinforcements at a finite number of span-wise locations, while the values among these sections are recovered by linear interpolation. The chord-wise position of the shear webs and the chord-wise extension of the spar caps can be optimized too. These properties are parametrized by varying the coordinates that express the chord-wise position of the shear webs and the extension of the spar caps at span boundaries of these structural components. The global configuration is retrieved by linear interpolation of the values at the boundaries. The span-wise extension of the structural components is fixed and it can be investigated by parametric studies. Although this approach leads to a partial optimization of the blade geometry because it allows the description of a precise structural configuration, it has been successfully applied to design a wind turbine aeroelastic model for wind tunnel applications [14]. Furthermore, the regular description of the structural components meets the manufacturing requirements that affect the blade geometry, limiting the production cost. Although this feature is available, it has not been used in the current project to simplify the approach. On the other hand, the most general formulation of topology optimization can not be considered by the current implementation. Considering the topology optimization, the most complicated aspects are the multiple load conditions and numerous design requirements that increase the problem complexity.

The parameters $\boldsymbol{p}_{s,t}$ related to the tower are the diameter and the thickness values of the steel shell at a finite number of tower sections, also in this case this discrete values are linearly interpolated along the entire height.

Manufacturing constraints can be expressed by geometric conditions between the elements of $\boldsymbol{p}_s$, included during the optimization by (2.16c). By these constraints, for example, the thickness of a tower sector can be imposed constant, or the same thickness distribution can be set on the lower and upper spar caps.

Starting from the structural parametrization, two different analyses are performed. The structural and inertial characteristics of the MB model must be evaluated at first, to allow `Cp-Lambda` analyses. After computing the generalized load envelope E using the MB analyses, all the measurements to evaluate the design requirements must be recovered. Considering the tower, both analyses are performed by analytical approach due to the simple structural layout. If the blade is examined, cross-sectional analysis of the software `ANBA` is performed. `ANBA` evaluates the sectional properties of the blades, giving the fully coupled stiffness matrix and the inertial blade properties. Also global sectional properties such as centroid location, shear center position and principal axes orientation are obtained. Furthermore, the software provides the recovery relations between the internal forces, computed by the DLC evaluation, and the stress and strain distribution on each blade section. By this procedure, it is possible to evaluate the constraints on ultimate loads and fatigue damage for both components.

2.3.4 Cost Function

A cost of energy model is considered as merit figure, providing various advantages than a cost function based on physical measurement. First, the CoE model merges in a single measurement all the parameters that define the wind turbine. Standard optimization techniques can be applied, avoiding the use of the multi-objective design. Furthermore, it allows to investigate the optimal design of the overall configuration of the wind turbine, aiming at a holistic design where all the wind turbine parameters are designed by a monolithic procedure.

Second, it gives a general indication about the optimality of the design. This index allows to compare also different layouts, providing information that could be difficult to find looking at technical data.

The cost model developed by National Renewable Energy Laboratory (NREL) is chosen as merit figure [64]. The Cost of Energy (CoE) can be expressed by the following equation:

$$\mathrm{CoE} = \frac{\mathrm{FCR}\ \mathrm{ICC}(p)}{\mathrm{AEP}(p)} + \mathrm{AOE}(p) \tag{2.24}$$

where:

- the Fixed Charge Rate (FCR) is the amount of monetary unit per year of initial capital cost needed to cover the capital cost and other fixed charges.
- the Initial Capital Cost (ICC) is the sum of cost of the wind turbine and the balance of station cost. This item includes the contributions of the rotor, drive train, nacelle, tower, control system, and balance of station. Further elements are included if an offshore wind turbine is considered.
- AEP is the annual energy production
- AOE are the Annual Operating Expenses

$$\mathrm{AOE} = \mathrm{LLC} + \frac{\mathrm{O\&M\ LCR}}{\mathrm{AEP}(p)} \tag{2.25}$$

with

- the Land Lease Cost (LLC), that takes into account the lease cost payed for the turbine installation
- the Operation and Maintenance cost (O&M), that considers the scheduled and unscheduled maintenance, but also the labor, the administration and the supplies related to the maintenance
- the Levelized Replacement Cost (LRC), that splits the cost of major replacements over the operational life of the wind turbine

finally p are the design parameters.

When the structural optimization is considered, the cost model weights the blades structural parameters and the tower structural parameters to obtain the best trade-off between the layout of the two structures. The design affects only the ICC, where the cost of the two components is included. The blades and the tower costs are obtained by scaling the mass of each component by statistical regressions.

Notice that there is a strong coupling in the CoE model between the aerodynamic design, that affects the AEP, and the structural design, that influences the ICC. For example, fixing all the aerodynamic parameters, except the blade chord, it is possible to increase the aerodynamic efficiency reducing the blade solidity. However, if the airfoils type and their positions along the blade span are fixed, the blade relative thickness is fixed. Therefore a chord reduction causes a decrease of the blade thickness, a diminution of the structural efficiency and an increase of the blade mass/cost to satisfy the design requirements. On the other hand, if the solidity augments, the blade thickness increases, but the advantages in term of structural efficiency could be limited by the buckling requirement. Indeed, the growth of the solidity implies large external shell panels that can be subjected to buckling. The coupling between the aerodynamics and the structure is only outlined here, but it will emerge clearly when the aero-structural optimization results will be considered in Sect.3.4, where further considerations will be reported.

2.3.5 Tuning of Control System

The structural design is based on the DLC evaluation by `Cp-Lambda` analyses, so an external control law must be provided to regulate the MB model. The external controller has to satisfy various requirements. The first one is the fulfillment of the reference conditions imposed by the regulation policy. This requirement is the most important one because it is related to the power production and to the AEP accordingly. Other requirements, such as load alleviation or increasing of the structural damping, can be considered. Furthermore, if the controller is included into an optimization procedure, an automatic tuning method should be provided to update the controller at each model instantiation. This procedure should be robust, giving satisfactory performance without user intervention. For simplicity, it is more advisable that a single controller is used all along the operative range from the cut-in to the cut-out wind speed. Obviously, if a sufficiently robust controller is provided as initial guess, a sub-optimal design can be accomplished without considering the control laws updating. Both approaches are applied in the current project, depending on the provided initial data and other design considerations as will emerge during the analysis of the results in Sect. 3.

If the control laws are updated at each DLC evaluation, a collective-pitch wind scheduled Linear Quadratic Regulator (LQR) is considered [62]. This choice is based on the internal know-how of the POLI-Wind research group and it is a good trade-off between completeness and simplicity of the approach. The LQR is a model based controller, directly tuned on a reduced order model that is available at each machine instantiation. For this reason, the controller can be updated automatically when the wind turbine model is modified. Furthermore, the LQR is a Multi-Input Multi-Output (MIMO) controller that is able to provide the regulation all along the operative range. Looking at the different operative regions,

- a variable torque–constant pitch strategy characterizes the region II;
- a variable torque–variable pitch logic is applied in region region $\mathrm{II}\frac{1}{2}$;
- a constant torque–variable pitch regulation interests the region III.

The full-state LQR is tuned considering the linearization at each operative condition of a nonlinear reduced order model. The nonlinear model includes tower fore-aft motion, actuators dynamic and drive train shaft dynamic and it is represented by the following equations:

$$M_T\ddot{d} + C_T\dot{d} + K_T d - F_a\left(\Omega, \beta_e, V_w - \dot{d}, V\right) = 0 \tag{2.26}$$

$$\left(J_{LSS} + J_{HSS}\right)\dot{\Omega} + T_l\left(\Omega\right) - T_a\left(\Omega, \beta_e, V_w - \dot{d}, V\right) = 0 \tag{2.27}$$

$$\ddot{\beta}_e + 2\xi\omega\dot{\beta}_e + \omega^2\left(\beta_e - \beta_c\right) = 0 \tag{2.28}$$

$$\dot{T}_{el_e} + \frac{1}{\tau}\left(T_{el_e} - T_{el_c}\right) = 0 \tag{2.29}$$

The first equation represents the tower dynamic where d is the fore-aft motion of the tower top and F_a is the aerodynamic longitudinal force. The M_T, C_T and K_T are modal mass, damping and stiffness of the tower obtained by a modal reduction of a finite element model of the tower structure. The second equation expresses the drive train dynamic: Ω is the rotor angular velocity, T_l is the torque due to mechanical loss and T_a is the aerodynamic torque. J_{LSS} and J_{HSS} are the contributions to the overall rotor inertia relative to the low speed shaft and to the high speed shaft. T_{el_e} and β_e are the electrical torque and the collective-pitch obtained by the last two equations that express the dynamic behavior of the actuators, filtering the required input torque T_{el_c} and collective-pitch β_c. V_w is the instantaneous wind speed, that accounts the turbulent fluctuations, while V is the mean hub wind speed. A picture of the model is reported in Fig. 2.6, while further details are available in [62].

The aerodynamic torque T_a and the aerodynamic force F_a are computed as:

$$T_a = \frac{1}{2}\rho A R \frac{C_P\left(\lambda, \beta_e, V\right)}{\lambda}\left(V_w - \dot{d}\right)^2 \tag{2.30}$$

$$F_a = \frac{1}{2}\rho A C_F\left(\lambda, \beta_e, V\right)\left(V_w - \dot{d}\right)^2 \tag{2.31}$$

where ρ is the air density, A is the rotor area, R is the rotor radius and λ is the tip speed ratio. The aerodynamic coefficients C_P and C_F are known by look up tables and they are obtained by static Cp-Lambda analysis as reported in Sect. 2.2.4. Since C_P and C_F

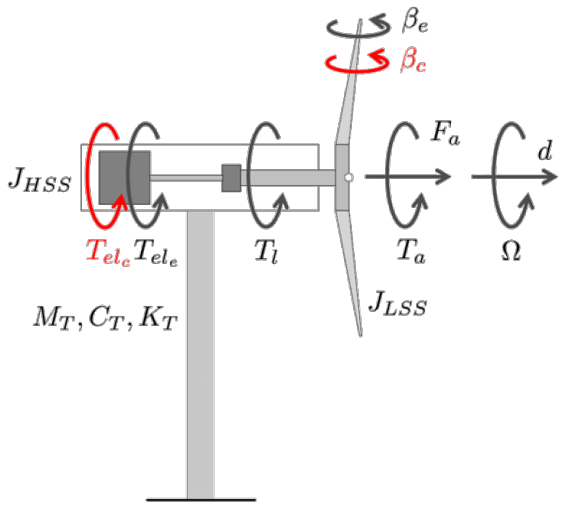

Figure 2.6: *Reduced order model to tune LQR control law*

are evaluated by a complete aero-servo-elastic model, they represent the detailed wind turbine model at a reduce computational cost.

The LQR tracks the reference states obtained by the definition of the regulation policy reported in Sect. 2.2.4. The control gains and the reference states are computed all along the operative range and they are scheduled by hub-height wind value. This value is obtained by filtering the measurement of an on-board anemometer, or by applying an observer as reported in [72]. Also other parameters, which are required by full-state feedback LQR, can be estimate by state observers. This approach has been developed and successfully validated on multiple test cases [72]. However to limit the complexity, the observers are not included in the current design procedure. The measurements are obtained by dummy sensors that will be replaced by the observed outputs on the real wind turbine. Since the observers have proved a robust behavior, this simplification does not affect the generality of the results.

2.3.6 Closure of Multi-level Optimization Loop

The connection between the optimization layers is performed by an updating procedure of the design requirements at coarse-level, considering the results provided by the fine-level. The basic idea is that the results of the two levels differ slightly, so scaling the constraints is a heuristic way to include at coarse-level the 3D effects that only a complete finite model can capture. Notice that the design requirements are always evaluated at the fine-level by considering the original admissible values, i.e. the initial values of $\mathbf{\Gamma}_s$. The constraints scaling procedure is a method to include the three dimensional effects in the cross sectional analysis and beam model. Since these effects are naturally included in the 3D FEM, no correction must be applied.

If the verification of the constraint equations on the fine-level model performed in (2.22c) reveals that some design inequalities are not satisfied, the constraints are modified proportionally to the violation amount. Assume that a condition for maximum stress $\sigma_{\text{max},2D}$ is satisfied at a given section $\sigma_{\text{max},2D} < \sigma_{\text{adm}}$ at the end of the ith coarse-level optimization, but it is violated when the fine-level 3D analysis is performed, i.e. $\sigma_{\text{max},3D} > \sigma_{\text{adm}}$. Then the admissible stress for the $(i+1)$th iteration is

modified as

$$\sigma_{\text{adm}}^{(i+1)} = s_\sigma \, \sigma_{\text{adm}}^{(i)}, \tag{2.32}$$

where $s_\sigma = \sigma_{\max,2D}/\sigma_{\max,3D}$. This way, a more stringent constraint condition is imposed at the next coarse-level iteration. It may be expected that the stress ratio between the quasi-3D and the 3D analyses is almost constant for moderate variations of the structural element sizes. Therefore, the present approach may be used for refining the coarse-level analysis according to the results from the fine-level solution. The other constraint parameters Γ_s are handled in a similar way, so that the full set of constraint limits may be updated as

$$\boldsymbol{\Gamma}_s' = \boldsymbol{S}\boldsymbol{\Gamma}_s, \tag{2.33}$$

where $\boldsymbol{S}$ is a diagonal matrix containing the constraint limit modification factors $s_{(\cdot)}$ for each of the constraint conditions.

2.4 Aero-structural Optimization of Rotor Blades

Better aero-structural configuration of rotor blades can be achieved if aerodynamics and structural properties are considered by a unified design process. The aero-structural optimization allows to define the best compromise, weighing different factors to obtain the best performance in terms of merit figure. In Sect. 2.4.1, a sequential application of the aerodynamic and structural design shows the limits of the mono-disciplinary optimization and it highlights the importance of developing coupled aero-structural design techniques. In the other sections, different aero-structural optimization algorithms are developed based on various simplifications due to the complexity of the problem. The Pre-Assumed Aerodynamic Shape (PAAS) approach is presented at first in Sect. 2.4.2, the External Aerodynamic/Internal Structure (EAIS) approach is then reported in Sect. 2.4.3, while the Monolithic with Load Updating (MLU) approach is finally shown in Sect. 2.4.4. The algorithmic formulation and a general description will be reported for each method.

2.4.1 Limits of direct application of aerodynamic and structural optimization techniques

Given the aerodynamic and structural optimization algorithms described in Sects. 2.2 and 2.3 respectively, the simplest possible approach to an aero-structural optimization of the rotor would consist of stacking in sequence the aerodynamic optimization and the structural optimization. However, this method may produce sub-optimal design solutions and this section aims at highlighting the limits of this approach by means of a simple example.

The pure aerodynamic optimization has firstly the crucial limit that the blades stiffness is not updated from one iteration to the other. This implies that the aeroelastic effects due to the finite stiffness of the rotor cannot be properly taken into account leading to a fictitious behavior of the wind turbine and therefore to an erroneous estimation of the power performance. The estimation of the AEP can then only be considered as an estimate. Moreover, an even more critical aspect of applying separately the aerodynamic and the structural optimization techniques lies in the fact that the optimization is likely to degenerate if the structural efficiency is not considered during the aerodynamic

optimization. Given a set of frozen structural parameters $\boldsymbol{p}_s$, the optimization function `MaxAEP` expressed in Eq. 2.1 tends indeed to favor low values for rotor solidity achieving higher C_p at higher λ. The optimal aerodynamic performance is found at the best trade-off point between a higher C_p and a larger region $II\frac{1}{2}$. This can be well visualized in Fig. 2.7a, where the aerodynamic optimization was run using as starting point the DTU 10MW RWT wind turbine, which is presented and discussed in Sect. 3.2.1. The aerodynamic optimization was run with 4 optimization variables for chord length $\boldsymbol{p}_{a,c}$ and 4 for twist angle $\boldsymbol{p}_{a,t}$, at non-dimensional blade span η equal to 0.2, 0.4, 0.6 and 0.8 respectively. Outside this range, $\boldsymbol{p}_{a,c}$ and $\boldsymbol{p}_{a,t}$ were not allowed to vary. The maximum allowable chord was kept constant and equal to 6.26 m. The aerodynamic optimum, referred as "Aero Optimum" in Fig. 2.7, has a significant lower rotor solidity. Minor modifications are instead imposed to the twist distribution.

However, given the frozen set of airfoil AF, a low chord distribution also implies a low thickness distribution. This means that very thick structural elements become required in order to achieve the design bending stiffness of the blades, see Fig. 2.7b. Therefore, the final design of this simple optimization approach results in a design with very high values of AEP but also a dramatically high mass distribution. The evaluation of the CoE would highlight the sub-optimality of the solution of this approach for the aero-structural optimization.

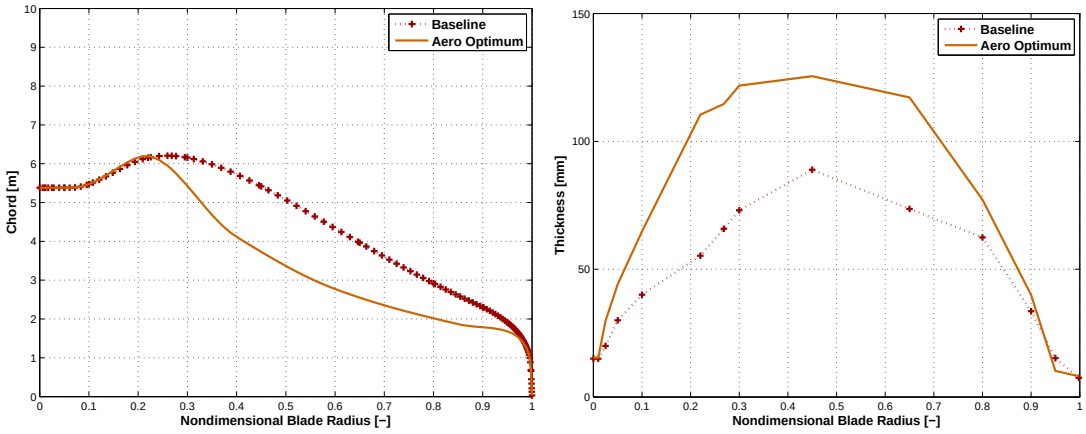

(a) *Chord distribution comparison* **(b)** *Spar caps thickness distribution comparison*

Figure 2.7: *Results from uncontrained aerodynamic optimization followed by structural optimization*

The degeneration of the problem can be prevented by iterating few times between the aerodynamic and the structural loops and by using an a posteriori addition of constraints on maximum chord and minimum solidity. It is clear however that more rigorous methods are needed, where the optimization algorithm can automatically handle all the couplings between $\boldsymbol{p}_a$ and $\boldsymbol{p}_s$ and incorporate all the linear and nonlinear constraints $\boldsymbol{g}$ in the formulation.

2.4.2 Pre-Assumed Aerodynamic Shape approach

Conceptually, the easiest aero-structural approach consists of generating a parametric family of aerodynamic shapes, running the subsequent structural optimization routines and finally evaluating the CoE produced by each design. A response surface can be

evaluated on the outputs of the structural design, establishing a connection between the CoE values and the user-defined aerodynamic parametrization. The aerodynamic configuration with the minimum CoE can be identified on the response surface. Considering the minimum CoE aerodynamic layout, the structural optimization provides the structural design of the aero-structural configuration. The block diagram of the PAAS approach is reported in Fig. 2.8, showing a similar framework to the one reported in Fig. 2.4. This analogy originates from the definition of the PAAS method, that involves the sequential application of the aerodynamic and structural optimization.

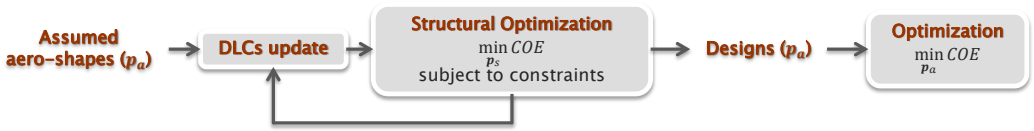

Figure 2.8: *Block diagram of the PAAS optimization*

The approach here reported is similar to a previous study developed in [14], with few key differences. In [14], a small family of aerodynamic shapes was generated by an iterative loop between AEP maximization and blade tapering τ constraint update. For each result of the aerodynamic loop, a structural optimization was run and the ratio AEP to blade mass was evaluated. In this work a different approach is followed. Firstly, the merit figure is now the CoE. Secondly, a family of aerodynamic shapes, here described by subscript index $_i$, is created as a function of rotor solidity σ and maximum chord c_{max}. The new goal is to better sample the space of aerodynamic solutions and to identify more accurately the aero-structural optimum. The algorithm can be described

thanks to the following formalism:

$$\textbf{Function } (\boldsymbol{p}_a^*, \boldsymbol{p}_s^*, CoE^*) = \texttt{PAASOptimization}(\boldsymbol{p}_a, \boldsymbol{p}_s, D, \boldsymbol{\Gamma}_s) : \tag{2.34a}$$
$$\textbf{for } i = 1 : n \tag{2.34b}$$
$$(\boldsymbol{p}_{a_i}^*, P_{y_i}^*) = \texttt{MaxAEP}(\boldsymbol{p}_a, \boldsymbol{p}_s, D), \tag{2.34c}$$
$$\text{s.t.:} \quad \boldsymbol{g}_a(\boldsymbol{p}_a) \leq 0, \tag{2.34d}$$
$$\sigma \geq \boldsymbol{\sigma}_i, \tag{2.34e}$$
$$c \leq c_{max_i}. \tag{2.34f}$$
$$(\boldsymbol{p}_{s_i}^*, CoE_i^*) = \texttt{MinBladeCost}(\boldsymbol{p}_{a_i}^*, \boldsymbol{p}_s, D, \boldsymbol{\Gamma}_s), \tag{2.34g}$$
$$\text{s.t.:} \quad \boldsymbol{g}_s(\boldsymbol{p}_s) \leq 0, \tag{2.34h}$$
$$\boldsymbol{\omega}(\boldsymbol{p}_s, D) \in [\boldsymbol{\omega}_L, \boldsymbol{\omega}_U], \tag{2.34i}$$
$$\boldsymbol{\sigma}(\boldsymbol{p}_s, \boldsymbol{E}, D) \leq \boldsymbol{\sigma}_{\text{adm}}, \tag{2.34j}$$
$$\boldsymbol{\epsilon}(\boldsymbol{p}_s, \boldsymbol{E}, D) \leq \boldsymbol{\epsilon}_{\text{adm}}, \tag{2.34k}$$
$$\boldsymbol{d}(\boldsymbol{p}_s, \boldsymbol{E}, D) \leq \mathbf{1}, \tag{2.34l}$$
$$\boldsymbol{\delta}_{\text{tip}_{\text{max}}}(\boldsymbol{p}_s, \boldsymbol{E}, D) \leq \boldsymbol{\delta}_{\text{tip}_{\text{adm}}}. \tag{2.34m}$$
$$\textbf{end} \tag{2.34n}$$
$$(CoE^*, \sigma^*, c_{max}^*) = \texttt{minCoE}(\boldsymbol{CoE}, \boldsymbol{\sigma}, \boldsymbol{c}_{max}), \tag{2.34o}$$
$$(\boldsymbol{p}_a^*, P_y^*) = \texttt{MaxAEP}(\boldsymbol{p}_a, \boldsymbol{p}_s, D) \quad \text{with} \quad \sigma = \sigma^*, c = c_{max}^*; \tag{2.34p}$$
$$(\boldsymbol{p}_s^*, CoE^*) = \texttt{MinBladeCost}(\boldsymbol{p}_a^*, \boldsymbol{p}_s, D, \boldsymbol{\Gamma}_s). \tag{2.34q}$$

The iterative loop stacks in sequence the generation of n optimal aerodynamic shapes, produced by equation (2.34c), for a given set of constraints $\boldsymbol{g}_a$, described by equation (2.34d), as a function of minimum solidity and maximum chord, described by equations (2.34e) and (2.34f) respectively. The function (2.34g) performs the blade mass minimization for each given set of aerodynamic parameters $\boldsymbol{p}_{a_i}^*$ and it is just a simplified version of the function `MinBladeTowerCost` described in equations (2.14). This is represented in equations (2.35) where only the blade structure characterized by $\boldsymbol{p}_{s,b}$ is optimized, while the tower parameters $\boldsymbol{p}_{s,t}$ are kept constant. This can be formally expressed as:

$$\textbf{Function } (\boldsymbol{p}_s^*, CoE^*) = \texttt{MinBladeCost}(\boldsymbol{p}_a, \boldsymbol{p}_s, D, \boldsymbol{\Gamma}_s) : \tag{2.35a}$$
$$(\boldsymbol{p}_{s,b}, \boldsymbol{p}_{s,t}) = \boldsymbol{p}_s, \tag{2.35b}$$
$$(\boldsymbol{p}_{s,b}^*, \boldsymbol{p}_{s,t}, CoE^*) = \texttt{MinBladeTowerCost}(\boldsymbol{p}_a, \boldsymbol{p}_{s,b}, \boldsymbol{p}_{s,t}, D, \boldsymbol{\Gamma}_s) \tag{2.35c}$$
$$\boldsymbol{p}_s^* = \boldsymbol{p}_{s,b}^* \cup \boldsymbol{p}_{s,t}. \tag{2.35d}$$

The structural optimization function (2.34g) is subjected to several constraint functions (2.34h) - (2.34m). The optimization loop iterates for a set number of solidities and maximum chords until the field of solution is satisfactorily explored. The minimum CoE* and the related values of σ^* and c_{max}^* are identified by a response surface method applied by the function (2.34o). The inputs of `minCoE` are the vectors $\boldsymbol{CoE}$, $\boldsymbol{\sigma}$, $\boldsymbol{c}_{max}$,

in which the i-values of the blade population given by the for-loop are stacked, while the outputs are the optimal values for these parameters. The optimal aero-structural configuration is obtained by the sequential application of the functions `MaxAEP` and `MinBladeCost`, sampling the blade population in correspondence to $\sigma = \sigma^*$ and $c_{max} = c^*_{max}$, as shown by Eq. (2.34p) – (2.34q).

Under the assumption that the family of aerodynamic shapes is representative of the field of solutions, this method offers the capability of catching the global trend of CoE and it is fast and robust. Unfortunately, this method heavily relies on the analyst's skills. The blade designer must indeed be able to forecast the main drivers among the several aerodynamic parameters. The identification of the CoE global minimum crucially depends on the selection of these parameters and their couplings. Finally, to this day the process is not fully automated and requires the manual creation of the family of blades and the subsequent running of the structural optimization loops. In conclusion, the PAAS approach just described can be considered a very useful initial tool to describe the field of solutions. The rapidity and robustness of this approach allow a rough initial description of the field of solutions and this aero-structural optimization tool can act as a very useful benchmark for the other approaches described in Sects. 2.4.3 and 2.4.4. However, following the common trend of reducing the responsibilities and the working time of the human operator, the need for more accurate and automatized methods is evident.

2.4.3 External Aerodynamic/Internal Structure approach

To effectively tackle the challenge of obtaining a true aero-structural optimization, a new approach was developed. This approach, hereby referred by the acronym EAIS, somehow resembles the conceptual algorithm discussed for the PAAS approach described in Sect. 2.4.2, but it also includes some crucial differences. Mainly, the choice of the aerodynamic parameters $\boldsymbol{p}_a$ is not left in the hands of an experienced blade designer, but it is now automatically handled by an external optimization routine. This aerodynamic optimization loop has in its cost function the sequence of blade mass minimization, AEP computation and finally CoE evaluation. In this algorithm, the CoE becomes the effective merit figure to be minimized and this heavily influences the behavior of the optimization process. The approach is shown by the block diagram reported in Fig. 2.9, the external aerodynamic and the internal structural optimization loops are clearly visible.

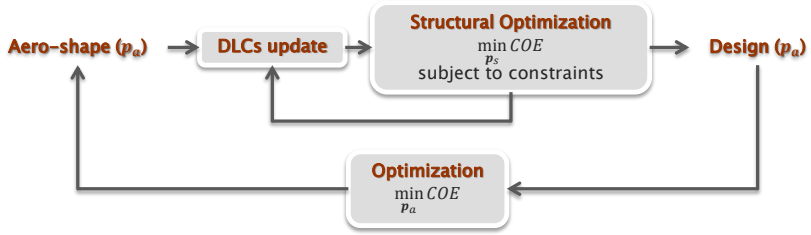

Figure 2.9: *Block diagram of the EAIS optimization*

The structure of the algorithm is described in the equations (2.36a) - (2.36p) using

the same formalism already found in the previous sections:

$$\textbf{Function } (\boldsymbol{p}^*_{a,c}, \boldsymbol{p}^*_{a,t}, \boldsymbol{p}^*_s, CoE^*) = \texttt{EAISOptimization}(\boldsymbol{p}_a, \boldsymbol{p}_s, D, \boldsymbol{\Gamma}_s) : \tag{2.36a}$$
$$(\boldsymbol{p}_s, CoE) = \texttt{MinBladeCost}(\boldsymbol{p}_a, \boldsymbol{p}_s, D, \Gamma_s), \tag{2.36b}$$
$$\text{s.t.:} \quad \boldsymbol{g}_s(\boldsymbol{p}_s) \leq \boldsymbol{0}, \tag{2.36c}$$
$$\boldsymbol{\omega}(\boldsymbol{p}_s, D) \in [\boldsymbol{\omega}_L, \boldsymbol{\omega}_U], \tag{2.36d}$$
$$\boldsymbol{\sigma}(\boldsymbol{p}_s, \boldsymbol{E}, D) \leq \boldsymbol{\sigma}_{\text{adm}}, \tag{2.36e}$$
$$\boldsymbol{\epsilon}(\boldsymbol{p}_s, \boldsymbol{E}, D) \leq \boldsymbol{\epsilon}_{\text{adm}}, \tag{2.36f}$$
$$\boldsymbol{d}(\boldsymbol{p}_s, \boldsymbol{E}, D) \leq \boldsymbol{1}, \tag{2.36g}$$
$$\boldsymbol{\delta}_{\text{tip}_{\text{max}}}(\boldsymbol{p}_s, \boldsymbol{E}, D) \leq \boldsymbol{\delta}_{\text{tip}_{\text{adm}}}. \tag{2.36h}$$
$$(\boldsymbol{p}_{a,c}, \boldsymbol{p}_{a,t}) = \boldsymbol{p}_a, \tag{2.36i}$$
$$\textbf{do} \tag{2.36j}$$
$$(\boldsymbol{p}^*_{a,c}) = \texttt{ChordGuess}(\boldsymbol{p}_{a,c}, CoE), \tag{2.36k}$$
$$\text{s.t.:} \quad \boldsymbol{g}_a(\boldsymbol{p}_{a,c}) \leq \boldsymbol{0}. \tag{2.36l}$$
$$(\boldsymbol{p}^*_{a,t}, \boldsymbol{p}^*_s, CoE^*) = \texttt{EAISCostFunction}(\boldsymbol{p}^*_{a,c}, \boldsymbol{p}_{a,t}, \boldsymbol{p}_s, D, \Gamma_s), \tag{2.36m}$$
$$\Delta p_{a,c} = \left\| \boldsymbol{p}^*_{a,c} - \boldsymbol{p}_{a,c} \right\|, \quad \Delta CoE = \|CoE^* - CoE\| \tag{2.36n}$$
$$\boldsymbol{p}_{a,c} = \boldsymbol{p}^*_{a,c}, \quad CoE = CoE^*, \tag{2.36o}$$
$$\textbf{while } (\Delta p_{a,c} \geq \text{tol}_{p_{a,c}} \textbf{ and } \Delta CoE \geq \text{tol}_{CoE}). \tag{2.36p}$$

The optimization process starts with a first evaluation of the CoE expressed by equation (2.36b), by means of a structural optimization for the given initial aerodynamic parameters $\boldsymbol{p}_a$. Then, chord and twist optimization variables $\boldsymbol{p}_{a,c}$ and $\boldsymbol{p}_{a,t}$ are differentiated, see equation (2.36i), to be handled separately. This is necessary because of the very small sensitivity of the CoE in respect to the twist distribution. Therefore, it is decided that the external aerodynamic optimization loop only manages $\boldsymbol{p}_{a,c}$. The true optimization loop enclosed between (2.36j) and (2.36p) first includes the optimization algorithm here represented by function `ChordGuess` in equation (2.36k). This optimization algorithm is currently be run thanks to the function `patternsearch` of the `Matlab` Global Optimization Toolbox [61]. `patternsearch` offers a robust tool for the nonlinear constrained optimization process without requiring continuity and differentiability of cost functions. This is an important feature that allows to explore the solution space relaxing the continuity and linearity assumptions assumed in the problem. `ChordGuess` handles $\boldsymbol{p}_{a,c}$ based on the CoE output produced by the cost function `EAISCostFunction` represented in equation (2.36m) and further elaborated in the list of equations (2.37). The variations imposed to $\boldsymbol{p}_{a,c}$ are again constrained by a set of

nonlinear constraints as indicated by (2.36l).

$$\textbf{Function } (\boldsymbol{p}^*_{a,t}, \boldsymbol{p}^*_s, CoE^*) = \texttt{EAISCostFunction}(\boldsymbol{p}^*_{a,c}, \boldsymbol{p}_{a,t}, \boldsymbol{p}_s, D, \Gamma_s) : \tag{2.37a}$$
$$(\boldsymbol{p}^*_{a,t}) = \texttt{TwistOptMaxCp}(\boldsymbol{p}^*_{a,c}, \boldsymbol{p}_{a,t}, \boldsymbol{p}_s, D), \tag{2.37b}$$
$$\text{s.t.:} \quad \boldsymbol{g}_a(\boldsymbol{p}_{a,t}) \leq \boldsymbol{0}. \tag{2.37c}$$
$$\boldsymbol{p}^*_a = \boldsymbol{p}^*_{a,c} \cup \boldsymbol{p}^*_{a,t}, \tag{2.37d}$$
$$(\boldsymbol{p}^*_s, CoE^*) = \texttt{MinBladeCost}(\boldsymbol{p}^*_a, \boldsymbol{p}_s, D, \Gamma_s), \tag{2.37e}$$
$$\text{s.t.:} \quad \boldsymbol{g}_s(\boldsymbol{p}_s) \leq \boldsymbol{0}, \tag{2.37f}$$
$$\boldsymbol{\omega}(\boldsymbol{p}_s, D) \in [\boldsymbol{\omega}_L, \boldsymbol{\omega}_U], \tag{2.37g}$$
$$\boldsymbol{\sigma}(\boldsymbol{p}_s, \boldsymbol{E}, D) \leq \boldsymbol{\sigma}_{\text{adm}}, \tag{2.37h}$$
$$\boldsymbol{\epsilon}(\boldsymbol{p}_s, \boldsymbol{E}, D) \leq \boldsymbol{\epsilon}_{\text{adm}}, \tag{2.37i}$$
$$\boldsymbol{d}(\boldsymbol{p}_s, \boldsymbol{E}, D) \leq \boldsymbol{1}, \tag{2.37j}$$
$$\boldsymbol{\delta}_{\text{tip}_{\text{max}}}(\boldsymbol{p}_s, \boldsymbol{E}, D) \leq \boldsymbol{\delta}_{\text{tip}_{\text{adm}}}. \tag{2.37k}$$

As anticipated previously, in the EAIS optimization approach the design of the twist distribution becomes a nested and isolated problem that runs before the aeroelastic simulations and the structural optimization loop. This is described by the function `TwistOptMaxCp` in equation (2.37b), where an optimization process is run for the twist optimization to achieve the highest C_p in region II for the current wind turbine configuration described by $\boldsymbol{p}^*_{a,c}$, $\boldsymbol{p}_{a,t}$, $\boldsymbol{p}_s$ and D. The twist optimization is again constrained by the set of nonlinear constraints $\boldsymbol{g}_a$ expressed in equation (2.37c). For each distribution of chord and twist corresponding to $\boldsymbol{p}^*_{a,c}$ and $\boldsymbol{p}^*_{a,t}$ a structural optimization is then run to minimize blade mass, to compute the AEP and finally to evaluate the current value for the merit figure CoE^*, see equation (2.37e). The function `MinBladeCost`, already discussed in (2.35), is subjected to the common set of structural constraints.

Compared to the PAAS approach, the EAIS optimization tool offers a fully automated procedure that can explore the space of solutions more effectively and more accurately. Moreover, it does not rely on any a priori choice of the aerodynamic parameters $\boldsymbol{p}_a$ and the optimization algorithm can impose variations to the chord based on the downstream variations of the CoE. The main drawback of this tool compared to the PAAS approach is the higher computational cost.

2.4.4 Monolithic with Load Updating approach

The MLU approach merges aerodynamic and structural design of rotor blades in a single optimization problem. Differently from the previous PAAS and EAIS approaches, in this method the structural $\boldsymbol{p}_s$ and the aerodynamic $\boldsymbol{p}_a$ parameters are handled together by the same optimization routine. Conceptually, the suggested approach is therefore an extension of what reported in Sect. 2.3, where the structural optimization algorithm (2.14) is developed. However, a key difference exists between this approach and the structural optimization method: when the aerodynamic configuration is modified, the loads variations are no longer negligible and a technique to estimate loads dependence on aerodynamic variables must be developed. The block diagram of the monolithic procedure is reported in Fig. 2.10, where the aero-structural optimization is represented by

a single block. This block includes the monolithic design procedure with the updating of the load envelope. The reference value of the load envelope is obtained by aeroservoelastic `Cp-Lambda` analyses in the "DLCs update" block. An iterative approach corrects the reference load envelope, leading to a convergent method if the loads updating procedure provides a good approximation of the DCL evaluation.

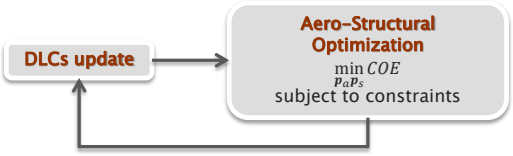

Figure 2.10: *Block diagram of the MLU optimization*

The algorithmic form of the optimization procedure is listed by Eq. (2.38):

$$\textbf{Function } (\boldsymbol{p}_a^*, \boldsymbol{p}_s^*, CoE^*) = \texttt{MLUOptimization}(\boldsymbol{p}_a, \boldsymbol{p}_s, D, \boldsymbol{\Gamma}_s) : \tag{2.38a}$$
$$(\boldsymbol{E}) = \texttt{LoadEnvelope}(\boldsymbol{p}_a, \boldsymbol{p}_s, D), \tag{2.38b}$$
$$\textbf{do} \tag{2.38c}$$
$$(\boldsymbol{p}_{s1}, \boldsymbol{p}_{s2}) = \boldsymbol{p}_s, \tag{2.38d}$$
$$(\boldsymbol{p}_a^*, \boldsymbol{p}_{s1}^*, CoE^*) = \texttt{MinCostMLUApproach}(\boldsymbol{p}_a, \boldsymbol{p}_{s1}, D, \boldsymbol{E}, \boldsymbol{\Gamma}_s), \tag{2.38e}$$
$$(M) = \texttt{3DCADAndFEMeshGeneration}(\boldsymbol{p}_a^*, \boldsymbol{p}_{s1}^* \cup \boldsymbol{p}_{s2}, \boldsymbol{E}), \tag{2.38f}$$
$$(\boldsymbol{p}_{s2}^*, w_2^*, \Gamma_s') = \texttt{3DFEAnalysis}(M, \boldsymbol{p}_{s2}, D, \boldsymbol{E}, \boldsymbol{\Gamma}_s), \tag{2.38g}$$
$$\boldsymbol{p}_s^* = \boldsymbol{p}_{s1}^* \cup \boldsymbol{p}_{s2}^*, \tag{2.38h}$$
$$(\boldsymbol{E}') = \texttt{LoadEnvelope}(\boldsymbol{p}_a^*, \boldsymbol{p}_s^*, D), \tag{2.38i}$$
$$\Delta p_a = \left\|\boldsymbol{p}_a^* - \boldsymbol{p}_a\right\|, \quad \Delta p_{s1} = \left\|\boldsymbol{p}_{s1}^* - \boldsymbol{p}_{s1}\right\|, \quad \Delta CoE = \|CoE^* - CoE\|, \tag{2.38j}$$
$$\boldsymbol{p}_a = \boldsymbol{p}_a^*, \quad \boldsymbol{p}_s = \boldsymbol{p}_s^*, \quad \boldsymbol{\Gamma}_s = \boldsymbol{\Gamma}_s', \tag{2.38k}$$
$$\textbf{while } (\Delta p_a \geq \text{tol}_{p_a} \textbf{ and } \Delta p_{s1} \geq \text{tol}_{p_{s1}} \textbf{ and } \Delta CoE \geq \text{tol}_{CoE}). \tag{2.38l}$$

In algorithm (2.38) the aerodynamic variables $\boldsymbol{p}_a$ are part of the optimization procedure as the structural variables $\boldsymbol{p}_s$. In vector $\boldsymbol{p}_a$ the shape functions $\boldsymbol{p}_{a,c}$ and $\boldsymbol{p}_{a,t}$ that modify the chord and twist distribution respectively are included, while $\boldsymbol{p}_s$ is the vector containing the structural thicknesses. The outputs of the function are the optimal values concerning aerodynamics $\boldsymbol{p}_a^*$, structure $\boldsymbol{p}_s^*$ and minimum cost of energy CoE^*. Also in this case a multi-level approach is applied, including 3D FEM refinement, but for sake of simplicity the attention is focused on coarse-level optimization of the function

(2.38e) reported in algorithm (2.39):

$$\textbf{Function } (\boldsymbol{p}_a^*, \boldsymbol{p}_s^*, CoE^*) = \texttt{MinCostMLUApproach}(\boldsymbol{p}_a, \boldsymbol{p}_s, D, \boldsymbol{E}_0, \boldsymbol{\Gamma}_s): \tag{2.39a}$$

$$(\boldsymbol{p}_a^*, \boldsymbol{p}_s^*) = \min_{\boldsymbol{p}_a, \boldsymbol{p}_s} CoE(\boldsymbol{p}_a, \boldsymbol{p}_s, D) \quad (\text{and } CoE^* = \arg\min_{\boldsymbol{p}_a, \boldsymbol{p}_s} CoE), \tag{2.39b}$$

$$\text{s.t.:} \quad \boldsymbol{g}_a(\boldsymbol{p}_a) \leq \boldsymbol{0}, \tag{2.39c}$$

$$\boldsymbol{g}_s(\boldsymbol{p}_s) \leq \boldsymbol{0}, \tag{2.39d}$$

$$\boldsymbol{\omega}(\boldsymbol{p}_s, D) \in [\boldsymbol{\omega}_L, \boldsymbol{\omega}_U], \tag{2.39e}$$

$$\boldsymbol{\sigma}(\boldsymbol{p}_s, \boldsymbol{E}, D) \leq \boldsymbol{\sigma}_{\text{adm}}, \tag{2.39f}$$

$$\boldsymbol{\epsilon}(\boldsymbol{p}_s, \boldsymbol{E}, D) \leq \boldsymbol{\epsilon}_{\text{adm}}, \tag{2.39g}$$

$$\boldsymbol{d}(\boldsymbol{p}_s, \boldsymbol{E}, D) \leq \boldsymbol{1}, \tag{2.39h}$$

$$\boldsymbol{\delta}_{\text{tip}_{\max}}(\boldsymbol{p}_s, \boldsymbol{E}, D) \leq \boldsymbol{\delta}_{\text{tip}_{\text{adm}}}. \tag{2.39i}$$

$$\text{where} \quad (\boldsymbol{p}_{a,t}^*) = \texttt{TwistOptMaxCp}(\boldsymbol{p}_{a,c}^*, \boldsymbol{p}_{a,t}, \boldsymbol{p}_s, D) \tag{2.39j}$$

$$\boldsymbol{p}_a = \boldsymbol{p}_{a,c} \cup \boldsymbol{p}_{a,t}^* \tag{2.39k}$$

$$(\boldsymbol{E}) = \texttt{UpdatingLoadEnvelope}(\boldsymbol{p}_a, \boldsymbol{E}_0) \tag{2.39l}$$

As for the algorithm in (2.14), the large number of design requirements, expressed by constraint equations, suggests to apply a gradient based optimization strategy to the function `MinCostMLUApproach`. Since the analysis environment is complex and it implies the interaction of multiple software, the only feasible way to estimate gradients is by finite differences. The merit figure of `MinCostMLUApproach` is the CoE, while the set of constraints is the union between constraint equations of algorithms (2.1) and (2.16). The meaning of the design requirements is reported in Sects. 2.2 and 2.3 and it is not repeated here. The function `TwistOptMaxCp` links twist variables $\boldsymbol{p}_{a,t}$ to chord variables $\boldsymbol{p}_{a,c}$ as reported in Sect. 2.4.3.

The core of the `MLUOptimization` is expressed by equation (2.39l), which represents the procedure for updating the load envelope. The goal of equation (2.39l) is to estimate the load variations as a consequence of perturbations of $\boldsymbol{p}_a$. Approximate models are built to rapidly estimate the values of constraint equations and their sensitivity to the optimization variables, while avoiding the re-computation of all the DLC. At the beginning of each optimization cycle, the correct values of the loads envelope is known from `Cp-Lambda` analyses, so the exact constraints values are available. These measurements are then updated by considering the variations of vector $\boldsymbol{p}_a$. The inputs of function `UpdatingLoadEnvelope` are the current aerodynamic parameters $\boldsymbol{p}_a$ and the load envelope $\boldsymbol{E}_0$, computed in a high fidelity simulation environment, while the output is the corrected load envelope $\boldsymbol{E}$.

Different scaling procedures are applied for the different constraints, taking into account the physics involved in each design requirement. Ultimate load constraints and blade-tower clearance evaluation are considered at first: these requirements are enforced by the instantaneous internal load distributions extracted from the set of DLC and collected into a load envelope. Aerodynamic, inertial and gravity loads are included into the internal forces evaluated by `Cp-Lambda`. The assumption that only aerodynamic loads are affected by variations of aerodynamic variables $\boldsymbol{p}_a$ is applied. This hypothesis is suggested by the aerodynamic BEM theory, which indicates that the

distributed aerodynamic loads are linear function of the blade chord. This assumption implies approximations, i.e. a modified chord causes a variation of the inflow angle and therefore of the angle of attack, but it is here assumed that the variations of inflow angle can be neglected because of limited modification of the solidity of the rotor. Other approximations are related to small perturbations of rotor azimuthal position and control inputs that can be considered only if the evaluation of the DLC is repeated. Nevertheless, a correct load envelope evaluation by `Cp-Lambda` analyses would lead to a discontinuous behavior if the ranking of the load is modified as reported in Sect. 2.3. So the selection of the most severe DLC is updated by the external iteration and the load envelope is scaled during the gradient evaluation procedure, removing the source of discontinuities from the SQP algorithm. Considering aerodynamic distributed forces $\boldsymbol{F}_a$ and moments $\boldsymbol{M}_a$ in the local aerodynamic reference frame, the scaling process by chord multiplicative gains $\boldsymbol{p}_{a,c}$ is:

$$\boldsymbol{F}_a = \boldsymbol{F}_a + \Delta\boldsymbol{F}_{\boldsymbol{a}} = \boldsymbol{F}_a + \Delta\boldsymbol{p}_{\boldsymbol{a,c}}\,\boldsymbol{F}_{a,0}$$
$$\boldsymbol{M}_a = \boldsymbol{M}_a + \Delta\boldsymbol{M}_{\boldsymbol{a}} = \boldsymbol{M}_a + \Delta\boldsymbol{p}_{\boldsymbol{a,c}}\,\boldsymbol{M}_{a,0}.$$

where subscript $_0$ identifies the `Cp-Lambda` measurements pertinent to the reference model, while Δ is the variation from reference value. Applying linear beam theory to updated aerodynamic loads $\boldsymbol{F}_{\boldsymbol{a}}$ and $\boldsymbol{M}_{\boldsymbol{a}}$, the corrections of internal forces distributions are obtained. Ultimate loads scaling procedure is shown in Fig. 2.11, where local variation of aerodynamic distributed loads is reported considering a local increase of the blade chord.

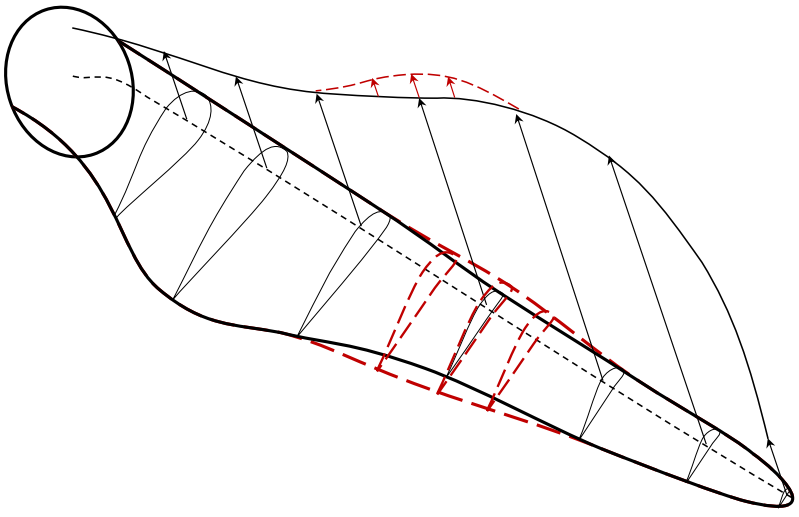

Figure 2.11: *Ultimate loads updating procedure: scaling of aerodynamic distributed loads*

A different approach is instead required to estimate sensitivity of damage fatigue index to aerodynamic parameters. The fatigue damage depends indeed on time histories of load conditions that explore all machine operative region, so it takes into account the global effects of aerodynamic variables on the overall dynamic behavior of the wind

turbine. The estimation of the damage index constraint cannot therefore be separated from the evaluation of the dynamic response of the machine. However, the computational costs must be kept low due to the numerous evaluations of the cost function `MinCostMLUApproach`. The way to overcome this is found by means of a simplified model that is integrated into the SQP optimization loop. A possible approach to increase the computational efficiency of the model could be the application of a reduction technique, where elastic elements are approximated by an efficient base. Various techniques of model reduction are available and some examples can be found in [73]. The authors choose a different approach that deals with the global nature of the fatigue constraint and does not require simulation software modifications. Various tests have proved a correct estimation of fatigue damage sensitivity to aerodynamics parameters when simplified wind turbine multibody models are considered. The applied hypothesis is that fatigue fluctuations are mainly due to aerodynamic loads and accelerations applied to the blade, while the interactions between the blades and the effect of the tower are considered negligible. So it is possible to estimate the fatigue constraints sensitivity using a simplified multibody model, that is obtained by decreasing the number of finite elements on each blade and approximating the tower flexibility by two prismatic joints with the associated stiffness. The simplified model allows the estimation of DLC at each evaluation of the fatigue constraints and the approximation of the fatigue damage index in a limited time. Since the trend is evaluated correctly by the reduced model, the value of fatigue damage index is obtained as follow:

$$\boldsymbol{d} = \boldsymbol{d}_0 + \Delta\boldsymbol{d}_{SM} = \boldsymbol{d}_0 + (\boldsymbol{d}_{SM} - \boldsymbol{d}_{SM,0})$$

where subscript $_{SM}$ identifies the quantities estimated by the simplified model.

The whole procedure of load update is therefore based on physical simplified models and it is necessary to estimate the constraints sensitivities during the optimization process. Since the results of the inner optimization algorithm are based on these approximations, a recalibration procedure is worthiness to fill the gap with the higher-fidelity model. For this reason a tuning enforced by `Cp-Lambda` full model is performed at each macro cycle of `MinCostMLUApproach` to verify the real values of the constraints and to reduce the estimation error. The trade-off between higher-fidelity and lower-fidelity models is achieved by bounds on optimization variables and tolerances provided by the user. The bounds on variables allow to limit the changes of the aero-structural configuration during the inner optimization loop based on lower-fidelity models, while the tolerance of the inner optimization algorithm limits the drift from the reference configuration before loads recalibration. A good trade-off avoids over-solving the inner optimization problem and exploits the lower-fidelity models potentialities. This approach has proved fair robustness and leads to an iterative procedure that usually converges after few steps to a stationary point. The comparison of the results produced by the different aero-structural approaches proves the validity of the procedure for the load update.

2.5 Refinement of Structural Configuration

The structural refinement can be applied if robust procedures to generate automatically a reliable finite element model are provided. For a complex structure such as a wind

turbine blade this requires several steps, which can be summarized as:

- Definition of the modeling approach that will drive the overall procedure, as reported in Sect. 2.5.1.
- Parametric definition of each blade component, either in terms of its bounding surfaces or of the laminate mid-planes, as described in Sect. 2.5.2.
- Generation of a complete FE model, described in Sect. 2.5.3, which in turn requires:
  - Mesh generation of the 3D blade discretization using shell elements or solid elements, as described in Sect. 2.5.3.
  - Assignment of element properties, including the laminate ply stacking sequences and associated thicknesses, material parameters and fiber orientations, as detailed in Sect. 2.5.3.
  - Conversion of the 1D spatial beam model loading conditions into equivalent conditions for the 3D FE model, as described in Sect. 2.5.3.
- FE analysis and post-processing of the results for the verification of the relevant design conditions, as detailed in Sect. 2.5.4.

In this work, the CAD model generation, as well as the assignment of the associated material properties and loading conditions, is based on the information from the coarse-level optimizer, and it is performed in `Matlab`. The FE mesh generation is performed using the batch meshing facilities of `HyperMesh`, where the required scripts are generated in `Matlab`. Finally, `Matlab` scripts handle the batch submission of the various analyses performed using `MSC Nastran` [74], as well as their post-processing.

2.5.1 Modeling aspects

The way in which the FE modeling of wind turbine blades is conducted may have a significant influence on the procedures used for generating the CAD geometry. The most frequently used technique for blade modeling is based on layered shell elements [12, 22], which are commonly available in commercial FE solvers. Most implementations provide the possibility of specifying the extent of the elements in terms of offsets from a reference surface other than its mid-thickness. This is particularly convenient when dealing with wind turbine blades, as the elements can be specified with respect to the exterior surface defined by the shape of the airfoils. Since the external shape is smooth, the generation of the necessary CAD model is not particularly complicated.

However, a possible drawback of the offset technique is that it may result in the erroneous prediction of the torsional behavior of the blade [75]. This problem is of particular concern since torsion affects loading through changes in the angle of attack, as for example explicitly exploited for load mitigation in bend-twist coupled rotor blades [49]. Recent improved shell formulations circumvent this problem, as for example element `SHELL281` [76] or the pre-integrated matrix input [77] available for `ANSYS`.

Otherwise, one can generate a mid-thickness CAD model of the blade, as done manually in [78]. The construction of the geometry using mid-thickness surfaces, illustrated in Fig. 2.12a at left, is in general rather cumbersome, since thickness variations lead to step changes between contiguous mid-thickness surfaces.

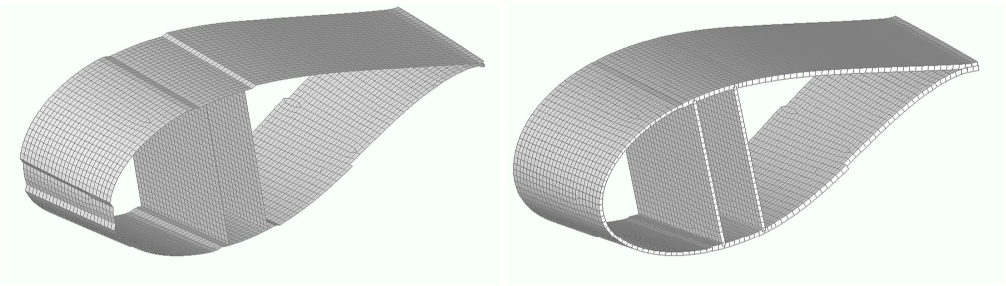

(a) *Mid-thickness shell elements* **(b)** *Solid elements*

Figure 2.12: *Two possible FEM models of rotor blades*

Alternatively, solid elements can be used for building the mesh, as shown in Fig. 2.12b at right. These are particular suitable for capturing inter-laminar stresses, for delamination and debonding analysis. However, the use of solid elements may complicate the CAD generation, since both the external and internal surfaces must be defined, which may be cumbersome to do in the various transition zones of a blade. Furthermore, one should pay specific attention to the accurate definition of the material property orientation [79]. While procedures for associating the correct material orientation to models composed of shell elements are rather well established (e.g. by direct projection of a user-defined material reference vector on the element [80]), the case of complex models composed of solid elements requires special attention as individual local coordinate systems must be defined.

For generality, the present implementation supports all approaches mentioned above, so that one may generate mid-thickness shells, or, alternatively, solid element meshes. However the approach involving mid-thickness shell elements generation has proved to be more robust and reliable than the generation of a model based on solid elements, so it is usually select for standard applications.

2.5.2 CAD model

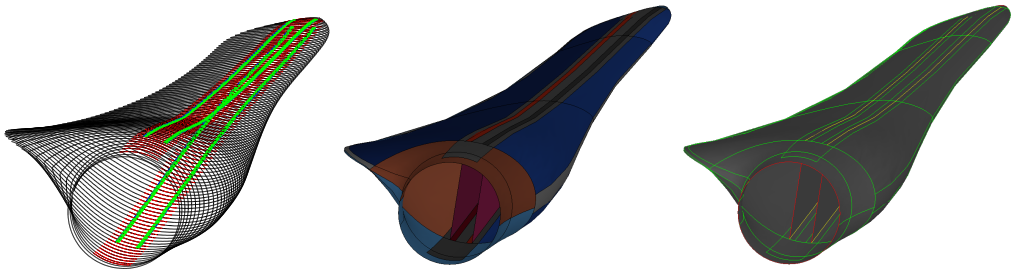

(a) *Interpolation of airfoil data points* **(b)** *NURBS surfaces* **(c)** *Partitioning in simple sub-surfaces*

Figure 2.13: *Selected steps in the generation of the CAD model of a wind turbine blade*

The generation of a complete CAD surface model for shell meshing is accomplished as follows. A number of cross sections, typically of the order of one hundred, are obtained by thickness-interpolation of the generating airfoil data points, using their span-wise chord and twist distributions. Chordwise spline interpolations are used for

parameterizing the airfoils from their data points, and nodes define the location of the boundaries of the projections of the various blade elements (spar caps, shear webs, etc.) onto the external blade surface, as illustrated in Fig. 2.13a.

For mid-thickness CAD generation, an inward projection along the local normal is performed using the thickness information associated with each blade element. This way, steps at the boundaries between elements with different thicknesses are generated. The thickness data accounts for span-wise variations, as computed by the coarse-level optimization, as well as user-defined chord-wise variations; the latter ones are used to avoid modeling errors associated with the overlapping of inner skin/core, which are likely to occur near the trailing edge [24].

From the chordwise interpolations of the airfoils or their mid-thickness projections, collocation data points are obtained with sufficient sampling resolution (typically of the order of one thousand points per cross section) to allow for an accurate surface parameterization, which is obtained by using NURBS [81] on each surface describing a blade component projection.

Some details are here reported to better understand the generation of the NURBS surfaces. For sake of simplicity a curve is considered at first, then the attention is focused on the surfaces. A $p-$degree Non-Uniform Rational B-Spline (NURBS) curve is defined by

$$C(u) = \frac{\sum_{i=0}^{m} N_{i,p}(u) w_i P_i}{\sum_{i=0}^{m} N_{i,p}(u) w_i} \quad a \leq u \leq b$$

where P_i are the control points, the w_i are the weights and the $N_{i,p}(u)$ are the pth-degree B-spline basis functions defined on the parameter u and on knot vector U:

$$U = \{\underbrace{0, \ldots, 0}_{p+1}, u_{p+1}, \ldots, u_{r-p-1}, \underbrace{1, \ldots, 1}_{p+1}\}$$

where $r = m + p + 1$.

Control points position and weight modifications can be exploited to control the local shape of the curve. Each control point P_i influences the curve by its position and by the associated weight w_i. The knot vector U divides the parametric space into knot spans, defining how the control points influence the curve.

The definition of a NURBS surface can be easily obtained by the extension of the curve definition. A NURBS surface of degree p in the u direction and degree q in the v direction is the following bivariate vector-valued piecewise rational function:

$$S(u, v) = \frac{\sum_{i=0}^{m} \sum_{j=0}^{n} N_{i,p}(u) N_{j,q}(v) w_{i,j} P_{i,j}}{\sum_{i=0}^{m} \sum_{j=0}^{n} N_{i,p}(u) N_{j,q}(v) w_{i,j}} \quad 0 \leq u, v \leq 1$$

where $P_{i,j}$ are the control points, $w_{i,j}$ are the weights, $N_{i,p}(u)$ and $N_{j,q}(v)$ are nonrational

B-spline basis functions defined on knot vectors:

$$U = \{\underbrace{0, \ldots, 0}_{p+1}, u_{p+1}, \ldots, u_{r-p-1}, \underbrace{1, \ldots, 1}_{p+1}\}$$
$$V = \{\underbrace{0, \ldots, 0}_{q+1}, v_{p+1}, \ldots, v_{s-q-1}, \underbrace{1, \ldots, 1}_{q+1}\}$$

with $r = m + p + 1$ and $s = n + q + 1$.

Assuming unitary weights, the interpolating surface of degree (p, q) that contains all the points $D_{c,d}$ is:

$$D_{c,d} = S\left(s_c, t_d\right) = \sum_{i=0}^{m} \sum_{j=0}^{n} N_{i,p}\left(s_c\right) N_{j,q}\left(t_d\right) P_{i,j} \tag{2.42}$$

Fixing the degree, the interpolating surface is defined by the knot vector and by the control points.

The knot vector is related to s_c and t_d, that are the values of the parameters when the surface pass through each point $D_{c,d}$. The collocation parameters for the interpolation procedure are obtained using the centripetal method [82]. Considering the u direction, the values $u_{i,j}$ are obtained by:

$$\begin{cases} u_{0,j} = 0 \\ u_{k,j} = \dfrac{\sum\limits_{i=0}^{k} \left|D_{i,j} - D_{i-1,j}\right|^{\frac{1}{2}}}{\sum\limits_{i=0}^{m} \left|D_{i,j} - D_{i-1,j}\right|^{\frac{1}{2}}} \quad \text{with} \quad k = 1, \ldots, m \\ u_{m,j} = 1 \end{cases}$$

while the same procedure is applied to v direction, obtaining $v_{i,j}$. The final values of the parameters are obtained by the average

$$s_i = \frac{\left(u_{i,0} + u_{i,1} + \ldots + u_{i,n}\right)}{n+1} \quad \text{with} \quad i = 1, \ldots, m$$
$$t_j = \frac{\left(v_{0,j} + v_{1,j} + \ldots + v_{m,j}\right)}{m+1} \quad \text{with} \quad j = 1, \ldots, n$$

The knot vectors are related to the values of the parameters s_c and t_d. The first $p + 1$ knots are null, while the last $p + 1$ knots have unitary value to clamp the surface to the boundary control points. The other elements of the knot vectors are computed by using the average method suggested by de Boor [81]:

$$\begin{cases} u_0 = u_1 = \ldots = u_p = 0 \\ u_k = \dfrac{1}{p} \sum\limits_{i=j}^{j+p-1} s_i \quad \text{with} \quad j = 1, \ldots, m - p \\ u_{m-p} = u_{m-p+1} = \ldots = u_m = 1 \end{cases}$$

Considering the Eq.(2.42), the term $N_{i,p}$ is independent of the index j, so the equation can be rewritten as follow

$$D_{cd} = S\left(s_c, t_d\right) = \sum_{i=0}^{m} N_{i,p}\left(s_c\right)\left(\sum_{j=0}^{n} N_{j,q}\left(t_d\right) P_{i,j}\right) \tag{2.43}$$

$$= \sum_{i=0}^{m} N_{i,p}\left(s_c\right) Q_{i,d} \tag{2.44}$$

where $Q_{i,d}$ is defined by a change of variable. This system of linear equations allows to find the d-th column of control points $Q_{i,d}$, given the degree p in direction u, the parameters s_i and the d-th column of data points $D_{i,d}$.

So each column of control points $Q_{i,d}$ is obtained by the solution of an interpolation problem applied to each column of data points. Finally solving the system of equations that express $Q_{i,d}$, the control points $P_{i,j}$ are obtained.

$$Q_{i,d} = \sum_{j=0}^{n} N_{j,q}\left(t_d\right) P_{i,j} \tag{2.45}$$

In this case the $i-$th row of $P_{i,j}$ is the vector of control points related to $i-$th row of the matrix Q by the B-spline curve of degree q evaluated at t_d parameters. Once the position of the control points $P_{i,j}$ is computed, the B-spline surface of p, q degree, with knots vectors U and V, is fully defined. Other points on the surface are obtained by the evaluation of Eq. (2.42) considering generic value of (s, t).

For the construction of a solid mesh, the external blade surfaces are first generated as described above. Next, the various surfaces are further partitioned into simpler sub-surfaces, as illustrated in Fig. 2.13c. Partitioning is performed such that, by extruding inwards each external sub-surface along the local thickness direction, one can obtain the associated facing internal sub-surface; this will allow for the generation of the solid mesh by means of a similar through-the-thickness extrusion of a surface mesh, as explained later on. Contact areas between two surfaces, as at the glued connections between shear webs and spar caps, are also used for the partitioning, so as to ensure conforming discretizations during meshing.

The information associated with the parametric NURBS representation of the resulting model is finally exported in Initial Graphics Exchange Specification (IGES) format towards `HyperMesh` for subsequent meshing.

The present approach, which tries to generate an accurate geometric model before meshing, differs significantly from the lofting of pre-defined cross sectional meshes and presents several advantages. In fact, using this approach the shape of the internal skin as well as the transitions between zones with varying thickness along the span of the blade are precisely reconstructed. This is particularly important since these regions must be accurately modeled [51], and it may be particularly useful in areas of rapid span-wise variations as the one between root and max chord span.

2.5.3 FE model

Mesh generation

The generation of an unstructured mostly quadrilateral shell mesh is obtained by using `HyperMesh` on the exterior or mid-thickness surface CAD model; a limited number of triangular elements is generally obtained close to corners and in a few difficult spots. The meshing algorithm ensures the conformity of the resulting grid across edges bounding the various sub-surfaces of the model.

An unstructured mostly hexahedral solid mesh is obtained by first quad meshing the external sub-surface of each individual blade component as for the shell case, projecting the mesh onto the opposite internal surface, optionally defining through-the-thickness discretizations by the same projection, and finally connecting the resulting surface grids into a solid one. Since the initial surface meshes are conforming, the final solid grid is also guaranteed to be conforming.

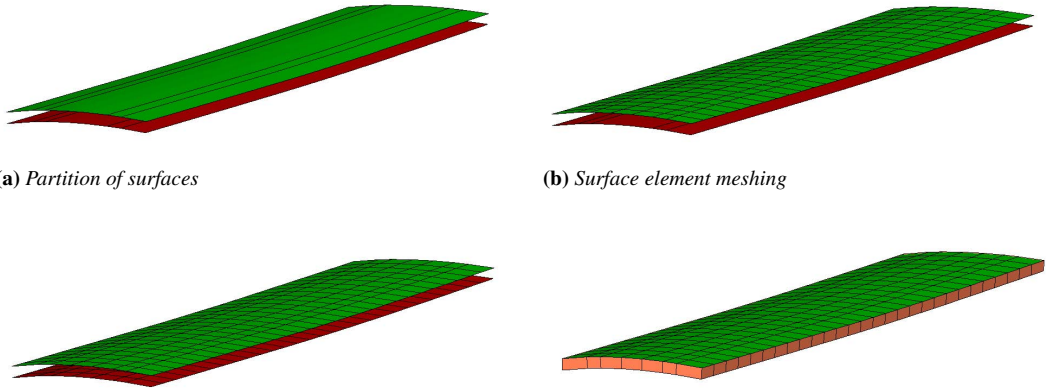

(a) *Partition of surfaces*

(b) *Surface element meshing*

(c) *Surface element projection*

(d) *Solid element extrusion*

Figure 2.14: *Solid meshing generation procedure*

The surface meshing and extrusion procedure is illustrated in Fig. 2.14 for a span-wise portion of the spar cap; notice that the external surface has been divided into several stripes in the chord-wise direction, Fig. 2.14a, to account for the glued connections with the shear webs. The creation of the shell elements on the first surface is reported by Fig. 2.14b. The projection on the other surface is visible in Fig. 2.14c and the generation of the solid elements is shown in Fig. 2.14d. A span-wise portion of the resulting complete solid mesh is illustrated in Fig. 2.15a, and details of the trailing edge with its reinforcement strip and the thickness variation of the core is shown in Fig. 2.15b.

Material properties

Material properties, including the orientation of the fibers with respect to the pitch axis, are associated with the various entities of the CAD model during its definition.

Once the mesh has been generated, the definition of the material properties of each mesh element is obtained as follows. At first, the centroid of each element is computed;

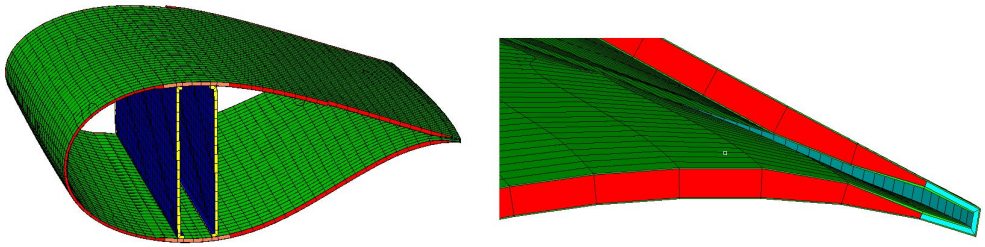

(a) (b)

Figure 2.15: *Span-wise portion of solid mesh and trailing edge detail*

if the element is of the 3D type, its centroid is projected onto the master CAD face of that blade component. At that CAD face location, a local material reference frame is defined that has a unit vector in the direction of the fibers and a second unit vector along the local normal, computed from the NURBS surface parameterization. The orthotropic material properties of the element are then readily obtained by transforming into the local reference frame of that same element.

For shell meshes, the procedures support the generation of layer-by-layer representations by Classical Lamination Theory (CLT). This approach is particular convenient for modeling very thin layers, such as the skin coating that would result in elements with very high aspect ratios. Even though such details of the blade design may seem to be of minor importance from the structural point of view, they can indeed have a significant influence on the estimation of the total mass (up to $4 \div 5\%$), with a consequent possible effect on the blade dynamic properties.

Equivalent loading conditions

In order to perform all relevant analyses on the fine-level FE model, appropriate loading and boundary conditions must be generated from the results of the coarse-level multibody simulations; these include loads inducing extreme stress and strain values, loads associated with maximum tip deflections, as well as time histories of the turbulent loads cases for the evaluation of fatigue damage. For each of these loading conditions, span-wise distributions of the internal stress resultants and of the aerodynamic forces are readily available from the multibody simulations.

The computation of equivalent loading conditions for the FE model can be performed in two ways: the internal forces can be applied directly or a distinction between aerodynamic and inertial loads can be considered.

The first approach considers a discretization of the internal forces distribution, copying the static load tests of the certification procedure of the real blade. A finite number of blade sections along the blade span is taken into account to apply the loads. The discrete loads are evaluated to best approximate the original internal forces distributions at these sections. The approximation of the internal forces and moments applied to 3D FEM are is shown in Fig. 2.16. The axial force, the shear forces and the torsional moment are obtained by dead loads applied at the discretization sections. The resulting distributions are piecewise constant functions of the blade span, as shown by Fig. 2.16a. The nondimensional blade coordinates are designated by η_i, where the index i identifies the sections where the loads are discretized. ΔF_i refers to the i-increment of the inter-

nal forces applied to the i-section on the blade axis E, that is a generic axis where the internal forces are evaluated. The magnitude of the original distribution is represented by the purple solid line, the applied loads are the blue vectors and the resulting stepwise distribution is displayed by the blue dashed line. Considering the linear beam theory, the bending moments are obtained by shear forces approximations and they are piecewise linear functions of the blade span. Looking at Fig. 2.16b, the original distribution is reported by the purple solid line while the approximated one is displayed by the blue dashed line.

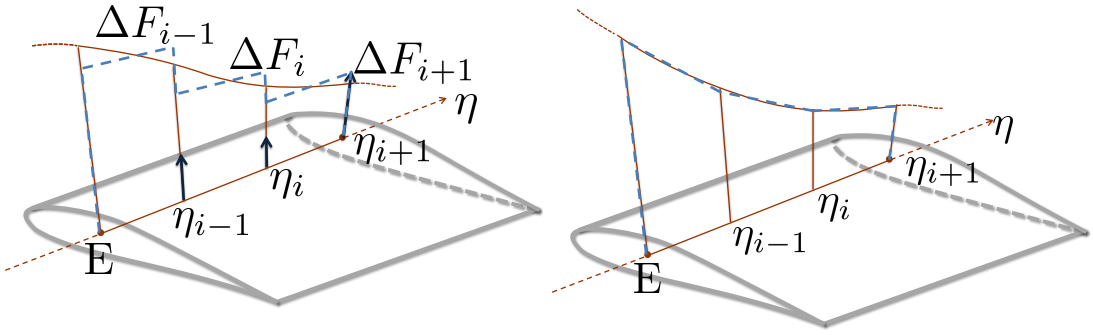

(a) *Shear discretization* **(b)** *Moment discretization*

Figure 2.16: *Discretization of internal forces*

In the second approach, a realistic loading conditions for the blade can be established, e.g. by limiting the application of the aerodynamic loads to the external skin nodes. The analytic explanation of this method is here reported while the implementation will be considered among the further developments of the blade modeler.

Span-wise distributions of inertial loads are recovered by enforcing the equilibrium of a blade portion. With reference to Fig. 2.17, consider a blade segment $\eta \in [\eta_i, \eta_{i+1}]$, where $\eta \in [0, 1]$ is the span-wise non-dimensional coordinate running along the beam reference line passing through the sectional point E. The internal stress resultants on the $(i+1)$th section is $\boldsymbol{f}_{i+1}$, and the moment resultant about E is $\boldsymbol{m}_{i+1}$, while the ones on the ith section negative face are $-\boldsymbol{f}_i$ and $-\boldsymbol{m}_i$, respectively. At the span-wise station η, per-unit-span aerodynamic forces $\boldsymbol{f}^A(\eta)$ and moments $\boldsymbol{m}^A(\eta)$ are applied at the aerodynamic reference line passing through the sectional point A, which is at a distance $\boldsymbol{r}^A(\eta)$ from point E on the ith section. Similarly, per-unit-span inertial forces $\boldsymbol{f}^I(\eta)$ and moments $\boldsymbol{m}^I(\eta)$ are applied at the beam reference line, which is at a distance $\boldsymbol{r}^I(\eta)$ from point E on the ith section.

The force and moment (about E) equilibrium conditions for the blade segment write

$$-\boldsymbol{f}_i + \boldsymbol{f}_{i+1} + \int_{\eta_i}^{\eta_{i+1}} (\boldsymbol{f}^A + \boldsymbol{f}^I)\, \mathrm{d}\eta = 0, \tag{2.46a}$$

$$-\boldsymbol{m}_i + \boldsymbol{m}_{i+1} + \int_{\eta_i}^{\eta_{i+1}} (\boldsymbol{m}^A + \boldsymbol{m}^I + \boldsymbol{r}^A \times \boldsymbol{f}^A + \boldsymbol{r}^I \times \boldsymbol{f}^I)\, \mathrm{d}\eta + \boldsymbol{r} \times \boldsymbol{f}_{i+1} = 0. \tag{2.46b}$$

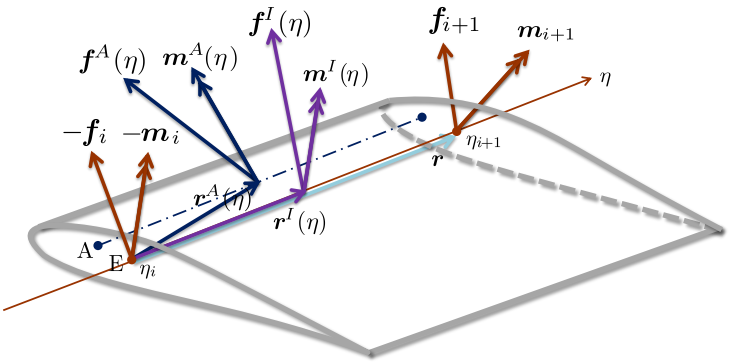

Figure 2.17: *Recovery of inertial loads from sectional internal stress resultants and aerodynamic loads*

By using a trapezoidal approximation for the span-wise integrals, one obtains

$$\int_{\eta_i}^{\eta_{i+1}} \boldsymbol{f}^I \, \mathrm{d}\eta \approx \frac{\eta_{i+1} - \eta_i}{2} (\boldsymbol{f}_i^I + \boldsymbol{f}_{i+1}^I), \tag{2.47}$$

where $\boldsymbol{f}_i^I$ and $\boldsymbol{f}_{i+1}^I$ are sectional inertial forces. By inserting (2.47) into (2.46a), starting from the blade tip, one may compute each sectional inertial force $\boldsymbol{f}_i^I$ based on the sectional resultants and aerodynamic loads. Similarly, from (2.46b) one may compute each sectional inertial moment $\boldsymbol{m}_i^I$.

Once sectional loads have been recovered as explained, they are applied to the blade structure by means of `RBE3` interpolation elements provided in the commercial FE solver `MSC Nastran` [74]. Different sets of nodes can be associated with different interpolation elements, each one in turn associated with a different set of forces and moments. This way aerodynamic loads can be applied to the sole skin nodes, while inertial loads can be applied to all sectional nodes; alternatively, combined loads can be applied to the spar cap nodes, as shown in Fig. 2.18. In all cases, forces are distributed to each node considering local user defined weighting factors, while moments are applied as sum of equilibrated forces on dependent nodes, as explained in [83]. An example of the application of loads to the spar cap of a shell 3D model is reported in Fig. 2.18.

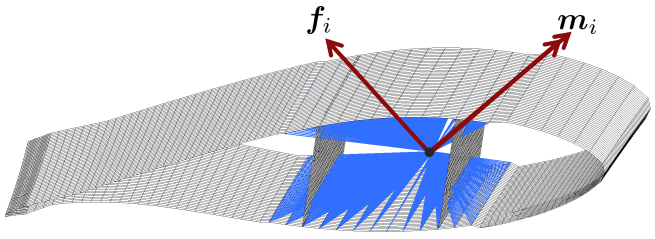

Figure 2.18: *Load application to spar caps nodes using the `RBE3` element*

A more realistic way of representing aerodynamic loads would be to reconstruct the chord-wise pressure distribution, for example using assumed shapes from experimental measurements or from suitable numerical models such as `Xfoil` [84]. This feature will be included in future releases of the code.

2.5.4 Analysis

The automatically generated 3D FE model enables the detailed fine-level verification of the various constraint inequalities associated with the overall optimization problem. Furthermore, it can be used for designing secondary structural parts such as the skin core thickness by means of a linearized buckling analysis. In the present section the assumptions and procedures for these various analyses are described.

Static analysis

Static analyses are performed for the verification of the constraint inequalities associated with the max/min allowable stresses/strains and the maximum tip deflection, with the aim of revealing possible effects not captured by the beam model.

For each user-defined verification section, the max/min stress/strain loading conditions are readily identified by scanning all DLCs of interest [14], and using the sectional recovery relations provided by `ANBA`. Next, the corresponding equivalent loading conditions are first computed as described in Sect. 2.5.3 from the coarse-level analysis, and then applied to the 3D FE model. Similarly, by scanning all DLCs, the maximum tip deflection condition is identified and translated into an equivalent loading condition.

Geometric and material linear static analyses are performed in `MSC Nastran`, and the relevant results in terms of strains, stresses and displacements are processed in `Matlab` to detect possible violations of the constraint conditions. It was verified that, for the examples developed in the present work, the use of geometrically nonlinear analyses, as opposed to the present linear ones, yield only negligible differences, although this might not be the case for the future projected very long and slender next generation wind turbine blades.

Modal analysis

During coarse optimization, a design accommodating desired dynamic properties can be obtained by specifying suitable constraints for significant natural frequencies of the blade, as described in Sect. 2.3.2. Such constraints are typically expressed for the rotating blade at rated rotor angular velocity. The inertial effects associated with blade rotation are taken into account in the `Cp-Lambda` modal analysis by first performing a nonlinear static analysis subjected to a loading condition including the inertial effects of rotational motion, and then by performing a modal analysis about the resulting deformed configuration, accounting for the centrifugal stiffness term.

A similar procedure could be used for performing the modal analysis on the 3D FE model [74]. However, while coarse-level constraints are enforced for the rotating frequencies, the fine-level verification of the frequency conditions is performed here for simplicity as a standard non-rotating modal analysis about the blade undeformed configuration. In particular, ratios between corresponding non-rotating frequencies, computed on the coarse-level beam and fine-level FE models, are used as indicators of the disagreement between the two representations. This is a reasonable assumption, since both models are sophisticated enough to precisely account for inertia-related changes of frequencies, and thus the ratios between non-rotating frequencies are expected to change in a similar fashion. Furthermore, rotational effects on frequencies are typically rather limited for wind turbine rotor blades.

Fatigue analysis

Similarly to the coarse-level optimization procedure [14], the fine-level evaluation of damage caused by loads in turbulent wind conditions (DLC 1.2 [50]) is only conducted for a limited set of critical points at user-defined verification sections. Such critical points are identified during coarse optimization as the sectional spots where the multiaxial damage index d of Eq. (2.18) exceeds a specified threshold.

The stress time histories necessary for evaluating the damage index are conveniently computed by exploiting the linear superposition of static unit load cases applied to the FE model with load histories obtained from the beam model (see e.g. [85]). At each verification point, a static force or moment (in the case of shells) of unit magnitude is applied, and the full stress time history follows as

$$\sigma_i(t) = \sum_j P_j(t) \frac{\sigma_{i,j}}{P_{j,\mathrm{FEA}}}, \tag{2.48}$$

where $P_j(t)$ denotes a load history obtained by a multibody transient simulation, $P_{j,\mathrm{FEA}}$ the applied unit load, and σ_i is the static stress resultant at point i for load case j. Each time step of the loads history $P_j(t)$ could be discretized by using one of the approaches reported in Sect. 2.5.3, for sake of simplicity, the direct discretization of the internal forces is chosen. This choice allows to consider all the dynamic contributions included into internal forces that are provided by the multibody software. Even if the stresses σ_i are obtained by static analysis, the effects of inertial loads and time variant aerodynamic effects are considered because they are naturally included into internal forces evaluation. So this procedure reduces the computational cost necessary for the evaluation of the full stress time history on the comprehensive 3D FE model. The remaining steps required for the computation of the damage index follow the same procedure used at the coarse analysis level, using rain-flow counting and the associated Markov matrices.

Buckling analysis

An additional feature only provided by a full 3D FE model is the capability of performing a linearized buckling analysis, which can be used for designing secondary structural elements, such as the skin and web core thicknesses. It is important to include the sizing of secondary components in the design process, because the distribution of the associated structural material has a significant influence on the non-structural mass, which in turn affects the dynamic behavior of the blade by changing its mass distribution.

Prior to the FE analysis, an initial distribution of the core material and thickness for skin and webs can be estimated by the following two step procedure, based on simplified design formulas:

1. Choice of material. Appropriate stiffness properties for the core material are estimated such that local buckling (or wrinkling) is avoided, as this may cause fractures in the core or delamination. Following [86], this is accomplished by comparing the computed extreme compressive stress to the following critical stress:

$$\sigma_{\mathrm{adm,wrinkling}} = 0.5 \sqrt[3]{G_{\mathrm{core}}\, E_{\mathrm{core}}\, E_{\mathrm{skin}}}, \tag{2.49}$$

   where G and E denote the shear and Young's moduli, respectively.

2. Thickness sizing. For the skin and web panels, the critical buckling stress $\sigma_{\text{adm,buck}}$ and shear $\tau_{\text{adm,buck}}$ are computed using the following equations:

$$\sigma_{\text{adm,buck}} = \frac{\pi^2}{t_{\text{panel}} b^2} K_{\text{c}} \sqrt{D_{11} D_{22}}, \tag{2.50a}$$

$$\tau_{\text{adm,buck}} = \frac{\pi^2}{t_{\text{panel}} b^2} K_{\text{s}} \sqrt[4]{D_{11} D_{22}^3}, \tag{2.50b}$$

where t_{panel} is the skin or web panel thickness, b is the panel edge width, D_{11} and D_{22} are the diagonal components of the out-of-plane bending stiffness matrix of the sandwich panels computed with classical laminate theory. Finally, K_{c} and K_{s} are buckling factors accounting for several properties of a sandwich structure, like its orthotrophy, curvature and out-of-plane shear flexibility, as well as for the way the longitudinal stress is distributed along the plate edge. For further details about the computation of the buckling factors see [65].

At several stations along the blade span, the skin core is sized by imposing the constraint $\lambda_s \geq 1$, where λ_s is the skin buckling load factor, computed by solving the following equation:

$$\lambda_s \left(\frac{\sigma}{\sigma_{\text{adm,buck}}} \right) + \lambda_s^2 \left(\frac{\tau}{\tau_{\text{adm,buck}}} \right)^2 = 1, \tag{2.51}$$

which takes into account stress-shear interactions [87]. Similarly, the web core is sized constraining $\lambda_w \geq 1$, where λ_w is the solution of:

$$\lambda_w^2 \left(\left(\frac{\sigma}{\sigma_{\text{adm,buck}}} \right)^2 + \left(\frac{\tau}{\tau_{\text{adm,buck}}} \right)^2 \right) = 1. \tag{2.52}$$

Subsequently in the design process, at the fine verification level and similarly to the case of the primary structural variables described in Sect. 2.3.2, the core thickness of a region where buckling occurs is increased by an amount proportional to the exceedance of the constraint condition $\lambda \leq 1$, where λ is the buckling eigenvalue associated with the applied load.

In the present implementation, the linear buckling analysis is performed using the loading conditions that result from the load envelope and the maximum tip deflection of the blade. These situations are characterized by severe compressive loads on the blade external shell and strong shear loading on shear webs panels, identifying the most critical conditions prone to buckling.

2.6 Local Structural Modeling

Local analyses might be required to provide a reliable structural sizing of the critical regions, enhancing the resolution of 3D FEM of the complete blade. Usually a region that requires a detailed analysis is the blade root bolted joint, where the bolts are embedded into blade laminate to provide the connection with the pitch bearing. Other critical areas are the trailing edge of the blade and shear webs edges. In these regions, the stress and strain distributions can be correctly estimated by taking into account the presence of adhesive that can be modeled accurately by a local 3D FEM.

Increasing the analysis resolution is possible by fully three dimensional detailed finite element analyses. These investigations are computationally expensive, so they can be applied only to blade sections with limited extension. Considering the importance of the blade root region, the capability of performing local analysis of blade root bolted joint is developed. The attention is focused on this detail because it influences the laminate thickness considerably, affecting the overall blade mass and the global blade configuration as well. The other local features affect the global blade design partially, so they will be considered in the near future.

2.6.1 Detailed modeling of blade root region

A local analysis of the blade root bolted joint can be performed as shown in Fig. 2.3, completing the information provided by the 3D FEM of the entire blade. A classical T-Bolt configuration is here reported, but the approach can be extended to different solutions, for example a threaded insert can be considered with minor code modifications concerning the CAD model. Generating a local detailed model requires a procedure similar to the creation the 3D FEM of the entire blade. However, some fundamental differences can be identified so a brief description is reported below. Also in this case the meshing platform `Altair Hypermesh` is exploited by `Tcl` scripting language [88], while `Matlab` manages all the data flows from the definition of the inputs to the generation of the final model.

Modeling aspects

The local analyses are performed by fully three dimensional models, identifying the 3D effects that are not visible in the global blade model. Zooming on the blade root, the effects on the blade laminate due to the holes of the bolts and to the bolts themselves are shown. It is also possible to examine the three dimensional stress field that affects the bolts due to the preloading and the application of the external forces.

A fully three dimensional analysis implies the generation of a solid geometry and the domain discretization by solid finite elements, resulting in a remarkable rise of the dimensions of the model. For this reason, the cyclic symmetry of the blade root region is exploited to limit the involved number of degrees of freedom.

The next sections show the generation of the CAD model and FE model. Finally the analyses are reported, showing the procedure applied to the bolt sizing and laminate verification of the blade root region.

CAD model

A model parametrization speeds up the design, easing the updating procedure and the reanalysis capability. Arbitrary dimensions of the pitch bearing, blade root laminate, bolts and barrel nuts can be considered by the current parametrization. Also a generic bolting configuration can be taken into account, allowing to explore the effects of the bolts number and their relative position.

For sake of simplicity a configuration with two T-bolts of different length is now examined, while various layouts can be easily inferred. The modeled region is shown in Fig. 2.19, where the entire blade root region is reported on the left, while a zoom on the bolted joint is displayed on the right. The heads of the bolts are identified by the

gray circles, the barrel nuts are shown by the dashed cylinders and the axes of the bolts are represented by the dash-dotted lines. Notice that the bolts have different length: a short bolt alternates a longer one. This configuration reduces the stress on laminate due to the holes of the barrel nuts. Exploiting cyclic symmetry, the modeled area is delimited by the blue solid on the right side of Fig. 2.19. It spans an angle that includes the halves of two consecutive bolts and it considers a portion of blade root laminate long enough in the span direction to remove the local effects due to external load application.

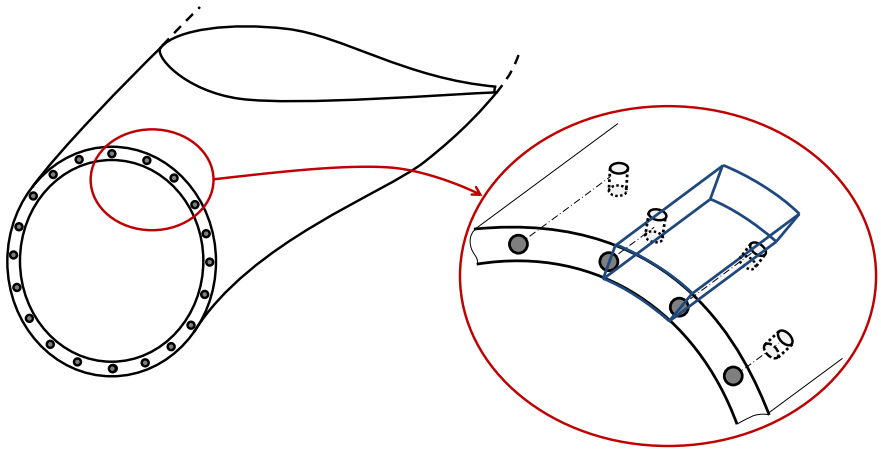

Figure 2.19: *Sketch of the blade root and detailed modeled region*

Each solid component of the CAD model is generated by the surfaces that define the external shape. Each surface is created by the procedure reported in Sect. 2.5.2 or by native functions of the `Altair Hypermesh` environment. The surfaces are assembled to form the solids that represent topological elements of the model, i.e. bolts, barrel nuts, pitch bearing and blade laminates. Each solid complies with the neighboring ones, allowing the generation of a consistent mesh.

An example of the parametric CAD model is reported in Fig. 2.20, showing a model sketch with quote and an exploded assembly where different components are identified.

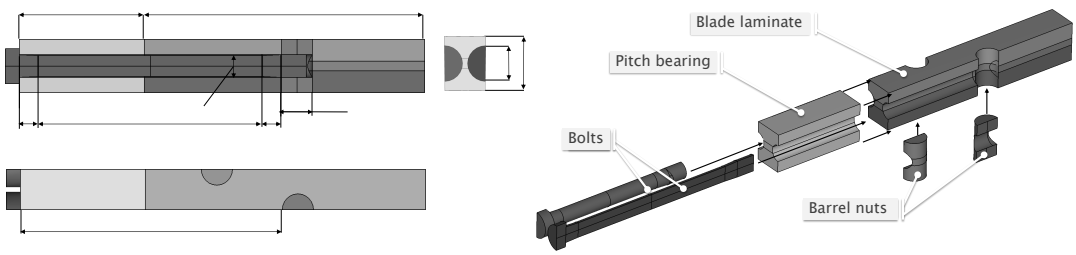

(a) *Model sketch standard views*

(b) *Three dimensional exploded assembly*

Figure 2.20: *Parameteric blade root geometry*

FE model

A `MD-MSC Nastran` FE model is created by meshing the CAD geometry by `Altair Hypermesh` facilities. The detailed FE model employs solid tetrahedral elements, allowing a robust meshing approach and ensuring, if required, the connection of the finite elements between different structural components. Anisotropic material laws define the mechanical properties of the orthotropic laminates, while the steel pitch bearing is defined by standard isotropic material. Constraint equations impose preload on bolts and contact between different components [74], [89]. Since only a sector of the blade root is analyzed, suitable symmetry conditions are imposed on the boundaries. Furthermore the model is constrained along axial direction where the pitch bearing reaction is supposed to be applied.

An example of FE model is reported in Fig. 2.21. All the structural components are highlighted by different colors, constraint elements and contact surfaces are also shown. The external load is applied by an interpolation element. This choice does not affect the results since the local effects are limited to the region close to interpolation element.

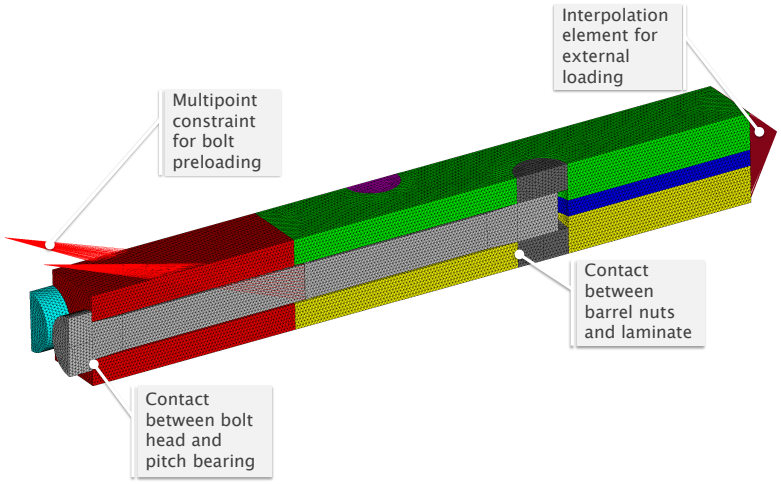

Figure 2.21: *Blade root detailed FEM*

It is supposed that the external load is oriented in the parallel direction to the bolts axis. The load application point is on the mean thickness line of the laminate and it is equidistant from the symmetry surfaces of the model. Given the axial forces F_{axial} and resulting bending moment $M_{bending}$ applied to the blade root, the axial load carried by each bolt is obtained as:

$$F_i = \frac{M_{bending}}{\sum_{i=1}^{N_{bolts}} A_i d_i^2} d_i A_i + F_{axial} \tag{2.53}$$

where A_i is the nominal area of each bolt and d_i is the distance of each bolt to the line of application of $M_{bending}$. Considering the extension of the modeled region, the load applied to the model F_A is obtained by a combination of the F_i values. Depending on the analysis performed, different values of F_{axial} and $M_{bending}$ are taken into account to perform structural design as reported in the next section.

Analyses

The contact between the pitch bearing and the blade must be ensured during the entire operative range, so a preload must be imposed to each bolt to avoid separation during the ultimate load conditions. The most critical situation is identified by the maximum value of the bending moment at blade root. The external load applied to the FE model can be directly obtained from the load envelope at this blade section applying the Eq. 2.53. The preload P on each bolt is evaluated by the approach suggested by [90], completing the data provided by the standard with the one obtained by the FE analysis:

$$P = \alpha_A \, LTF \, P_{min} = \alpha_A \, LTF \left[\left(1 - \sum_{i=1}^{N_{Mod}} \phi_i \right) F_A \, (1 + R_F) \right] \tag{2.54}$$

where:

- α_A is the tightening factor, due to the inaccuracy of the tightening methods
- LTF is the load transfer factor, due to the loss of preload related to threads deflection and radial expansion of the nuts
- R_F is the relaxation factor, it considers the effects of temperature, deformation of the contact surface and relaxation of the material
- ϕ_i is the fraction of the applied load carried by the bolt. The summation spans over the N_{Mod} modeled bolts and it allows to determine the preload for the more flexible bolt.

The preloads of the other bolts are computed by P to ensure the same tension during the ultimate load condition. The factors ϕ_i are obtained by the FE analysis, evaluating the ratio between the load carried by each bolt and the external applied load. Considering the complexity of the structural configuration, characterized by orthotropic material and different bolts, only a FE model can provide the reliable estimation of fraction ϕ_i.

After the definition of the preloads values, the verification of bolted joint is performed considering ultimate load and fatigue damage as suggested by international standards [51], [69] and [90]. The ultimate stress on each bolt $\sigma_{Bolt,i}$ is evaluated considering the ultimate load cases as follow:

$$\sigma_{Bolt,i} = \frac{P_i + \phi_i F_A}{A_i} \tag{2.55}$$

allowing the evaluation of the safety margin $s_{Bolt,U}$ for the ultimate stress condition:

$$s_{Bolt,U} = \min_i \frac{\sigma_{yield,i}}{\gamma_{M,static} \sigma_{Bolt,i}} \tag{2.56}$$

The fatigue analysis is performed by life equivalent load that is evaluated by life equivalent bending moment $M_{bending,eq}$ at the blade root.

$$M_{bending,eq} = \left[\sum_{i=1}^{N_{Wind}} \left(\frac{\sum_{j=1}^{N_{Cycle}} n_j M_j^m}{N_{eq}} \right)_i N_i \right]^{\frac{1}{m}} \tag{2.57}$$

where

- N_{Wind} is the number of DLC considered to estimate fatigue life
- n_j is the number of cycles given by the application of the rainflow counting algorithm to each time history. M_j is the amplitude of the alternate bending moment related to n_j, while N_{Cycle} is the number of intervals in which the amplitude fluctuations are discretized.
- N_{eq} is the number of equivalent cycles
- N_i is a factor that scales the simulated time to the real wind turbine operative life
- m is the inverse of the Wöhler diagram slope.

The alternate stress σ_{Bolt,A_i} applied on each bolt is obtained by the Eq. (2.53) and Eq. (2.55), setting to zero value the axial force and the preload. The mean stress value σ_{Bolt,M_i} is directly obtained by the preload pertaining each bolt.

The alternate stress admissible $\tilde{\sigma}_{Adm,A}$ depends on the material detail category defined by [51] and the Wöhler diagrams reported in [69]. Safety coefficients are applied to $\tilde{\sigma}_{Adm,A}$ in agreement with [51], obtaining:

$$\sigma_{Adm,A} = \frac{k_s \tilde{\sigma}_{Adm,A}}{\gamma_{M,fatigue}} \tag{2.58}$$

where k_s is a safety factor applied to the material and $\gamma_{M,fatigue}$ is a coefficient related to the bolt nominal diameter. The mean stress admissible is the ultimate stress σ_U of the bolt material. Applying the Goodman's correction due to the mean stress, the fatigue safety margin is obtained by the following equation:

$$s_{Bolt,F} = \min_i \frac{1}{\frac{\sigma_{Bolt,M_i}}{\sigma_U} + \frac{\sigma_{Bolt,A_i}}{\sigma_{Adm,A}}} \tag{2.59}$$

The ultimate stress analysis and the fatigue life analysis provide a preliminary verification of the blade root bolted joint. If some constraints are not satisfied, a new model is created, manually modifying the input data to meet the requirements. The automatic procedures allow to update the FE model quickly, obtaining a fast evaluation of the new values of the preloads and the safety margins. Usually after few iterations, it is possible to identify a feasible configuration of the blade root bolted joint.

Notice that the design of the blade root laminate is strictly related to the bolted joint sizing. The thickness of the orthotropic material influences the external load fraction ϕ_i carried by each bolt, therefore the safety factors of the bolts. Furthermore, the FE model allows to measure the local increment of the stress in the blade root laminate due to the holes of the bolted joint. These local effects can be directly included at coarse aeroelastic layer, updating the constraints as performed by full blade 3D FEM and completing the information of the 3D FEM of the full blade. The updating procedure of the constraint equations has been reported in Sect. 2.3.6, while a graphical representation has been shown in Fig. 2.3.

2.7 Summary notes

A detailed description of each optimization method has been provided in the previous sections. It is useful to summarize the main characteristics of each method to ease the comprehension of the provided results. Recalling the structure of the chapter, the attention is focused initially on the coarse optimization level. The following itemization repeats the main features of each design procedure, highlighting the pros and cons.

- **Aerodynamic optimization**:
  - **Merit figure**: AEP
  - **Optimization variables**: Blade chord and twist span-wise distributions
  - **Pros**: Fast aerodynamic design
  - **Cons**: Structural effects are neglected
- **Structural optimization**:
  - **Merit figure**: CoE
  - **Optimization variables**: Thickness of blade structural components, chord-wise shear webs position and spar caps extension, thickness and diameter of steel tubular tower
  - **Pros**: Coupled structural design of rotor blades and support tower
  - **Cons**: Aerodynamic effects are discarded
- **Aero-structural optimization**:
  - **Merit figure**: CoE
  - **Optimization variables**: Blade span-wise chord and twist distribution and thickness of blade structural components. Other structural variables can be easily included.
  - **Pre-Assumed Aerodynamic Shape (PAAS) method**
    - **Pros**: Simple and robust approach
    - **Cons**: User's participation is required to define an effective aerodynamic parametrization
  - **External Aerodynamic/Internal Structure (EAIS) method**
    - **Pros**: Robust and fully automatic approach
    - **Cons**: High computational cost
  - **Monolithic with Load Updating (MLU) method**
    - **Pros**: Automatic approach with limited computational effort
    - **Cons**: Load scaling procedure to update design requirements could be vulnerable

The fine-level can be addressed as a verification tool that allows to perform a detailed analysis of the structural layout through 3D-FEM of the entire blade or limited critical region. Despite this tool is combined only with structural optimization in the reported case studies, it can analyze a generic configuration, that can be provided by the aero-structural optimization or by an existing layout. The capabilities of the fine-level are:

- **Refinement of structural configuration (3D-FEM)**:
  - **Modeled region**: Entire blade
  - **Modeling approach**: Shell or solid elements
  - **Analysis capability:** Ultimate stress, ultimate strain, minimum clearance, fatigue, buckling
- **Local structural modeling (local 3D-FEM)**:
  - **Modeled region**: Blade root bolted joint
  - **Modeling approach**: Solid elements
  - **Analysis capability:** Ultimate stress, fatigue

The applications and the results of the design procedures are reported below. The most significant results are selected to provide a global overview of the methods without considering ancillary information. Each application is characterized by a high generality, reproducing realistic case studies that can be encountered in a real design process.

CHAPTER 3

Applications and Results

The developed optimization techniques are extensively validated in the current chapter. Two wind turbines are considered as test cases. The first configuration is a 2MW HAWT and it represents a standard industrial configuration. This test case shows how the developed techniques can be included in a standard industrial work flow, helping the structural analyst during the design phase. The second case is a conceptual 10MW HAWT and it aims at showing how the methods can be helpful in a preliminary sizing of a wind turbine with a remarkable nominal power. Realistic situations are reproduced by both cases, always seeking a high level of completeness.

At the beginning the attention is focused on the structural optimization methods applied to the rotor blades. Section 3.1 and 3.2 minimize the blade mass, keeping constant the aerodynamic data and the other parameters that define the wind turbine configuration. Each section is focused on different aspects of structural design. The first one considers the interaction between coarse and fine optimization level, giving various details about the closure of the optimization loop. The second section concerns the effects of the nonstructural mass on the design and it includes the sizing of structural details by local 3D FEM.

The results provided by the structural algorithms are considered as reference conditions to apply the optimization techniques that involve the sizing of further parameters in addition to blade structure. This step-by-step approach allows to test the new optimization procedures, providing feasible initial guess and limiting the issues due to unfeasible initial solutions.

The sizing of the tower is coupled to the blade structural design by Sect. 3.3. The differences between a standard industrial approach and the coupled developed techniques are highlighted by the 2MW HAWT configuration. The tower design for a wind turbine with high rated power is shown by the 10MW HAWT test case. Both cases report also

trend studies that identify the optimal solution in term of wind turbine configuration.

The performance of the aero-structural optimization techniques on 10MW HAWT are studied in Sect. 3.4. The aerodynamic optimization variables merge with the structural ones gradually, considering various algorithms that ensure different coupling level between structure and aerodynamics. Multiple results are reported, highlighting the pros and cons of each algorithm in terms of required user's expertise and computational effort.

3.1 Blade Structural Design: 2MW test case

In this section the performances of the developed structural multi-level optimization procedures are clarified with respect to a standard 2MW HAWT. The wind turbine configuration is defined in Sect. 3.1.1, reporting the main details about blade configuration. Then a first comparison between coarse and fine-level is carried out in Sect. 3.1.2, pointing out the differences between the two modeling techniques. Finally the closure of the optimization loop is reported in Sect. 3.1.3, filling the gap between coarse and fine modeling level.

3.1.1 Baseline wind turbine

A standard 2MW HAWT is considered. Since a classical configuration is examined, only few data are reported in Tab. 3.1.

Table 3.1: *2MW HAWT Main Data*

Data	Value
Wind Regime	IEC Class IIIA
Rated Power	2 MW
Blades number	3
Cut in wind speed	3m/s
Cut out wind speed	25m/s
Rotor Diameter	90m
Tower Height	79m

The structural layout of the blade is a stressed-shell configuration with single upper and lower spar caps confined within two planar shear webs, normal to the maximum chord line. The primary structural design parameters $\boldsymbol{p}_{s1}$ are defined as the common thickness of the two shear webs, the common thickness of the upper and lower spar caps and the thickness of the external blade shell. These quantities are represented by span-wise linear interpolations of corresponding nodal unknowns located at η =0, 0.01, 0.03, 0.10, 0.195, 0.20, 0.25, 0.4, 0.5, 0.6, 0.75, 0.8, 0.98 and 1, resulting in a total number of primary structural design parameters equal to 53. A typical blade section is reported in Fig.3.1.

The main blade structural components are reported in Table 3.2. The blade is made of six different material types, whose mechanical properties are summarized in Table 3.3. Non-structural masses are accounted for with both span-wise and chord-wise proportional quantities. A first estimate of the secondary design parameters, represented by the skin core thickness, is obtained using the preliminary design formulas

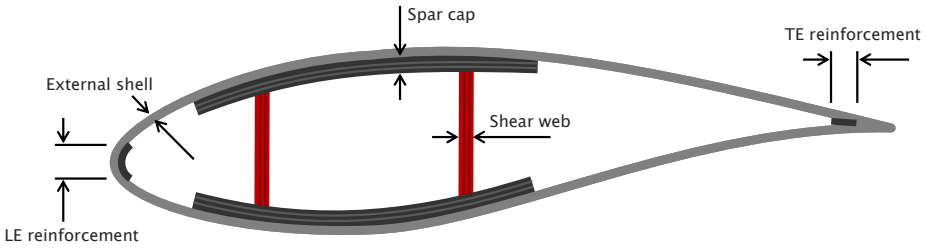

Figure 3.1: *Primary structural design parameters on a typical section*

described in Sect. 2.5.4.

Table 3.2: *2MW HAWT Structural configuration*

Component	Starting section (% span)	Ending section (% span)	Material type
External shell	0	100	Stitched triaxial -45/0/+45 fiberglass
Spar caps	3	97.8	Unidirectional fiberglass
Shear webs	10	97.8	Stitched biaxial -45/+45 fiberglass
Trailing and leading edge reinforcements	10	80	Unidirectional fiberglass
Skin core	10	97.8	T500 Foam
Web core	10	97.8	T400 Foam

The coarse minimum weight structural sizing is based on DLCs 1.2, 1.4, 1.5, 1.6, 1.7, 2.2, 2.3 and 6.1 [50]. The design constraints include: placement of the first and second blade natural frequencies with at least 12% and 20% gaps respectively with respect to the three-per-rev harmonic, a maximum blade tip deflection of $\delta_{\text{tip}_{\text{adm}}} = 5$ m, max/min allowable stresses/strains and fatigue constraints (see Eq. (2.16)).

The active constraints (A) and inactive constraints (N) are reported in Tab.3.4. The frequency placement and max tip deflection constraints are active at convergence, and thus the design is driven by the blade flap bending stiffness. In addition, fatigue constraints are active in the external shell between 10% and 40% span, where the largest chords occur. The constraints associated with stresses/strains are far from their respective limits.

Two different 3D models are generated using either mid-thickness shell elements or solid elements. For the shell model, the blade is discretized by isoparametric linear triangular and quadrilateral elements with layered composite properties. The solid model is based on isoparametric linear prismatic and hexahedral solid elements. For both models, the characteristic element side lengths are about 5 cm. All loads are applied to the spar caps using `RBE3` elements.

At first, possible differences between the coarse-level model and the detailed 3D models are investigated by performing modal, static, fatigue and buckling analyses.

Table 3.3: *2MW HAWT Material properties*

Material type	Longitudinal Young's modulus [MPa]	Transversal Young's modulus [MPa]	Shear modulus [MPa]
Stitched triaxial -45/0/+45 fiberglass	28500	10300	6400
Unidirectional fiberglass	38200	8600	3500
Stitched biaxial -45/+45 fiberglass	9700	9700	10900
T500 foam	93	93	40
T400 foam	65	65	28

Table 3.4: *2MW HAWT Baseline structural constraints*

Model	Stress/ Strain	Modal Prop.	Clearance	Fatigue
Baseline	N	A	A	A { external shell from 10% to 40% span

Next, bounds are updated for the constraints that fail verification, and the effects of loop closure on a subsequent coarse-level iteration are illustrated.

3.1.2 First multi-level iteration

Modal analysis

Table 3.5 reports the first flap-wise and edge-wise blade natural frequencies obtained with the 3D mid-thickness shell, 3D solid and beam `Cp-Lambda/ANBA` models. The associated vibration modes are visualized in Fig. 3.2.

Table 3.5: *Comparison of the two lowest blade natural frequencies*

	Shell	Solid	`Cp-Lambda/ANBA`
$\omega_{1,\text{flap}}$ [Hz]	0.855	0.853	0.857
$\omega_{1,\text{edge}}$ [Hz]	1.012	1.008	1.056

It is noted that the first flap-wise natural frequency agrees well for all models. On the other hand, the matching is not as good for the edge-wise mode, since the frequency predicted by the beam model is about 4% higher than the 3D ones. In the coarse-level optimization, this frequency is constrained to have a 20% margin with respect to the three-per-rev harmonic, and the constraint is active at convergence. To account for this, the constraint bound for this frequency is increased by 4% for the next coarse-level design iteration.

Static analysis

A static analysis for the load case corresponding to the maximum blade deflection is conducted next. A comparison of the flap- and edge-wise blade deflections obtained with the beam and 3D FE models reveals that all agree very well within a 0.02% margin.

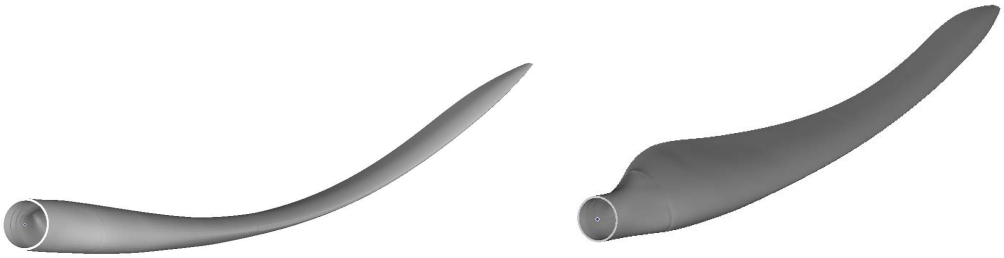

(a) *First flap-wise vibration mode* **(b)** *First edge-wise vibration mode*

Figure 3.2: *The two lowest blade vibration modes*

On the other hand, as expected, the stress distribution shows much larger differences. Figure 3.3a and 3.3b plot the span-wise distribution of maximum stresses in the fiber direction of external shell and spar caps, respectively.

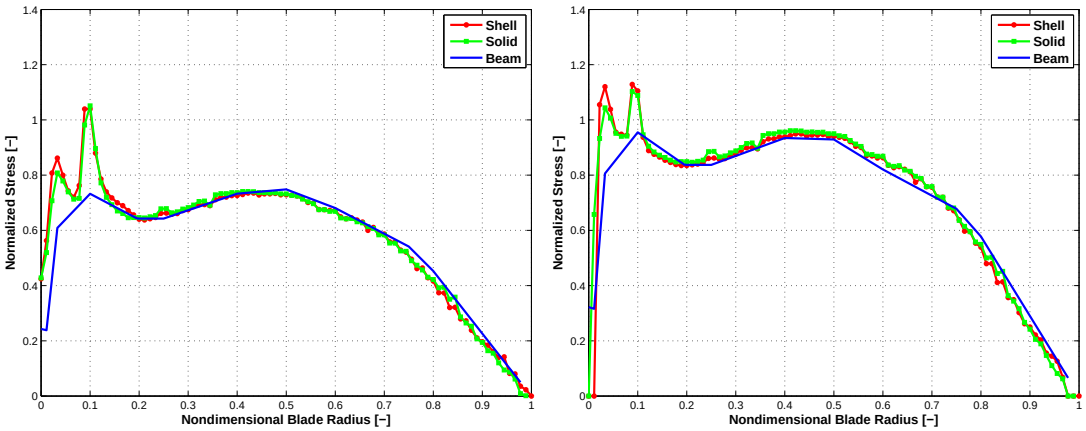

(a) *Maximum stress in external shell* **(b)** *Maximum stress in spar caps*

Figure 3.3: *Normalized maximum stresses in span-wise direction*

Figure 3.4 shows the distribution of the longitudinal stress at 10% of blade span in the external shell, plotted as a function of the non dimensional coordinate $0 \leq s \leq 1$. The importance of 3D effects in this blade region is particularly clear if one looks at the shell and solid models stress distributions and compares them to the beam one.

Significant relative differences are apparent at the root region, and in particular at the beginning of webs, leading and trailing edge reinforcements. The cause for these discrepancies is due to the simultaneous presence of rapid transitions in the local geometry and a low skin thickness. The latter exhibits a rapid variation in the first 10% span, becoming only $1/20$ of the root thickness. The figures show that peaks arise exactly at the boundary region of the spar caps and the transition of the skin core, a complex region illustrated in Fig. 3.5.

In summary, the investigation of static loading conditions clearly illustrates the need for a detailed 3D FE analysis in order to obtain reliable estimates of the stress field over the whole blade. While a beam model in general provides reasonable results for most of the blade span, it is however unable to describe the detailed stress field at critical

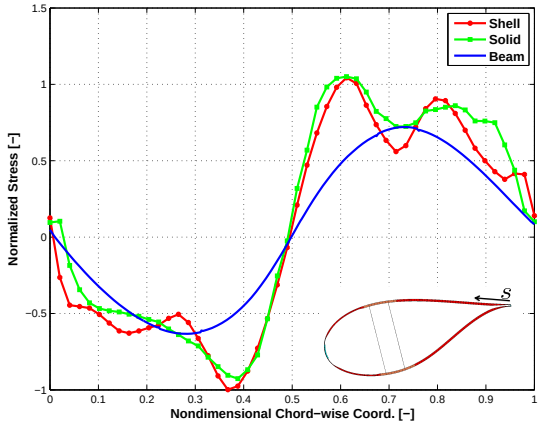

Figure 3.4: *Normalized stress in the external shell at nondimensional blade radius equal to 0.10, vs. nondimensional chord-wise coordinate s*

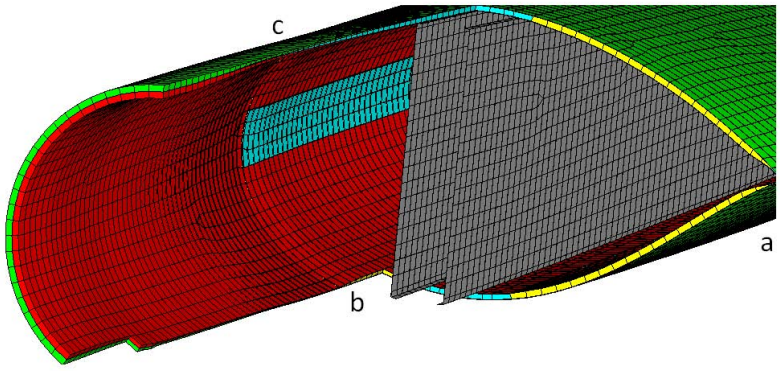

Figure 3.5: *Detail of the blade root: a) trailing edge transition, b) beginning of skin core, c) beginning of spar caps*

three dimensional and rapidly varying regions.

Fatigue analysis

A fatigue analysis as described in Sect. 2.5.4 is performed using the mid-thickness shell model. Results for the fatigue damage index evaluated according to the multi-axial criterion of Eq. (2.18) at selected span-wise sections are illustrated in Fig. 3.6a, along with comparable results obtained on the beam model.

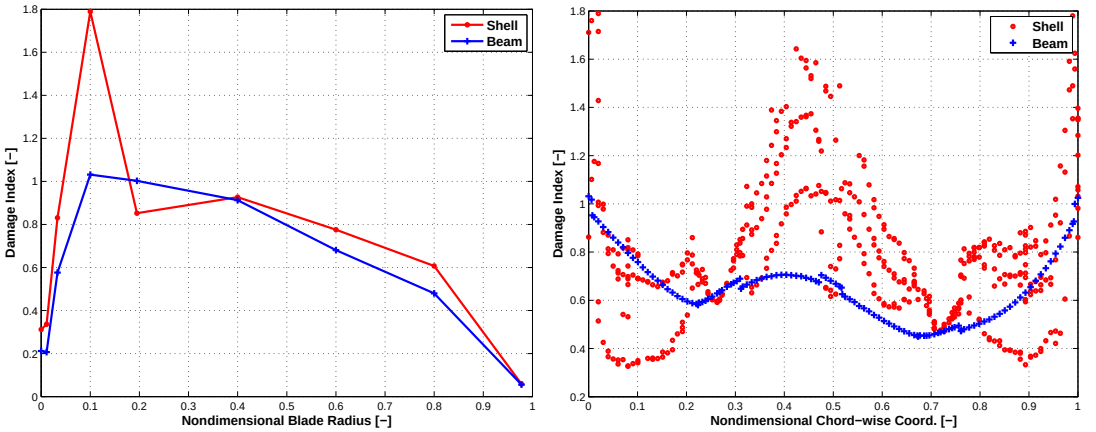

(a) *Damage index vs. blade span*

(b) *Damage index at $\eta = 0.10$ span section, vs. curvilinear coordinate s*

Figure 3.6: *Damage index in external shell at selected sections along blade span*

It appears that the detailed 3D mid-thickness shell model predicts a significant peak at 10% span, violating the fatigue constraint. Similarly to the static analysis case, the peak is grossly underestimated by the coarse-level beam model.

Figure 3.6b plots the fatigue damage parameter in the external shell at the most critical region, within a margin of 100 mm around 10% span. Fatigue damage is computed at points distributed along the airfoil, and plotted as a function of the curvilinear coordinate s. Similarly to the span-wise results, the 3D FE model predicts higher damage coefficients than the beam model, while both indicate the trailing edge region ($s = 0$ and $s = 1$) of the blade as the most exposed to fatigue.

Linear buckling analysis

Finally, a linearized buckling analysis of the 3D FE model is conducted by subjecting the blade to the loading condition of maximum tip displacement.

The first two buckling modes are shown in Fig. 3.7a and 3.7b. The first mode is localized near the blade root, while the second at the maximum chord region. Only the first mode is critical for the applied loading condition ($\lambda \leq 1$), and the instability is caused by the high compressive stresses that are generated around 10% span.

To correct for this, the structural capacity at this region would need to be increased. This can be done by using procedure (2.23), which would increase the skin core thickness. However, it should be noted that the same region of the blade failed the verification of the fatigue constraints. The update of the associated constraint bounds will induce, at the next coarse-level optimization, a modification of the primary structural

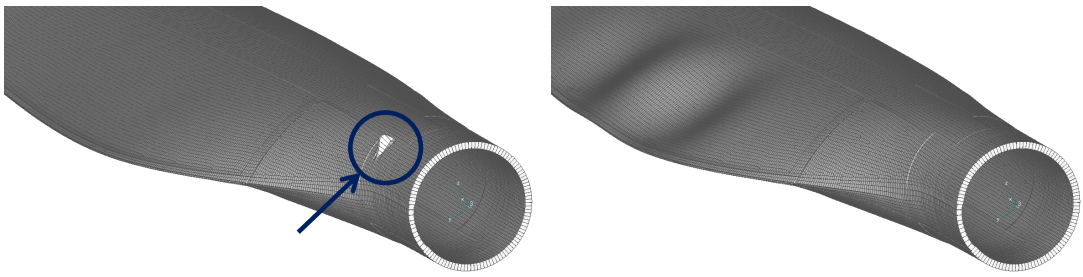

(a) *First buckling mode,* $\lambda_{Shell} = \lambda_{Solid} = 0.8$ **(b)** *Second buckling mode,* $\lambda_{Shell} = 3.594$, $\lambda_{Solid} = 3.4078$

Figure 3.7: *Close-up view of first two buckling modes*

parameters that will also induce a local strengthening of the structure. As a side effect, this might results in a sufficient buckling resistance for the original core thickness. In light of this observation, it was decided to avoid the update of the secondary design parameters, and wait for the result of the next coarse design iteration.

3.1.3 Closure of multi-level optimization loop

The closure of the loop between the coarse-fine analyses and back is illustrated by performing a second iteration. After the first iteration, the fine-level FE results identified the following critical aspects:

- The natural frequency spacing constraint is violated, as the 3D model edge-wise frequency is approximately 4% lower than the one predicted by the coarse-level beam model.
- Significant stress concentrations are present at the initiation sections of spar caps, shear webs and trailing and leading edge reinforcements, around 3% and 10% span.
- Fatigue constraints are violated at 10% span due to the same stress concentrations, with a fatigue damage index exceeding 1.8.
- The thickness of the blade external shell core around 10% span is not sufficient to resist local buckling.

These results are used for tightening some of the constraint conditions for the next coarse iteration, which become:

$$\omega_{1,\text{edge}} \geq 1.04 \cdot 1.20 \cdot 3P, \tag{3.1a}$$

$$d(\boldsymbol{p}_s, D)_{10\%\ \text{skin}} \leq 1/1.8. \tag{3.1b}$$

The first condition modifies the edge-wise frequency spacing constraint, while the second corrects the fatigue condition at 10% span. Since stress peaks do not exceed allowables, no specific action is taken. For buckling, no action is taken to see if the strengthening induced by the tighter fatigue constraint is capable of fixing the problem.

The geometrical changes caused by the updated constraints are illustrated in Fig. 3.8a and 3.8b.

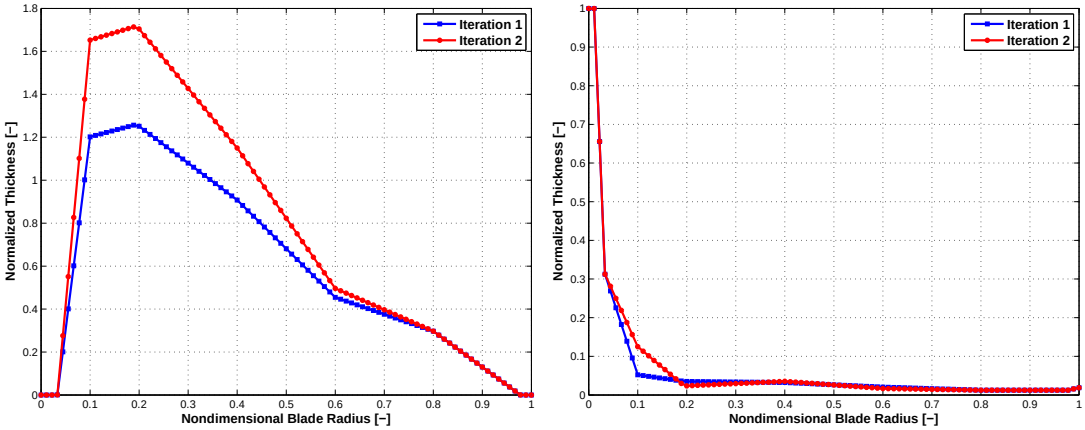

(a) *Trailing edge reinforcement* **(b)** *Skin thickness*

Figure 3.8: *Normalized thicknesses of blade components*

The trailing edge reinforcement has been significantly increased. This change is driven by the need for an increased edge-wise bending stiffness, required for the satisfaction of the modified frequency constraint condition, and the fine 3D edge-wise frequency now satisfies the 20% margin with the three-per-rev harmonic.

The skin thickness in the critical region at 10% span has been increased from 5% to 10% of the root thickness, so as to satisfy the more stringent fatigue constraint condition. This has in turn increased the total blade mass by about 1.2%.

The direct effect of increased skin thickness on the fatigue damage index computed on the fine 3D model is illustrated in Fig. 3.9. The figure shows that the previous peak at 10% span is lowered to just below unity, indicating that the design now satisfies the fatigue requirement at the fine-level.

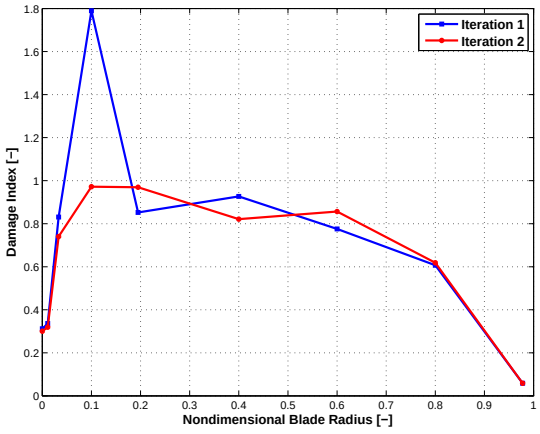

Figure 3.9: *Damage index in external shell at selected sections along blade span*

Furthermore, as illustrated in Fig. 3.10a, the previously identified skin stress concentrations are lowered in the critical region. In particular, the external shell thickness increase at 10% span eliminates the stress peak at that same location, whereas the peak at 3% span, i.e. at the beginning of the spar caps, is only slightly reduced. Changes in

the external shell geometry affect also the spar cap stresses, which are similarly lowered as illustrated in Fig. 3.10b.

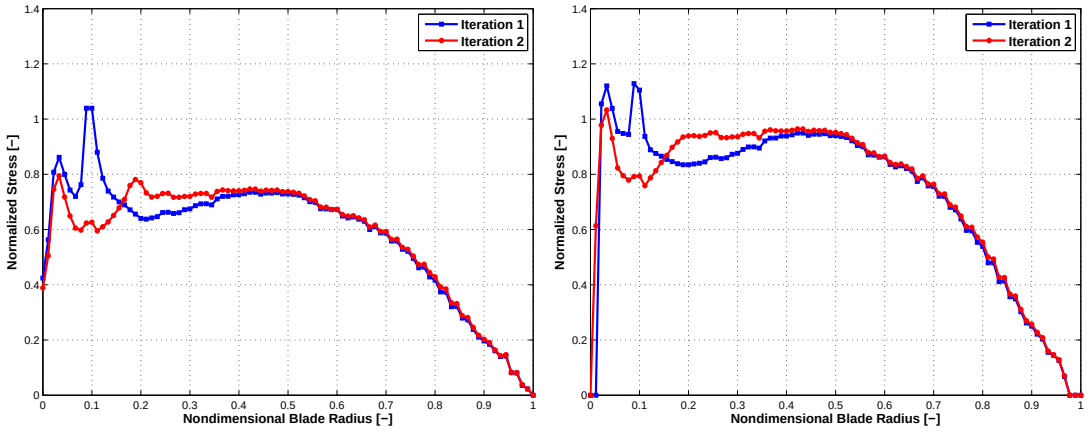

(a) *Maximum stress* $\sigma_{1,\max}$ *in skin* **(b)** *Maximum stress* $\sigma_{1,\max}$ *in spar caps*

Figure 3.10: *Normalized maximum stresses in fiber direction*

Finally, the increased external shell thickness has an indirect effect on the buckling capacity. In fact the lowest buckling eigenvalue is now increased from 0.8 to 2.08, implying that the improved design exhibits sufficient buckling strength so that, in this particular case, an external shell core thickness increase by the secondary design loop proves not to be necessary.

3.1.4 Conclusions

The current section reports a structural design of a 2MW HAWT rotor blade. The main purpose is showing how the local fine effects can be included into the global coarse optimization loop by a scaling procedure of the constraint equations. This approach is really useful when the configuration of the wind turbine is known and the detailed blade design has to be carried out. The inclusion of the three-dimensional effects is performed automatically, speeding up the structural design.

At the beginning the configuration of the 2MW HAWT and the parametrization of the blade structure are reported. The blade design is based on a set of multiple DLC that reproduces the real operative conditions of the wind turbine. The coarse structural optimization algorithm is applied to provide a global optimal configuration, enforcing all design requirements by constraint equations.

A twofold verification is performed by two different 3D FEM, involving either mid-thickness shell element or solid elements. The results of the two models are in good agreement and they exhibit local effects that are not visible in the coarse quasi-3D model. These effects are identified in the blade regions where the hypothesis of the beam theory are no longer valid. For example stress concentrations are shown in the areas subjected to rapid variations of the blade section, i.e at blade span values next to the maximum chord region, and near the boundaries of structural components, such as local reinforcements and shear webs.

Finally the local three-dimensional effects are included into the coarse-level by a scaling of the constraint equations. The interaction between the two modeling levels is

shown, highlighting the effects of the scaling of the constraints on the thickness of the structural components of the blade. Notice that the constraint scaling process provides the best results only if it is applied with attention by an expert analyst. Usually a selective constraint scaling procedure generates a more efficient blade design, as exemplified by the treatment of the buckling requirement. In this case a buckling free configuration is achieved by the increase of local strength due to fulfill the fatigue life requirement. So the core thickness is kept constant, limiting the rise of the nonstructural masses and therefore of the blade overall mass.

3.2 Blade Structural Design: 10MW test case

The DTU 10MW Reference Wind Turbine (RWT) is chosen as 10MW test case because it is a good example of the next generation HAWT, allowing a significant application of the implemented algorithms. Furthermore, the original configuration data are freely available to research purposes at the project website [91], facilitating the usability of the current thesis. The wind turbine configuration is defined in Sect. 3.2.1, describing the parametrization of the DTU 10MW RWT by the current optimization variables. The effects on the global blade design due to nonstructural mass and blade root configuration are examined as well. Section 3.2.2 reports some information about sizing procedure of the root bolted joint, showing the potentialities of the detailed 3D FE analysis.

3.2.1 Baseline wind turbine and model parametrization

DTU 10MW RWT is a concept machine developed by Danmarks Tekniske Universitet. Main wind turbine characteristics are reported in Tab. 3.6, the 3D shape of the blade is shown by Fig. 3.11, while a complete list of model data and DTU design criteria are listed in [92].

Table 3.6: *DTU 10MW RWT Main Data*

Data	Value
Wind Regime	IEC Class 1A
Rated Power	10 MW
Blades number	3
Cut in wind speed	4m/s
Cut out wind speed	25m/s
Rotor Diameter	178.3m
Hub Height	119.0m

The original DTU 10MW RWT blade structure is parametrized by the optimization variables reported in Sect. 2.3.3. The main structural elements of the original configuration are considered. Table 3.7 shows the configuration data and Figure 3.12a displays the components of a standard blade section. External shell, spar caps and multiple shear webs are the classical blade components. They provide bending and torsional stiffness to the blade, keeping the aerodynamic shape as constant as possible. Unidirectional fiberglass reinforcements are local stiffening elements to increase the structural efficiency. Two reinforcements are placed at the Leading Edge (LE) and at the Trailing Edge (TE) of the blade section, while the root reinforcement is superimposed to

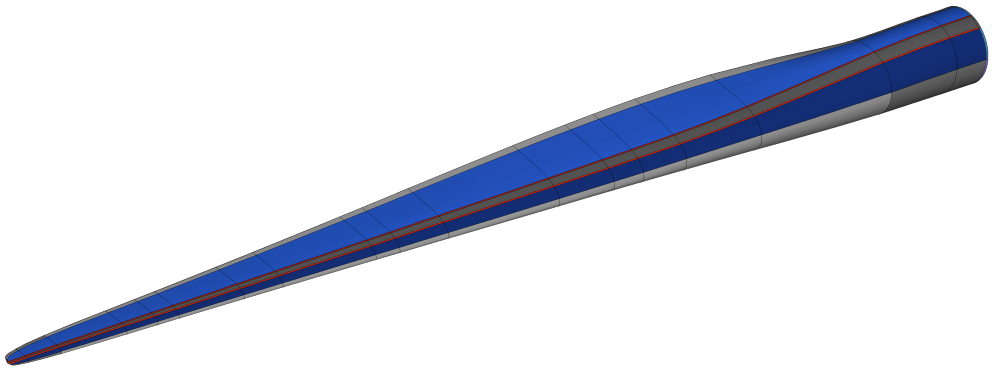

Figure 3.11: *10MW HAWT: Baseline blade 3D external surface*

the external shell in the blade root region. The thickness of the core is estimated for each blade section to generate a buckling free configuration. The elements reported in Fig. 3.12b are considered at coarse-level in the core thickness estimation, while a generic sectional distribution could be adopted on each blade section at fine-level. The nodal unknowns are located at nondimensional span-wise coordinate equal to: 0, 0.01, 0.025, 0.05, 0.1, 0.22, 0.268, 0.3, 0.45, 0.65, 0.8, 0.9, 0.95, 0.99, while the other values are obtained by linear interpolation. The mechanical properties of orthotropic materials are estimated by classical lamination theory [92] and they are reported in Tab. 3.8.

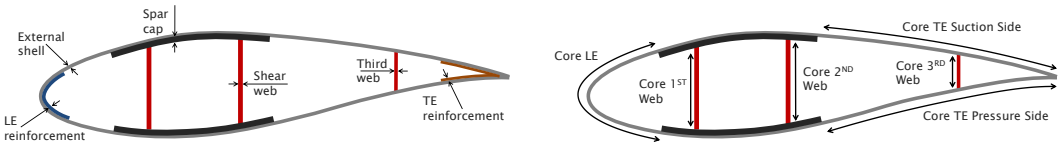

(a) *Baseline blade section components* **(b)** *Baseline blade core thickness*

Figure 3.12: *Parametrization of blade section geometry*

In the current project the attention is also focused on the manufacturability requirements that globally affect the coarse aeroelastic configuration. A first requirement takes into account that an amount of extra material is applied to the blade during the manufacturing process, for example the adhesive to allow the assembly. A second requirement is related to the joint between the blade and the pitch bearing, which must guarantee a safe connection.

Considering the nonstructural mass distribution, the mass of the core is included into the original design. In this project, a rigorous estimation is carried out by including different contributions due to the manufacturing process: adhesive, resin uptake, lightening system, bonding plies and external paint.

Another modification of the original configuration concerns the root of the blade. Laminate thickness is increased allowing the design of the bolted joints between the blade and the pitch bearing. A feasible value is obtained by an in-house experience and it is verified by the design of the root bolted joint with a detailed 3D FEM as reported in Sect. 3.2.2.

These modifications of the blade mass distribution cause variations in the operative

Table 3.7: *Structural configuration of the blade*

Component	Starting section (% span)	Ending section (% span)	Material type
External Shell	0	100	Stitched triaxial -45/0/+45 fiberglass
Spar caps	1	99.8	Unidirectional fiberglass
First and second shear webs	5	99.8	Stitched biaxial -45/+45 fiberglass
Third shear web	22	95	Stitched triaxial -45/0/+45 fiberglass
Trailing and leading edge reinforcements	10	95	Unidirectional fiberglass
Root reinforcement	0	45	Unidirectional fiberglass
External Shell core	5	99.8	Balsa
Web core	5	99.8	Balsa

Table 3.8: *Material properties*

Material type	Longitudinal Young's modulus [MPa]	Transversal Young's modulus [MPa]	Shear modulus [MPa]
Stitched triaxial -45/0/+45 fiberglass	21790	14670	9413
Unidirectional fiberglass	41630	14930	5047
Stitched biaxial -45/+45 fiberglass	13920	13920	11500
Balsa	50	50	150

loads, so the blade structure must be updated consequently. The optimal solution is identified by `Cp-Max` multi-level optimization procedure applied to the blade structure, while the aerodynamic properties are kept constant.

The structural design of the blade is related to the set of DLC considered. A large number of DLC is explored by DTU researchers to define the original DTU 10MW RWT blade configuration. Evaluating all original DLC is infeasible in the current optimization framework due to computational cost, so a selection is made considering the DLC required by the estimation of the constraint equations. In addition to the fact that all fundamental conditions are included, at the end of the optimization procedure the final configuration can be verified considering all DLC to ensure the feasibility of the result. In this project the relevant DLC turn out to be 1.1, 1.2, 1.3, 2.1, 2.3, 6.1, 6.2 and 6.3 [50]. The DLC estimation is related to the external controller, in this case a PID logic is adopted [93] as done when the original configuration is defined [92]. Obviously the DLC evaluation is strictly related to the enforced design requirements. Constraints on blade-tower clearance, ultimate stress, ultimate strain and fatigue damage are applied. Considering the blade-tower clearance, the pre-bend of the blade is modeled as an extra rotor cone angle equal to 2.15 degrees, ensuring the same clearance of the original configuration. Design requirements are applied also to blade modal properties: blade flap frequency separation from three-per-rev of 16% is imposed and a gap between blade flap and lead-lag frequency of 10% is enforced. Active (A) or non-active (N) constraints are reported in Tab. 3.9. It can be seen that constraints on blade-tower clearance and fatigue damage drive the design, while the requirements on ultimate load condition and modal properties are not active.

Table 3.9: *10MW HAWT Baseline structural constraints*

Model	Stress/ Strain	Modal Prop.	Clearance	Fatigue	
Baseline	N	N	A	A	external shell from 22% to 65% span shear web from 22% to 80% span root reinf. from 22% to 45% span

Looking at the constraints on each components, the modifications of the structure due to algorithm activity can be highlighted. A comparison of the design requirements on external shell of the DTU 10MW RTW and the optimized blade, called “Baseline”, is shown in Fig. 3.13. The constraints are reported at the nondimensional span-wise coordinates where the optimization variables are located: 0, 0.01, 0.025, 0.05, 0.1, 0.22, 0.268, 0.3, 0.45, 0.65, 0.8, 0.9, 0.95, 0.99. Following a common convention, a design requirement is satisfied if negative, active if null within a tolerance and violated if positive. The DTU 10MW RTW configuration largely satisfies the constraints, therefore there is room for improvement of the structural performance. The design procedure decreases the external shell thickness, until the constraints assume zero value and they turn out to be active. The “Baseline” blade is designed by fatigue requirements between the 22% and the 65% of the blade length. At the end a more efficient structural configuration is provided, ensuring satisfaction of the constraints.

The blade mass provide a global measurement of the modifications of the laminate thickness. The percent differences of the mass values, nondimensionalized by the DTU

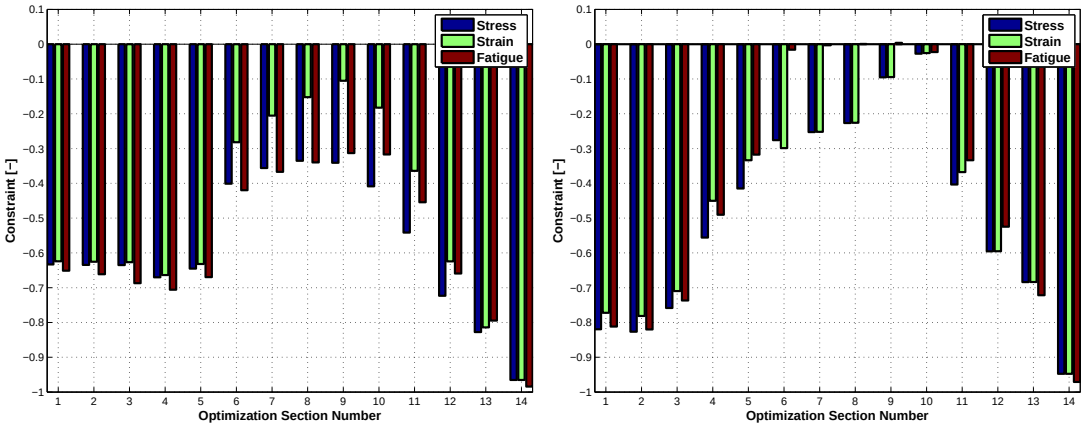

(a) *DTU 10MW RWT* **(b)** *Baseline*

Figure 3.13: *Design requirements on external shell of DTU 10MW RWT and Baseline blade vs optimization section number*

10MW RWT values, are reported in Tab. 3.10. A negative variation is related to a decrease of the mass value so the total mass and the mass of the structural material are decreased by the algorithm. This result is related to Fig.3.13, where an increment of the value of the constraints reflects a decrease of the laminate thickness.

Looking at the non structural mass, the value is increased due to the additional contributions that are neglected in the DTU design: adhesive, resin uptake, lightening system, bonding plies and external paint. The last value represents the structural mass between the blade root and the 10% of the blade length. This item shows the addition of the structural thickness that is required to provide a feasible blade root solution.

The increase of the nonstructural mass on the overall blade and of the structural mass in blade root region partially conceals the advantages of the automatic optimization approach over the classical sizing procedure. The final configuration has a total mass that is similar to the initial one, however the blade structure is subjected to significant modifications, satisfying a greater number of constraints. Therefore, the DTU 10MW RTW and the "Baseline" blade can be compared only keeping in mind that they are not homogeneous because of the different set of design requirements.

Notice that this comparison stresses the important contributions of the optimization procedure, that allows to obtain a structural efficiency difficult to achieve by manual design, limiting the weight when the number of requirements increases.

Table 3.10: *10MW HAWT Mass values comparison*

Mass	Per cent variation
Total	-3.92
Structural	-14.5
Non structural	77.1
Structural ($\eta < 0.1$)	12.5

A brief comparison between the DTU 10MW RWT and the "Baseline" blade is shown in Fig. 3.14. All data are reported with regard to non dimensional blade radius, that assumes zero value at blade root and unitary value at blade tip. Looking at low eta

values of Fig. 3.14a, the imposed increment of the external shell thickness is visible. In the same diagram, a reduction of thickness in the outer part of the blade is evident. This reduction is related to an increment of spar cap thickness, Fig. 3.14b, due to the satisfaction of the blade-tower clearance. This requirement is fulfilled by generating a more efficient structure that minimizes the overall mass. The comparison between original nonstructural mass distribution and updated one is shown in Fig. 3.14c: an increase is reported due to the additional contributions. In this project nonstructural mass is estimated from 10% of blade span to blade tip. In blade root region, where this mass distribution is strictly related to manufacturing techniques and to the structural layout, reasonable values are assumed. A breakdown of the updated nonstructural masses is highlighted in Fig. 3.14d. The different elements of Fig. 3.12b are grouped considering the core pertaining the external shell and the core placed into shear webs. The contributes of the adhesive applied in manufacturing, resin uptake, lightening system and bonding plies are grouped as "Glue mass".

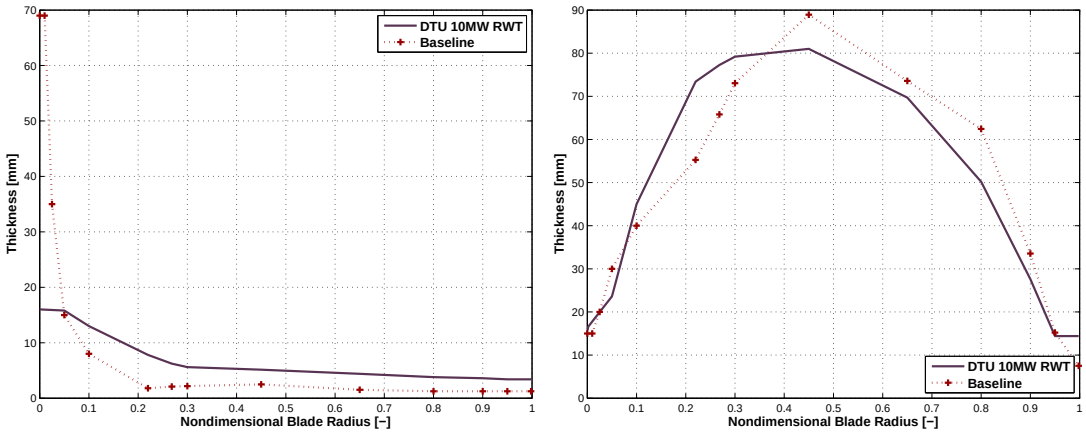

(a) *Baseline blade external shell thickness distribution*

(b) *Baseline blade spar caps thickness*

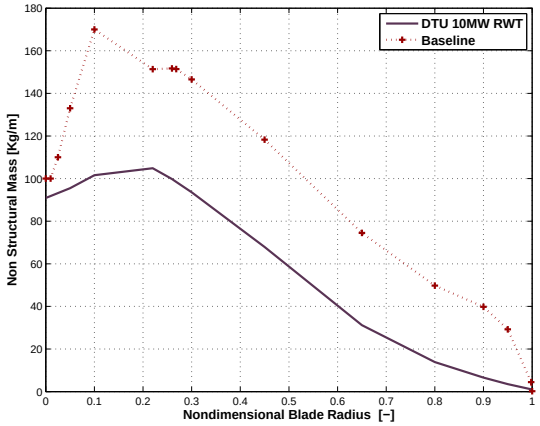

(c) *Baseline blade nonstructural masses distribution*

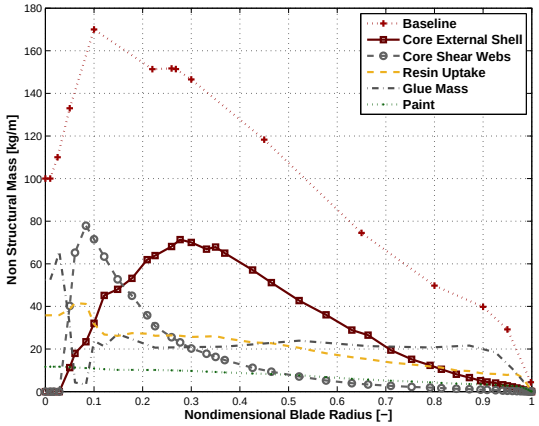

(d) *Baseline blade nonstructural masses breakdown*

Figure 3.14: *Comparison between DTU 10MW RWT and Baseline blade structure*

Multiple interactions between coarse and fine optimization levels are performed during the optimization process. Notice that the structural optimization provides the starting point of the other analysis reported below, such as the couple blade-tower structural

optimization and the aero-structural algorithms comparative. For this reason the attention is focused mainly on the details that affect the coarse configuration, discarding the minor details. An example of the 3D analysis is reported in Fig. 3.15, where the constraint on ultimate stress in the blade root region is shown. The requirement is checked only in proximity of most important blade regions, where optimization sections are defined. In this case the requirement assumes negative value and it is verified by the adopted convention.

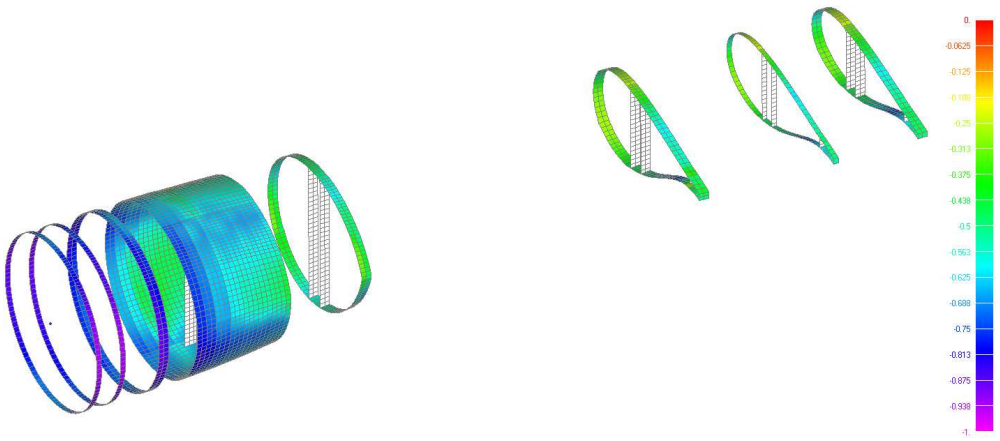

Figure 3.15: *10MW HAWT: 3D FEM of the Baseline blade: constraint on normal stress in external shell*

Further details of the structural optimization are not here reported to avoid useless repetitions. In Sect. 3.2.2 the attention is focused on the design of the blade root bolted joint by the local FE analysis, verifying the blade root laminate thickness imposed in the current section during blade structural design.

3.2.2 Bolted joint design

Sizing of T-Bolt root joint is carried out as reported by Sect.2.6.1, combining the results of the detailed `MSC Nastran` 3D finite element model of the root region and the guidelines of the international standards. The procedure provides the configuration of the bolted joint and it verifies the layout of the laminate in blade root region. Notice that usually different configurations of root joints are adopted on large blades, for example threaded inserts [24], however the classical T-bolts solution is simpler to be analyzed and it supplies a preliminary verification of the blade root layout.

Bolts of different lenght are considered to reduce the drilling negative effects on root laminate. A configuration with 270 T-Bolts satisfies the design requirements about ultimate stress and fatigue life as reported in Tab. 3.11. The table shows that the fraction of external load carried by the short bolt is slightly higher than the fraction associated to the long bolt. Looking at the safety factors, the bolts are designed by fatigue requirements, while the ultimate stress appears to be a minor parameter. Notice that a constraint is satisfied if the value of the safety factor is equal or larger than one.

The stress field on each component can be examined by looking at the results of the detailed FE model. For example a preliminary analysis can be performed by loading the blade root laminate, after removing the bolts and the barrel nuts. Figure 3.16 shows the results of this analysis, reporting the entire sector of laminate and highlighting the

Table 3.11: *10MW HAWAT Blade root bolted joint details*

Data	Short Bolt	Long Bolt
Thread size	M36	M36
Bolt grade	10.9	10.9
Fraction of external load on bolt	14.2%	16.1%
Ultimate load case Safety factor	2.21	2.22
Fatigue life Safety factor	1.18	1.09

stress concentrations that occur at the hole of the barrel nuts associated to the shorter bolt.

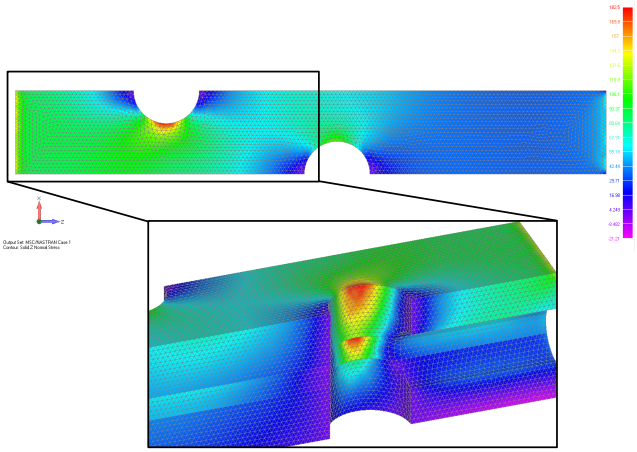

Figure 3.16: *Normal stress concentration on blade laminate due to the holes of bolted joint*

A compressive stress, due to the preload of the bolts, affects the picth bearing. Figure 3.17 reports a contour of the longitudinal stress, highlighting the contact region between the heads of the bolts and the pitch bearing surface. In this region the modulus of the compressive stress on the pitch bearing is maximum.

Finally the stress field in bolt bolts and barrel nuts is displayed by Fig.3.18. When the external load is applied, an increase of the stress value in the necked region of the bolts is clearly visible.

The analysis of the root bolted joint implies the verification of the imposed blade root laminate thickness as reported in Sect. 2.6.1. In this test case, when the design requirements are satisfied on the bolted joint, the blade root region is verified too. This results validates the global configuration determined in Sect. 3.2.1 and it makes the 10MW Baseline blade available to the other studies reported below.

3.2.3 Conclusions

This section shows how the structural optimization techniques can be exploited to apply moderate modifications to an existing blade configuration. A 10MW HAWT is considered to highlight the application of the current method on the wind turbine of

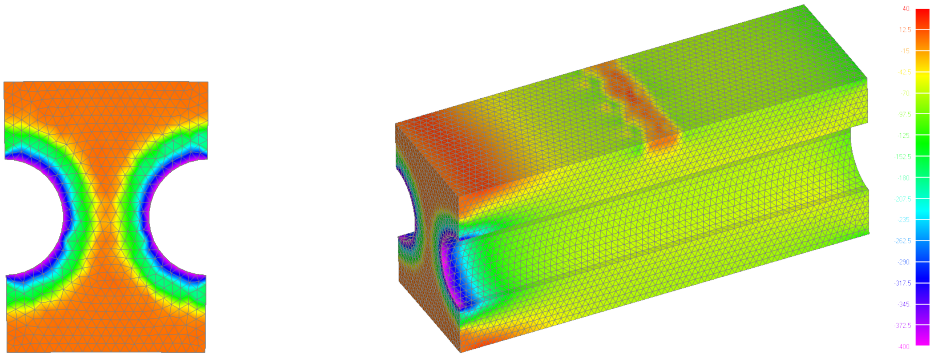

(a) *Contact surface of the pitch bearing with preloaded bolts heads*

(b) *3D view of bearing sector*

Figure 3.17: *Contour of the longitudinal stress in pitch bearing due to preloaded bolts*

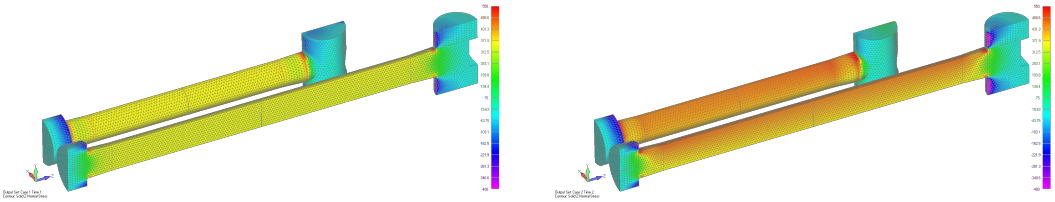

(a) *Bolts subjected to preload*

(b) *Bolts subjected to preload in ultimate load condition*

Figure 3.18: *Contour of the longitudinal stress in bolts and barrel nuts assembly*

the next generation. The original configuration is the DTU 10MW RWT, a conceptual wind turbine developed by the Danmarks Tekniske Universitet. Small modifications of the nonstructural mass and the blade root laminate are applied to satisfy technological constraints and to ensure the blade manufacturing. This revision influences the load envelope and it requires a redesign of the blade structural layout. This procedure is performed by selecting the sizing DLC and reproducing all operative situations of the wind turbine. Multiple interactions between coarse and fine-level are performed to provide a structural configuration that satisfy the requirements globally.

After defining the Baseline blade configuration, some results about the root bolted joint are reported. The potentialities of the local 3D FEM are exploited to magnify the blade root region, showing the local effects fundamental to design the bolted joint. The final configuration is obtained by an iterative procedure based on progressive updates of the model, fixing the requirements not yet satisfied. In Sect. 3.2.2 the final configuration of the joint is reported, as well as the stress field in the blade root laminate, in the pitch bearing and in the assembly of the bolts and the barrel nuts.

Notice that the load fraction on each bolts is fundamental in the bolt sizing procedure because it affects the preload and therefore the safety factors. The load fraction is related to the bolts characteristics but also to the stiffness of both the blade laminate and the pitch bearing. This effect implies a first interaction between the coarse-level, that define the blade root laminate thickness, and the fine detailed 3D FEM, that analyzes the bolts assembly. A second connection between the two modeling levels is due to the local stress concentrations caused by the holes, as reported in Fig. 3.16. In this case a direct correction of the design requirements of the coarse-level can be applied as described for 3D FEM of the entire blade, including in the coarse-level the effects that are visible only on a detailed fully three-dimensional model. Therefore the global blade configuration is connected to the local modeling of the blade root, requiring a local verification of the bolted joint that affects the global layout of the blade.

At the end of structural design, a 10MW HAWT blade is obtained and it can be exploited as initial configuration to validate the coarse optimization algorithms. In this procedure the attention should be focused only on the global blade design and on the parameters affecting the coarse configuration. The interaction between the two modeling levels should regard only the main structural details, discarding the minor parameters. In this case, small constraints violations at fine-level are allowed as long as their effects on the coarse optimization configuration are minimal. For this reason, the fine analysis has the task of verifying the coarse initial configuration, without playing an active role in coarse optimization algorithms verification. This choice aims at a simplification of the validation procedures, reported into the next sections. Obviously, when the optimal coarse solution is obtained, the multi-level interaction can be repeated, if a detailed blade design is required.

3.3 Blade-Tower Structural Design

The design of the blade and tower structure is here reported. For sake of simplicity only the coarse optimization level is considered, deferring the fine-level verification to a later phase of the project. Two test cases are reported: 2MW HAWT is considered in Sect. 3.3.1, while the 10MW HAWT is shown in Sect. 3.3.2. In both cases, the design

requirements that drive the tower sizing are shown, highlighting how the active control can play a key role in tower definition.

The current section aims also at showing how the implemented techniques can be useful to identify the best wind turbine configuration by trend studies. Fixing the boundary conditions of the optimization problem and the design requirements, it is possible to generate a population of wind turbines characterized by some relevant parameters. In this case the effects of the wind turbine configuration on the CoE are considered, identifying the optimal layout of the overall machine.

3.3.1 Optimal Wind Turbine Configuration: 2MW test case

2MW HAWT is considered as test case to investigate the performance of the blade-tower structural design algorithm. The wind turbine data and the structural parametrization of the blade are the same as the ones reported in Sect. 3.1.1. As initial guess is considered the blade configuration optimized at coarse-level, without applying fine-level correction for the reason reported in Sect. 3.2.3.

The support tower is modeled by 5 steel tubular sections: the length of first four sections, from the foundation to the tower top, is 15 meters, while the last section at tower top is 19 meters long. Mass and inertia of the junction flanges between the tower sections are included by indicative data to increase the realism of the model. The thickness of each tower segment is linearly interpolated between the two ends. If a stepwise thickness distribution is required, a discretization can be applied at the end of optimization, or an optimization with constant thickness segment can be performed.

DLCs considered by sizing procedure are 1.2, 1.4, 1.5, 1.6, 1.7, 2.2, 2.3 and 6.1 [50]. Design requirements include: flapping blade frequency placement at least 20% above three-per-rev harmonic, frequency separation at least 20% between blade flap and lead-lag eigenvalues, tower modal frequencies 15% above one-per-rev harmonic, verifications on blade-tower clearance, limits on ultimate stress, ultimate strain and fatigue damage on both blade and tower (see 2.16d-2.16k).

The implemented approach considers blade and tower optimization variables in a unified process. This methods is defined “coupled” and it allows to take into account the impact of the design of one component to the other. The coupled design is compared to the results of an iterative approach, where blade and tower properties are optimized iteratively, that is the usual procedure in structural sizing.

The optimized tower configurations are reported in Fig. 3.19a and 3.19b toward non-dimensional tower height that assumes zero value at the base and unit value at the top. The tower obtained by the coupled approach has a smaller diameter and a larger thickness than the structure obtained by the iterative approach, that is heavier therefore more expensive. However the design is driven by the minimum clearance constraint between blade tip and tower, so a slender tower ensure a larger clearance and a lighter and cheaper blade. Figure 3.20a highlights the impact on the thickness distribution of the blade external shell toward non-dimensional radius measured from the blade root till the blade tip. The spar cap thickness appears to be almost constant as reported by Fig 3.20b. The best compromise between the weight of two components is identified by the CoE model as merit figure and it is obtained by the coupled algorithm.

The criteria that drive the design are identified looking at the active constraints at the end of optimization. A constraint is satisfied if negative, active if zero within a

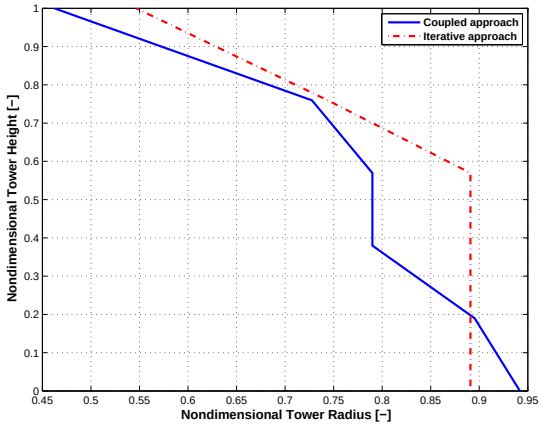

(a) *Tower radius distribution*

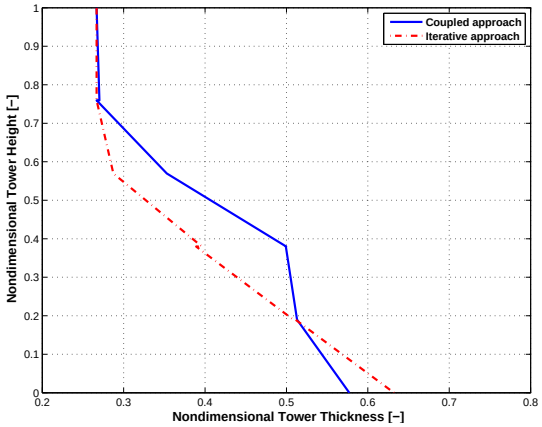

(b) *Tower thickness distribution*

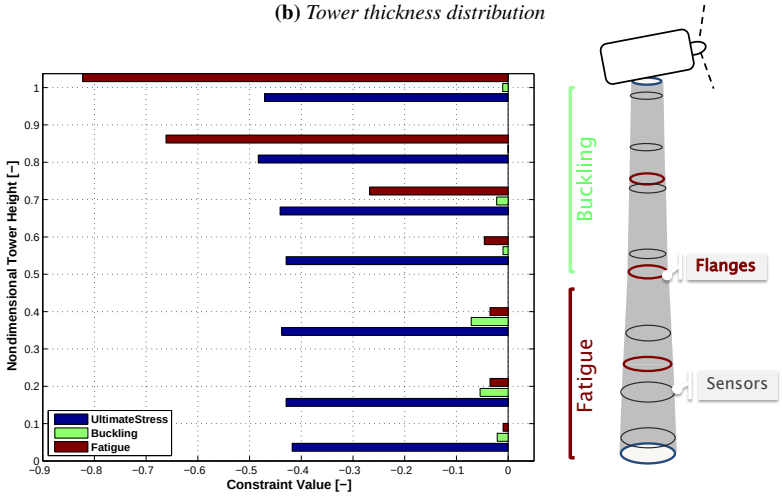

(c) *Coupled approach design requirements vs nondimensional tower height*

Figure 3.19: *2MW HAWAT: Coupled vs Iterative approach: non-dimensional tower radius, tower thickness and design requirements toward tower height*

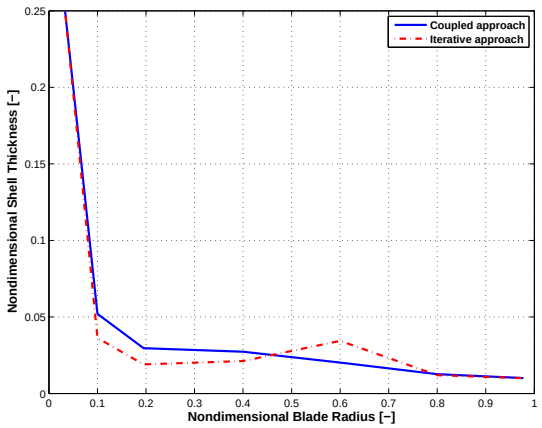

(a) *Blade external shell thickness*

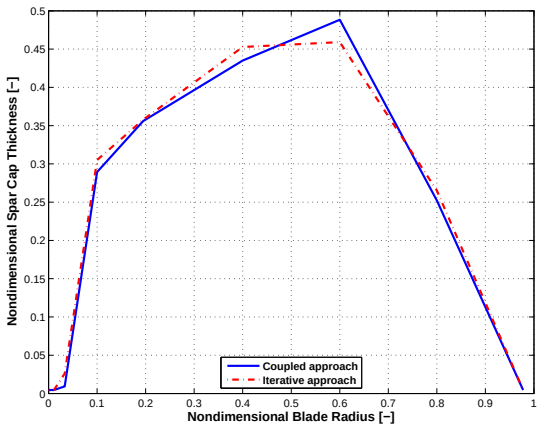

(b) *Blade spar cap thickness*

Figure 3.20: *2MW HAWAT: Coupled vs Iterative approach: non-dimensional blade external shell and spar cap thickness distribution*

certain tolerance and violated if positive. The blade structure exhibits active design requirements similar to the ones reported in Sect. 3.1.1, so they are not here reported. Looking at the constraints along the tower height, Fig. 3.19c, the lower part is sized by fatigue life requirements, the upper part is designed by buckling, while the ultimate strength requisite is always fulfilled. It should be noted that the controller law has a great impact on the tower loads and it represents a further design parameters to define the optimal configuration. In this case the wind scheduled LQR is tuned properly to obtain a good trade off between ultimate loads, fatigue loads and power production.

The comparison between coupled and iterative optimization approach shows the importance of clearance value. Considering a classical HAWT several parameters influence the clearance: rotor cone angle, nacelle uptilt angle, blade prebend and rotor overhang. Some of these are shown in Fig. 3.21.

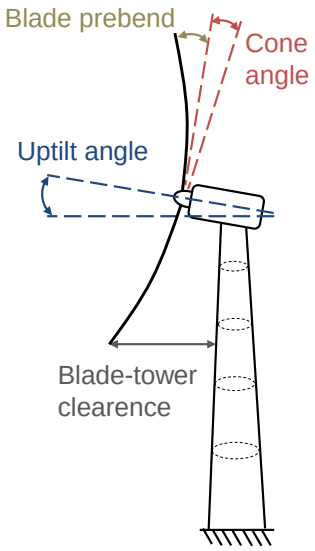

Figure 3.21: *Parameters that influence tower blade clearance*

Among these variables, cone angle and uptilt angle are selected to perform trend studies, highlighting the shape of the merit figure around the design point. The optimization of the blade-tower structure is repeated varying the cone angle and the uptilt angle, generating a comparable group of wind turbine subjected to the same constraints set. Macro-parameters that characterize each configuration are reported in figure 3.22a and 3.22b in non-dimensional form. If the cone angle or the uptilt angle increase, the blade tower clearance increases, allowing the construction of more flexible blades and tower with larger diameter, resulting in lighter an cheaper structures. Therefore the summation of the cost of the three blades and the tower, identified as "Investment", tends to decrease. At the same time if the machine configuration is changed acting on these two angles, the AEP varies due to the different relative orientation of the rotor blade towards the mean wind direction. The AEP is estimated considering DLC 1.2 [50] in standard power production state for different mean wind speeds at hub height and weighting mean power by Weibull probability function. If the rotor cone angle increases, the AEP remains almost constant, while lager reduction is connect to nacelle uptilt increment. The "Investment" and the AEP are unified by CoE model, the

best solution is obtained by setting the rotor cone angle equal to 2 degree and nacelle uptilt angle equal to 6 degree.

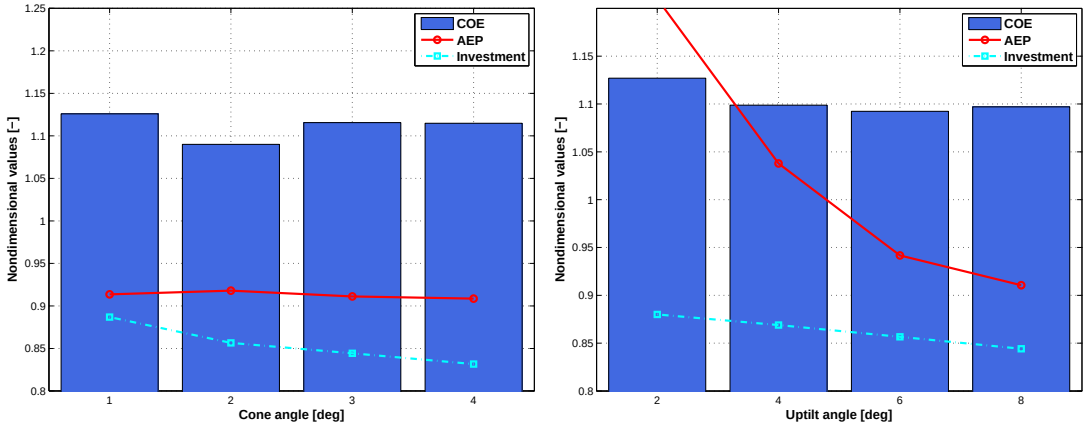

(a) *Rotor cone angle* **(b)** *Nacelle uptilt angle*

Figure 3.22: *2MW HAWT: Trend studies*

The reported trend analyses are characterized by the variation of only one parameter at time. The results can be enriched if the mixed terms are examined too, providing the entire response surface. Since this procedure is well known, it can be postponed among the further developments.

3.3.2 Optimal Wind Turbine Configuration: 10MW test case

The combined blade-tower structural optimization is performed by considering 10MW HAWT Baseline blade as guess point. This configuration is achieved by the structural optimization of the DTU 10MW RTW performed in Sect.3.2. As already pointed out for 2MW HAWT blade-tower design, the control strategy has a remarkable effect on tower fatigue. The tuning process of the controller is crucial to achieve a good compromise between the loads, that are applied to the wind turbine, and the power production, related to the satisfaction of the reference conditions. The baseline structural blade design, reported in Sect. 3.2, is achieved by DTU PID controller [93], applying a constant power control strategy. Since the procedures that allows an automatic tuning of DTU PID controller are not available, it is convenient to switch to collective pitch-torque POLI-Wind LQR controller [62]. Adjusting the LQR weighting matrices properly, it is possible obtaining a control law that reduce the fatigue damage on the tower, keeping constant the AEP. A comparison of the design requirements along the tower height is reported in Fig. 3.23, showing the initial values of the constraints given by the PID controller and the final values provided by the LQR controller after the tuning procedure. The values refer to the original tower configuration, before applying any modification to the structural properties. The sensor number is equal to 1 at tower base and it is 20 at the tower top. Notice that the final value of the design requirements are negative and so they are satisfied. The satisfaction of the constraint equations implies a reduction of the ultimate and fatigue loads by the tuning of LQR controller. Obviously, Figure 3.23 does not provide an absolute comparison of the performance of the two controllers because the tuning of the PID controller has not been updated. The comparison would like to

show that a lot of groundwork comes prior to apply the optimization procedure. As in a real design case, the control laws play a key role and they are fundamental to achieve the optimal result by means of an appropriate tuning procedure.

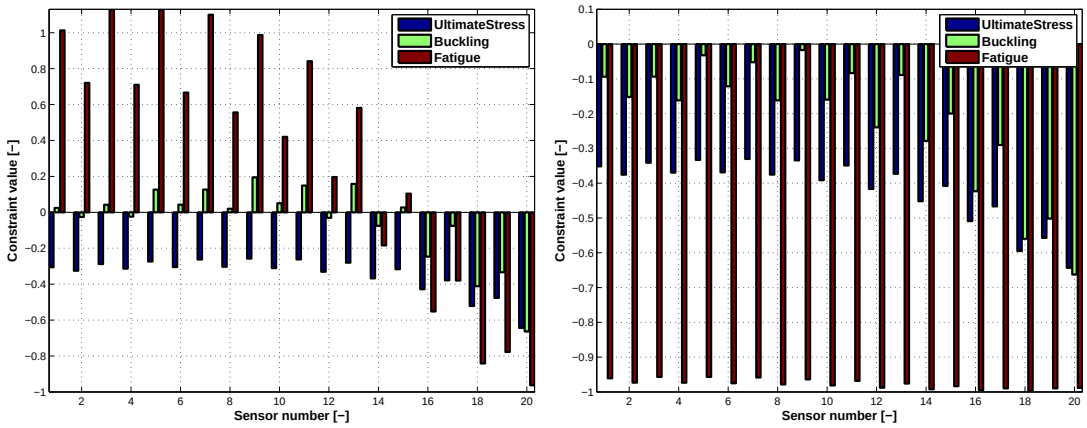

(a) *PID controller* **(b)** *LQR controller*

Figure 3.23: *10MW HAWT Design requirements on tower vs sensor number (1 at tower base, 20 at tower top)*

Since the fatigue requirement on tower structure is limited, a redesign of the original layout is possible, avoiding a significant weight increase of the tower structure. The tower is modeled by 6 steel tubular sectors with linear variable thickness. The first five sections, from tower base to tower top are 20 meters long, while the higher sector is 15.63 meters long. Tower thickness and diameter is fixed at tower boundaries as design constraint, mass and inertia of connection flanges are not included in the optimization procedure. The blade-tower structural optimization is performed only at `Cp-Max` coarse aeroelastic level, focusing on the best compromise in term of configuration and leaving the details to an advance phase of design.

Looking at macro-parameters reported in table 3.12 a sensible reduction is obtained in term of blade and tower mass applying the combined blade-tower optimization procedure. Also the summation of the cost of three blade and the tower cost, defined as "Investment", decreases as well.

Table 3.12: *10MW HAWAT Blade-tower optimization result*

Data	$\Delta_{\%} = 100\frac{Optimized-Baseline}{Baseline}$
Blade mass	−3.5%
Tower mass	−7.3%
Investment	−5.1%

Tower diameter and thickness distribution toward non-dimensional height are reported in Fig. 3.24a and 3.24b, while external shell and spar cap thickness distributions are listed in Fig. 3.24c and 3.24d. Also in this case blade-tower clearance requirement is fundamental: this active constraint forces `Cp-Max` to increase the clearance reducing the tower diameter locally. Therefore a small reduction of spar cap thickness is possible, increasing the blade flexibility and reducing the blade weight. Looking at the

blade external shell only minor modifications are applied, fixing local constraints on optimization sections.

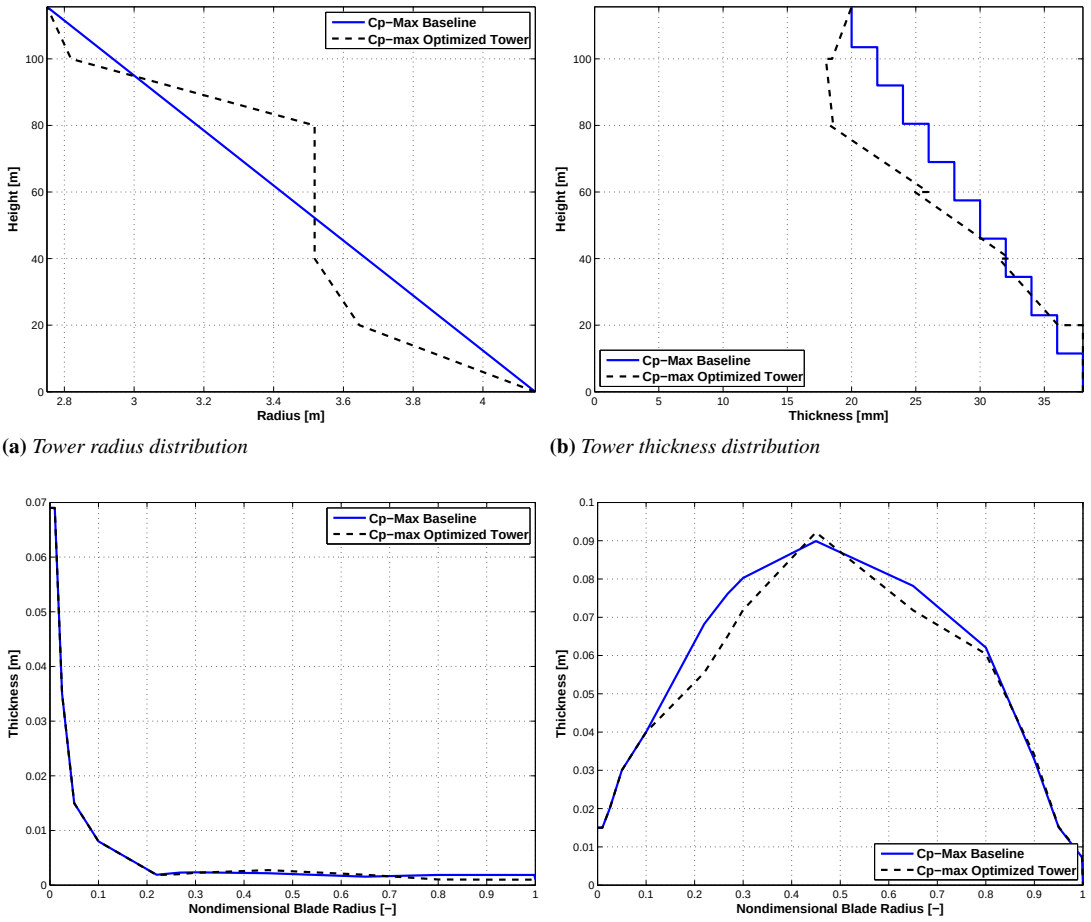

(a) *Tower radius distribution*

(b) *Tower thickness distribution*

(c) *Blade external shell thickness distribution*

(d) *Blade spar caps thickness distribution*

Figure 3.24: *10MW HAWT: Combined blade-tower structural optimization*

Conscious of the importance of the clearance value, two trend studies are performed varying rotor cone angle and nacelle uptilt angle as done for 2MW HAWT. Figure 3.25a shows that the effects of the rotor cone angle on the cost of energy are limited. Even if the minimum of the COE is obtained for the nominal value of the cone angle, the merit figure is almost stationary. Looking at nacelle uptilt angle in Fig. 3.25b, a gain in term of COE is obtainable if the angle value is decrease to 3 degrees. This reduction causes an increment of the initial investment, directly related to blade and tower mass, but at the same time an increment of AEP compensates this effect obtaining a benefit in term of COE.

3.3.3 Conclusions

The validation of the coarse optimization procedures to perform blade and tower structural design has been reported. The results on two different test cases are shown, proving the applicability of the procedure to standard industrial case but also to wind turbine

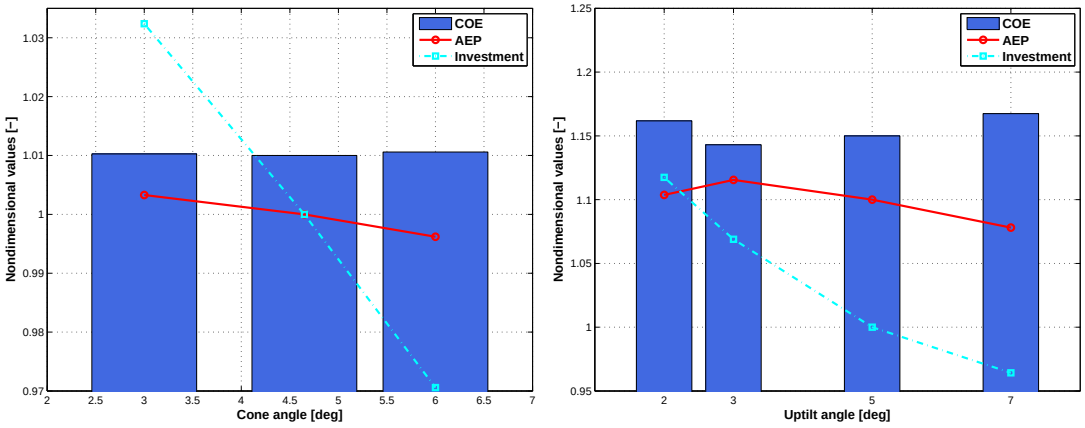

(a) *Rotor cone angle* **(b)** *Nacelle uptilt angle*

Figure 3.25: *10MW HAWT: Trend studies*

research configurations.

A standard 2MW HAWT is considered at first, reporting a comparison between the coupled approach and a standard iterative approach. The method identifies the best trade-off between the blade and the tower properties when the design of the two components is performed by a monolithic procedure. For this reason, the structural design provided by the coupled approach proves to be more efficient, in term of CoE, than the iterative result. The tower-blade clearance parameter is one among the design requirements that most affects the final result. It is possible to include this parameter into the optimization procedure by trend studies, focusing the attention on the variables that influences the clearance directly. The effects of the rotor cone angle and the nacelle uptilt angle are examined, generating a population of wind turbines that is parametrized by different value of these variables. The CoE model allows to consider the structural benefit and the AEP variation of each configuration, identifying the optimal solution. The analyses prove that the nominal values of cone angle and uptilt angle are the optimal ones.

A 10MW HAWT is taken into account in the second part of the section, highlighting the importance of the tuning of the control law in wind turbine tower design. A good compromise between buckling load, fatigue load and AEP is achieved by the adjustment of the LQR weighting matrices. When a proper tuning of the control law is obtained, it is possible performing the coupled sizing of the blade and the tower properties. These results are in good agreement with the one reported for the 2MW HAWT. The importance of the clearance parameter is evident and it suggests to set up another trend analyses, involving the rotor cone angle and the nacelle uptilt angle. In this case a weak dependency of the CoE to the rotor cone angle is shown, while a slight reduction of the nacelle uptilt angle proves to be convenient.

3.4 Blade Aero-Structural Design: 10MW test case

The coarse aero-structural algorithms are applied to the open access conceptual 10MW HAWT. This test case is representative of a real design condition and it allows to test

the performance of the algorithms through a direct comparison of the results. After focusing on structural parameters only, it is interesting to consider the evolution of the configuration when aerodynamics and structure are merged in an aero-structural optimization procedure. The current approach aims at a further improvement in terms of CoE, through the combined optimization of the blade structure and the aerodynamics.

The wind turbine data has been listed in Sect. 3.2.1 and they will not be repeated in the current section. The structural Baseline configuration is considered as initial guess. A comparison of the aero-structural optimization algorithms is highlighted by Sect. 3.4.1, showing the pros and cons of each strategy, while the conclusions are reported by Sect. 3.4.2.

3.4.1 Aero-structural optimization algorithms performances

Considering the 10MW HAWT Baseline blade as initial configuration, the developed aero-structural optimization algorithms are compared. The reported results aim at validating the procedures, showing the pros and the cons of each algorithm. Furthermore, the impact of the aero-structural approach on the design is explored, considering the variations of the macro-parameters of each design configuration. More precisely, the values of AEP and blade mass are analyzed to justify the benefit in term of CoE and to provide a better understanding of the algorithm behavior.

It is possible to identify the performance of the algorithms when they are applied to the same optimization problem. For this reason, the same input data are considered, keeping constant the data structure D for all applications. The DLC are set and they are equivalent to the ones reported in Sect. 3.2.1, providing the same boundary conditions. Also the model parametrization is constant: the aerodynamic variables are identical to the ones reported in Sect. 2.4.1, while the structural variables are described in Sect. 3.2.1.

The PAAS approach is considered at first. This choice is mainly due to the simplicity of this technique and to the reliability of the results. Furthermore, the PAAS algorithm allows to explore the solution space, identifying the trend of the merit figure toward some user defined macro-parameters. Obviously, the success of this technique is based on the parametrization chosen by the analyst, requiring a certain level of experience in blade design. The current choice is based on the combination of blade solidity σ and maximum blade chord c_{max}. This coupling aims at well matching the trade-off between aerodynamic performance and structural requirements. As Sect. 2.4.1 shows, aerodynamic characteristics can be increased if σ decreases, while structural efficiency exhibits an opposite behavior with respect to σ. A constraint on c_{max} is also needed to avoid extremely tapered blade shapes that could not capture the cost advantages of an efficient structure. The goal of the choice of the two parameters is to identify a good combination of σ and c_{max} to well sample the space of solutions and to capture the global trend of CoE.

Applying the PAAS algorithm, a parametric family of rotor blades is generated by different values of σ and c_{max}. Aerodynamic optimization and structural optimization are applied in sequence to each blade, maximizing AEP and minimizing blade mass. The results in terms of chord and twist distributions are reported in Fig. 3.26a and Fig. 3.26b. Each design is identified by the label PAASi, where i goes from 1 to 5 when the blade solidity assumes values from 4.0% to 6.5%.

The external blade shape of each PAASi is obtained by imposing the corresponding values of σ and c_{max} as constraints of aerodynamic optimization. Therefore no scaling procedure is applied, but the generation of the external shape is performed by the aerodynamic optimization considering the values of σ and c_{max} selected by the user. This parametrization and the values of the macro-parameters are arbitrary and they are selected to identify a minimum value in the CoE domain.

An interpolation using cubic splines is then run on the σ and c_{max} values and a minimum for the CoE is assumed to exist at σ equal to 5.32% and c_{max} equal to 7.4m. Assuming these values as active constraints, a new optimum aerodynamic shape is generated and subsequently the structural optimization loop is run. The solution found is hereinafter simply named PAAS and can act as a useful comparison with the results produced by the EAIS and MLU automatic approaches.

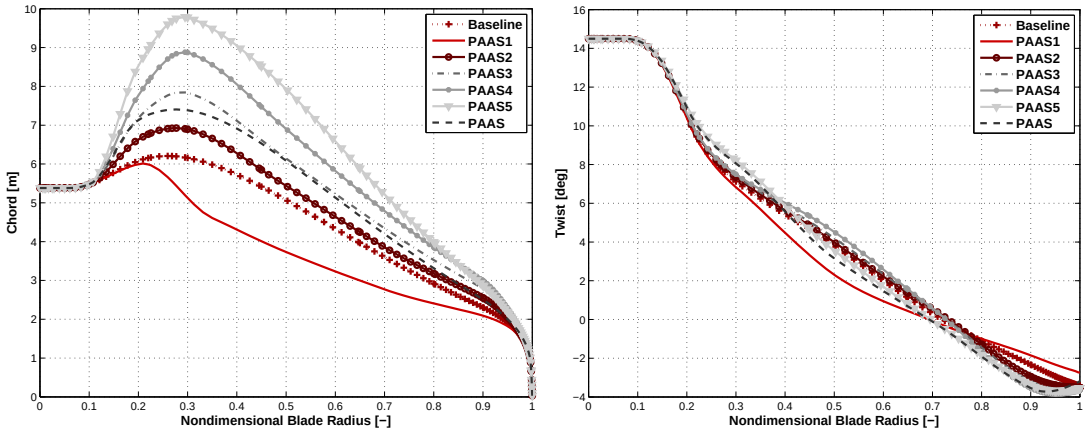

(a) *Chord distribution parametrized by* σ **(b)** *Twist distribution parametrized by* σ

Figure 3.26: *PAAS approach: parametrization of the blade aerodynamic shape*

The blades population shows significant variations of chord distributions due to the solidity requirement. The solution domain is well sampled, providing a database of results useful for the comparison with the EAIS and the MLU approach. A specific trend is not identified in twist distribution because there are no constraints active on this parameter, so its value is set by the algorithm to achieve the maximum AEP. Looking at the blade population, the minimum CoE is produced by the design PAAS. It is now interesting to compare these results with the ones produced by the EAIS approach and the MLU approach that are designed to obtain the optimal solution automatically.

A comparison of the macro-parameters for all the design is reported in Fig. 3.27. The percent variations from the Baseline blade are shown: a positive value in the bar diagrams implies an increment of the current model compared to the Baseline configuration. The label EAIS identifies the results of the optimum design from the EAIS approach, while MLU refers to the optimum design produced by the MLU approach.

In Fig. 3.27a the comparison of the merit figure is reported. The largest reduction is obtained by the MLU approach, followed by the EAIS approach. Examining the blade solidity in Fig. 3.27b, it is evident that the σ values of EAIS and MLU configurations are closely located to the optimum of the PAAS approach. The EAIS and the MLU approaches are therefore able to identify the blade configuration that minimize

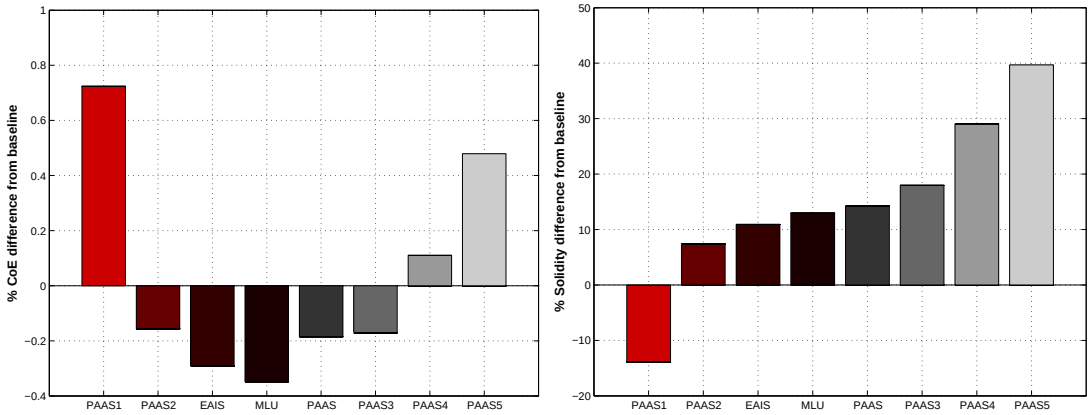

(a) *Comparison of CoE*

(b) *Comparison of blade solidity*

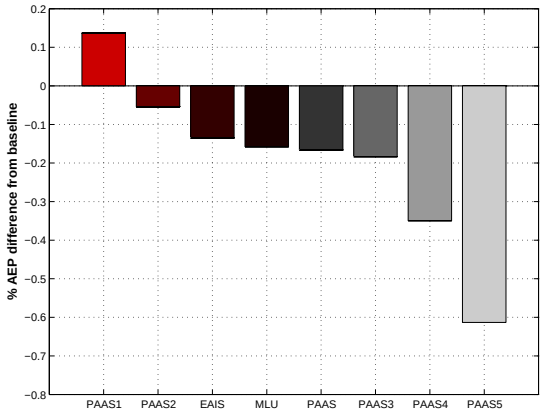

(c) *Comparison of AEP*

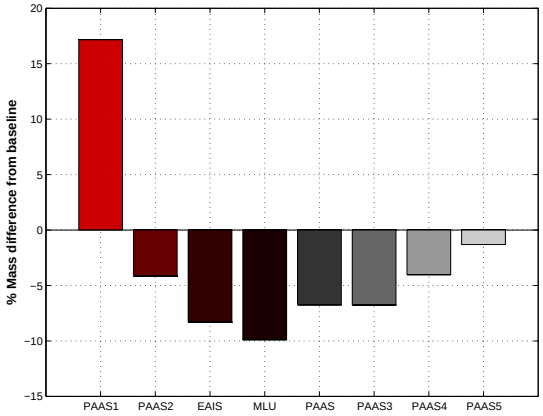

(d) *Comparison of blade mass*

Figure 3.27: *Aero-structural algorithm: comparison of macro-parameters v.s. Baseline configuration*

the CoE with a solidity in agreement with the PAAS method. The minimum of CoE can be explained looking at the AEP and blade mass diagrams reported in Fig. 3.27c and Fig. 3.27d. The trend of AEP is almost constant and it is opposite compared to σ, i.e. higher solidities cause lower AEP and vice versa. Examining the mass variation, a minimum is instead reported. At low σ values, an increase of solidity leads indeed to a higher structural efficiency and to a reduction of the mass of the blade. However, this is true only until the buckling requirement is not active. At high σ, the blade is indeed characterized by large and thin panels, which are prone to instability. The core thickness is then increased to avoid buckling, causing an increase of nonstructural mass and blade total mass accordingly. Moreover, the automatic approaches EAIS and MLU are more effective in finding the best trade-off between structural and aerodynamic efficiencies, achieving slightly better results than the PAAS approach.

Summarizing, the aero-structural approach obtains a consistent reduction of blade mass, limiting the AEP loss. Considering the three different approaches, the best configuration is obtained by fully automatic procedures. This is a valuable aspect because it assists the analyst, varying the blade aerodynamic shape automatically. Considering the active structural constraints, the designed blades are sized by clearance requirement and fatigue damage. Since the results are similar to the ones reported in Tab. 3.9, no further details are shown in this section. Notice that each aero-structural algorithm aims at the best configuration that satisfies the requirements. Therefore the design margins are automatically reduced by looking for the optimum, until the constraints become active. This is the same trend that the structural optimization highlights in Sect.3.2.1, where an example of constraints variations on external shell is reported in Fig.3.13 by comparing the design requirements of DTU 10MW RTW and the Baseline blade. The design requirements of the optimal aero-structural designs are similar to the one reported for the Baseline blade, so they are omitted in the current paragraph.

Considering the optimal aero-structural designs, the initial DTU 10MW RTW configuration is recalled. DTU 10MW RTW is the guess point of the structural optimization that provides the Baseline layout, basis of comparison for the study reported in this section. DTU layout is not included in the current diagrams because it does not satisfy all the constraints applied in this case study, therefore it is not possible provide a direct comparison. However, the advantages of the automatic techniques, over the classical design methods of the DTU 10MW RTW blade, can be highlighted by drawing a parallel between the optimal aero-structural configurations and the DTU one.

The aerodynamic configuration of DTU blade is identical to the Baseline blade and it is not repeated here. The AEP is mainly related to the aerodynamic properties of the blade, while the effects of the structural flexibility can be neglected by a rough approximation, so the AEP value is considered almost equal to the Baseline one.

The difference of the blade mass can be estimated by merging the effects of the structural optimization to the advantages of the aero-structural approach. A blade mass reduction of 13% is achieved by the results of the MLU approach compared with the DTU configuration. This causes a decrease of the cost of the single blade of 12% and a reduction of CoE of 0.6%. These results are similar if the PAAS and EAIS methods are considered.

It should be remembered that the DTU 10MW RTW blade satisfies a smaller set of design requirements than the blades reported in this section. Therefore the highlighted

differences are increased if the same set of constraints is considered. For this reason, the importance of an automatic design procedure is undeniable and it is the only way to maximize the performance.

A detailed comparison of the optimal aero-structural designs is reported. The aerodynamic parameters are shown in Fig. 3.28, while the thickness of the most important structural components is displayed by Fig. 3.29. The chord diagram shows that the distributions of designs EAIS and MLU lie between design PAAS2 and PAAS3, justifying the solidity trend of Fig. 3.27b. Twist distributions show a mismatch when nondimensional blade radius goes from 0.2 to 0.35, while a good agreement is obtained between 0.4 and the blade tip. This small discrepancy is due to the different merit figures considered when aerodynamic parameters are examined. In the PAAS approach the AEP is taken into account, while in the EAIS and MLU approaches the twist is assigned by the maximization of the power coefficient. EAIS and MLU designs exhibit slightly higher power coefficient, but the difference in term of AEP due to this variations is negligible. So the different merit figures produce this gap in twist distribution that turns out to be negligible in terms of CoE.

Looking at the structural parameters, a good agreement is reported. The results of EAIS and MLU designs are always placed close to the PAAS design, showing how the EAIS approach and the MLU approach are able to identify the optimal configuration.

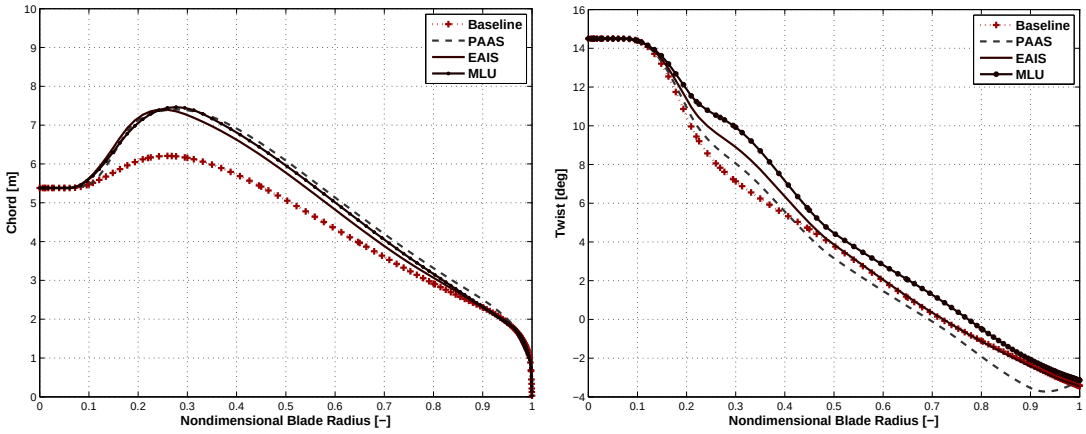

(a) *Blade chord* **(b)** *Blade twist*

Figure 3.28: *Aero-structural algorithm: comparison of blade aerodynamic parameters*

Regarding the relative computational costs, the comparison between the three approaches is reported in Tab. 3.13, highlighting the contrast between the higher automation of the processes and the higher computational costs. The MLU approach obtains the best trade-off, which however comes together with a significantly higher complexity of the code.

Table 3.13: *Relative computational costs for the aero-structural algorithms*

Algorithm	PAAS	EAIS	MLU
Relative computational costs	1	3	1.25

It should be remembered that the developed procedure aims at identifying the best

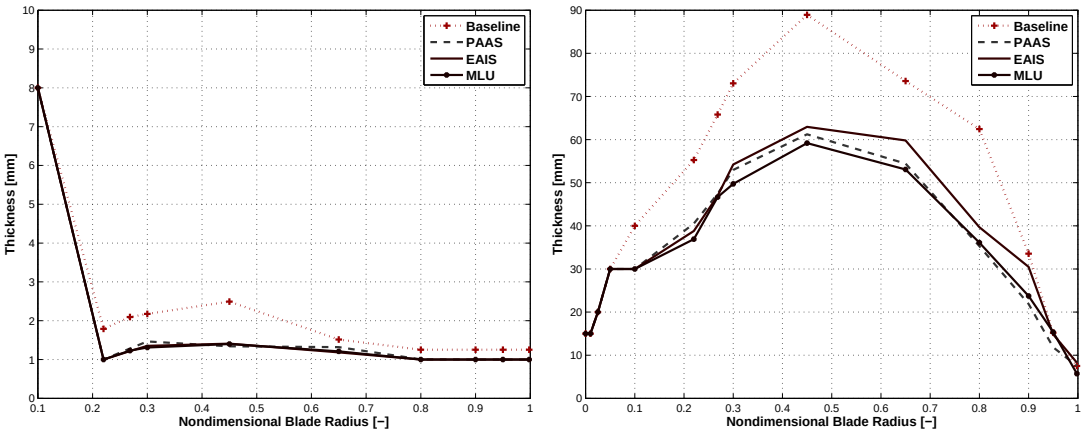

(a) *External shell thickness distribution*

(b) *Spar cap thickness distribution*

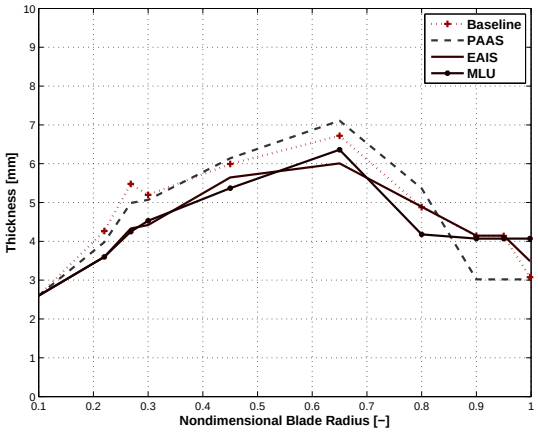

(c) *Shear web thickness distribution*

Figure 3.29: *Aero-structural algorithm: comparison of blade structural parameters*

blade design, for a given wind turbine configuration. So, in this work only aero-structural properties of rotor blade are modified, leading to limited variations of CoE. This is however a necessary step between the single field optimization, the optimal design of aerodynamics or structure, and the holistic design of the wind turbine. Global parameters, such as rotor radius, tower height, nacelle uptilt angle and rotor cone angle, must be considered to achieve larger CoE improvements. All these modifications will be included in a further development of this project, that will be based on these validated aero-structural optimization algorithms.

3.4.2 Conclusions

This section validates the coarse aero-structural optimization algorithms on a conceptual 10MW HAWT. The optimized Baseline configuration is considered as initial guess and further improvements are sought by the interaction of the blade structure and the aerodynamics during the design.

At the beginning the PAAS method is considered to generate a parametric population of wind turbines. Each element is characterized by imposed solidity and maximum chord value. Varying these two parameters, a good trade-off between the structural properties and the aerodynamic characteristics is obtained. The solution domain is explored, identifying the combination of solidity and maximum chord that provides the optimal solution.

Obviously the PAAS method is based on a user defined parametrization, requiring the expert analyst's intervention. The user's task can be limited by EAIS and MLU methods that provide highly automate design procedures. However, these two approaches identify the optimal solution directly, without giving any information about the solution space. For this reason, the sampling of the solution domain obtained by the PAAS methods is fundamental to validate the EAIS and MLU methods. Exploiting the broad representation of the CoE response surface given by the PAAS method, it is possible to understand if the other design strategies are performing well. This verification is achieved successfully by the presented test case. EAIS and MLU methods provide results that are located between the two best configurations identified by the PAAS approach. Furthermore, EAIS and MLU methods improve the results of the PAAS, achieving a larger reduction of CoE.

In the current section, PAAS, EAIS and MLU aero-structural optimization techniques have proved to be effective in a realist test case. The reported results show that each method presents pros and cons. During the design phase, a lot of parameters have to be considered to select a method instead of another one. Since they are not mutually exclusive approaches, it is suggested that a combination of them could be the best choice during the design. The stability and the reduced computational cost of the PAAS approach allows to perform preliminary analyses that are useful to understand the key aerodynamic parameters that most affect the CoE value. EAIS and MLU techniques can be exploited to obtain a further improvement of the optimal solution or when it is not possible to identify a good user defined parametrization. MLU approach provides an automatic technique at the cost of a slight increase of computational effort, however if a higher level of robustness is required, the EAIS must be selected, dealing with a larger computational cost.

CHAPTER 4

Passive Distributed Control

In this section the potentialities of the passive flap concept are explored. The purpose is to provide a preliminary analysis of the layout, highlighting the characteristics without ignoring the limits due to feasibility considerations. The chapter is organized as follow. At the beginning, a brief description of the concept is reported in Sect. 4.1. Then the modeling approach is described in Sect. 4.2. A simplified system is adopted to identify the key parameters that define the layout. The description of the tuning of the passive flap is reported, as well as the interaction with the control system. After the theoretical introduction, the results of the analyses are reported in Sect. 4.3. The validated model allows to optimize the flap configuration, achieving the best performance for a stable configuration. The behavior of the passive system is investigated all along the operating range, in time and frequency domain. The effects on the fatigue life and the power production are also estimated. Some considerations about the uncertainty in the aerodynamic properties are reported in Sect. 4.4. Finally the conclusions are stated in Sect. 4.5.

4.1 Definition of the concept

A passive flap system for vibration and load mitigation is investigated. This device is defined by the term passive because it does not require sensors and actuators and it moves only passively in response to blade vibrations. Furthermore, multiple flaps can be installed along the blade span, pursuing the advantages of the distributed active configurations. For these reasons, this concept is situated between the active distributed control systems, such as active flaps installed along blade span, and global control systems, such as pitch actuators or Bend-Twist Coupling (BTC).

A sketch of a control surface, painted in blue, installed on a wind turbine blade is reported in Fig.4.1a. The control surface movement affects the local aerodynamic

load, as reported by the delimited modification of the aerodynamic load distribution, i.e. dashed blue line. The control surface is not connected to actuators and the motion is related to the aeroelastic properties of the system. These characteristics are briefly reported in Fig.4.1b, that reveals in advance the main parameters studied in the next sections. Although a detailed description of all parameters is provided in Sect.4.2, with a technical drawing of the model, it is useful to highlight the fundamental characteristics of the passive flap configuration. The motion of the passive flap is determined by the combination of lumped stiffness k_δ and the mass and inertia of the flap, m_f and J_f, that determines the structural modal frequency. This frequency has to be tuned by considering the modal properties of the overall wind turbine to avoid unwanted dynamic couplings. The center of mass, i.e. the position of m_f, can lie in the control surface but also in front of it to ensure the required behavior. The lumped damper c_δ attenuates the deflection and it has to be design to maximize the performance. Looking at Fig.4.1b, it can be noticed that the leading edge of the control surface overhangs the position of the hinge. This parameter is crucial because it allows to reduce aerodynamic hinge moment, decoupling the aerodynamic moment applied on the flap and the flap motion. These details, as well as the other symbols in Fig.4.1b, are clearly investigated in the following sections, where simplified models are applied to support the statements here reported.

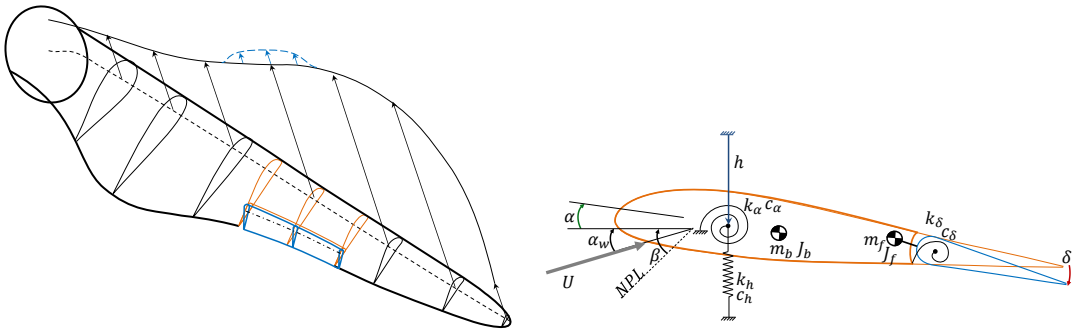

(a) *Passive flap installed on a blade* **(b)** *Conceptual model of passive flap*

Figure 4.1: *Conceptual sketch of passive flap configuration*

Notice that the present study focuses on the preliminary investigation of the passive flap idea applied to a wind turbine. The current approach tries to find out the potentialities of the concept, without aiming at an all-comprehensive investigation. For this reason, various hypotheses are made to simplify the analysis and the interpretation of the results. Despite simplified models are applied, it should be remembered that the passive flap configuration is a general concept that is not related to the modeling approach. If the results are promising, additional studies will be performed in a general simulation environment, removing the simplifying assumptions herein adopted.

Even if this chapter considers only the conceptual design of this element, the passive flap extends the potentialities of the design procedures, providing further parameters to the analyst. Since the passive flaps influence the loads acting on the rotor blades, the performance is maximized if the appended devices and the blade structure are designed by a monolithic approach, seeking the minimum CoE. Therefore, if the passive flap exhibits good properties, its design will be included in a more general context of wind

turbine optimization.

4.2 Simplified modeling approach

In this preliminary analysis a 2D sectional model of the DTU 10MW RWT blade is studied [92]. The span-wise position of the typical section model is considered at 75% of the blade span, [94]. This assumption simplifies the evaluation of the aeroelastic properties, focusing on the sectional effects. A sketch of the blade section with the flap is shown in Fig. 4.2.

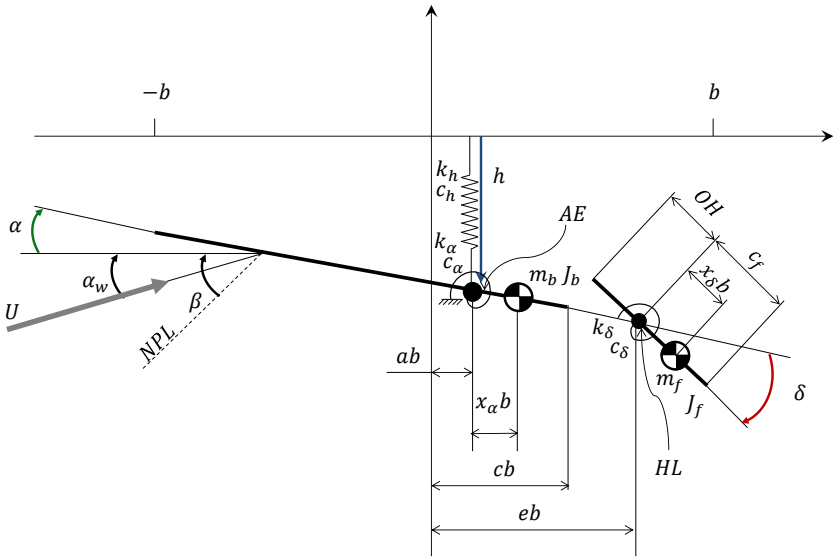

Figure 4.2: *Blade typical section model*

The structural properties are described by lumped parameters obtained by modal condensation of the overall blade model. In the current study, three degrees of freedom are considered:

- h: the plunge, i.e. the vertical deflection of the 2D section measured at the Elastic Axis (EA) of the blade;
- α: the torsional rotation of the 2D section about the EA;
- δ: the rotation of the flap at the Hinge Line (HL);

Looking at Fig. 4.2, α_w is the fluctuation of the angle of attack due to the turbulence, β is the pitch angle, measured from the Null-Pitch-Line (NPL). U is the magnitude of the relative wind speed, that takes into account all the aerodynamic effects on the section of the blade.

The springs K_h, K_α and K_δ represent respectively the plunge, the torsional and the flap stiffness. Similarly, C_h and C_α represent the plunge and torsional damping, while C_δ is a damper at the flap hinge. Finally, m_b and m_f are the sectional blade and flap masses and J_b and J_f the moments of inertia.

The chord of the flap c_f is measured from the HL to the Trailing Edge (TE) of the airfoil. The distance between the HL and the Leading Edge (LE) of the flap is defined OverHang (OH). The other geometric distances are defined as fraction of the semi-chord of the airfoil b.

The aerodynamic loads are evaluated by the unsteady strip theory, including the apparent mass contributions as well as the effects of wake vorticity. Considering the small disturbance assumption, the inviscid and incompressible flow hypotheses, a closed form solution can be determined in the frequency domain by Theodorsen approach. This could be considered the traditional approach to assess the flutter boundaries for a typical section [95]. An equivalent time domain approach is achieved by considering the Duhamel integral of Wagner step response. The indicial response leads to a Linear Time Invariant (LTI) state space model that can handle arbitrary motion [96]. Therefore this approach will be preferred to evaluate the performance of the passive flap along the operative range.

4.2.1 Formulation of the simplified model

In this preliminary analysis, two methods are considered to study the passive flap problem. The first one is the approach of Theodorsen in frequency domain [95, 97]. The aerodynamic model is combined with structural one as described by the following system:

$$\left(M_S s^2 + C_S s + K_S\right) \left\{ \begin{array}{c} h(s)/b \\ \alpha(s) \\ \delta(s) \end{array} \right\} = qA(s') \left\{ \begin{array}{c} h(s)/b \\ \alpha(s) \\ \delta(s) \end{array} \right\} \tag{4.1}$$

where M_S , C_S and K_S in the left hand side represent respectively the mass, the damping and the stiffness matrices. The right hand side represent the aerodynamic forces. The dynamic pressure is q while the aerodynamic matrix is specified by A:

$$A(s') = 2b^2 \left(M_{nc} s'^2 + \left(C_{nc} + C(s') R_1 S_2\right) s' + K_{nc} + C(s') R_1 S_1\right) \tag{4.2}$$

where M_{nc}, C_{nc}, K_{nc} are the non-circulatory mass, damping and stiffness matrices while the products $R_1 S_2$ and $R_1 S_1$ define the circulatory terms. The complex Theodorsen lift-deficiency function is $C(s')$, where the reduced frequency s' is:

$$s' = s\frac{b}{U} \tag{4.3}$$

The time domain model exploits the indicial response approach and it provides the state-space representation reported in Eq. (4.4):

$$M_S \left\{ \begin{array}{c} \ddot{h}(t)/b \\ \ddot{\alpha}(t) \\ \ddot{\delta}(t) \end{array} \right\} + C_S \left\{ \begin{array}{c} \dot{h}(t)/b \\ \dot{\alpha}(t) \\ \dot{\delta}(t) \end{array} \right\} + K_S \left\{ \begin{array}{c} h(t)/b \\ \alpha(t) \\ \delta(t) \end{array} \right\} = 2qb^2 \left\{ \begin{array}{c} -C_L^{NC} - C_L^C - C_L^G \\ C_M^{NC} + C_M^C + C_M^G \\ C_H^{NC} + C_H^C + C_H^G \end{array} \right\} \tag{4.4}$$

where the superscript ^{NC} of the aerodynamic coefficients identifies the non-circulatory terms, ^{C} refers to the circulatory terms and ^{G} are related to the turbulent fluctuations of the wind speed. The non-circulatory terms can be written in matrix form and correspond to the matrixes M_{nc}, C_{nc}, K_{nc} in Eq. 4.2. The circulatory terms are defined as:

$$C_L^C = C_{L_{/\alpha}} \alpha^C + C_{L_{/\delta}} \delta^C \tag{4.5}$$

$$C_M^C = \left(a + \frac{1}{2}\right) C_L^C \tag{4.6}$$

$$C_H^C = C_{H_{/\alpha}} \alpha^C + C_{H_{/\delta}} \delta^C \tag{4.7}$$

$$\tag{4.8}$$

where the angles α^C and δ^C are obtained by the following equations:

$$\alpha^C = \left[\alpha_{QS}\,(0)\,\varphi\,(\tau) + \int_0^\tau \frac{d\alpha_{QS}\,(\sigma)}{d\sigma}\varphi\,(\tau-\sigma)\,d\sigma\right] \tag{4.9}$$

$$\delta^C = \left[\delta_{QS}\,(0)\,\varphi\,(\tau) + \int_0^\tau \frac{d\delta_{QS}\,(\sigma)}{d\sigma}\varphi\,(\tau-\sigma)\,d\sigma\right] \tag{4.10}$$

$$\tag{4.11}$$

$C_{L/*}$ and $C_{H,/*}$ represent the first derivative of the lift and hinge moment coefficient functions towards the generic parameters $*$, i.e. the angle of attack or the flap deflection. The nondimensional distance between the elastic axis and the half chord of the section is a, as reported in Fig. 4.2, while $\tau = tU/b$ is traveled distance, expressed in semi-chord b. The $\varphi(t)$ is the R.T. Jones approximation of the Wagner function, [96], while the quasi-steady (QS) angles are:

$$\alpha_{QS} = U\alpha + \frac{\dot{h}}{b} + b\left(\frac{1}{2} - e\right)\dot{\alpha} \tag{4.12}$$

$$\delta_{QS} = \frac{U}{\pi}\left(T_{10} - LT_{21}\right)\delta + \frac{b}{2\pi}\left(T_{11} - 2LT_{10}\right)\dot{\delta} \tag{4.13}$$

where the coefficients T_i depend on the geometrical configuration [97], e is defined in Fig. 4.2 and $L = e - c$.

This model reproduces the unsteady aerodynamic effects due to an arbitrary motion of the 2D section. In a similar way, aerodynamics generated by a vertical speed variation can be described with the Küssner function, adding a contribution related to the forcing term [96]. The contributions due to the gust can be expressed as:

$$C_L^G = C_{L_{/\alpha}} \alpha^G \tag{4.14}$$

$$C_M^G = \left(a + \frac{1}{2}\right) C_L^G \tag{4.15}$$

$$C_H^G = C_{H_{/\alpha}} \tilde{\alpha}^G \tag{4.16}$$

where the α^G is expressed by the Duhamel integral of the approximation of the Küssner function ψ [98]:

$$\alpha^G = \left[\alpha_{QS_G}(0)\,\psi(\tau) + \int_0^\tau \frac{d\alpha_w(\sigma)}{d\sigma}\psi(\tau-\sigma)\,d\sigma \right] \tag{4.17}$$

while $\tilde{\alpha}^G$ is obtained by an approximation reported by [98]. The Duhamel integrals are solved by state space realization. After mathematical manipulation, the system model can be reduced in a LTI Multi-Input Multi-Output (MIMO) system:

$$\dot{\boldsymbol{x}} = \boldsymbol{A}\boldsymbol{x} + \boldsymbol{B}\boldsymbol{u} \tag{4.18}$$

being $\boldsymbol{x}$ the state vector, containing the structural and the aerodynamic states. The structural degrees of freedom include the plunge displacement, the torsional rotation, the flap rotation and their first derivatives in time. The aerodynamic states are related to the indicial response, including the approximation of the Wagner function and the approximation of the Küssner function for unsteady loads. The input vector $\boldsymbol{u}$ contains the tubulent fluctuations of the angle of attack and the collective-pitch control input. Starting from the state-space formulation of the system, the performance of the passive flap are evaluated by numerical simulations.

4.2.2 Tuning procedure

The tuning process of the passive flap is fundamental because it determines the interaction between the appended device and the rotor blades. In this procedure, the attention should be focused on the aeroelastic properties of the system, considering the structural and the aerodynamic couplings due to the blade motion and to the boundary conditions. Since the properties of the flap are constant, a satisfactory performance should be achieved on the entire operative range. Therefore, a global measurement of the flap behavior must be defined to compare different settings.

The DEL of the plunge displacement of the typical section is considered as an indicator of the flapping motion of the entire blade and on the related bending moment. Since the flapping moment is strictly related to the fatigue life of the blade, a reduction of the plunge displacement of the typical section is interpreted as an increase of the fatigue life of the blade. Furthermore, the DEL is a global parameter that considers all the operative conditions of the wind turbine. For these reasons, the performance of the passive flap are maximized by a tuning that minimizes the DEL of the plunge displacement.

The DEL is estimated by the model of Eq. (4.18). The inputs are evaluated by high fidelity `Cp-Lambda` simulations, considering a complete wind turbine without passive flaps. By this approach, the fluctuations of the angle of attack, due to the turbulent flow and the variations of the pitch angle imposed by the controller, are evaluated including the aeroservoelastic effects that influence the real wind turbine. It is supposed that the time histories of the inputs are also representative of a configuration with passive flaps. This assumption is due to the small magnitude of the perturbations introduced by the passive flaps. Obviously the performance of the overall system can be evaluated only by a fully coupled aeroservoelastic simulations. The current simplification aims at the identification of the important parameters involved into the tuning process and it will be removed in the future.

The time histories of the plunge motion are evaluated by the typical section model to compute the DEL. All the operative range is considered, evaluating the turbulent inputs from the DLC1.1 at different values of mean wind speed at hub height [50]. Assuming the annual wind distribution in terms of Weibull probability function, the DEL of the entire operative range for the plunge motion is evaluated by the procedure explained in [56].

Since the aeroelastic properties of the model are dependent on wind speed, the stability of the optimal configuration must be ensured. This implies that the layout must not exhibit flutter and divergence in the operative range. Considering the classical LTI theory, the stability is achieved if the real part of the eigenvalues of the state matrix $\boldsymbol{A}$ is negative. This requirement is fulfilled by imposing some conditions on the structural and aerodynamic properties of the system. The values of the lumped torsional stiffness and the mass balance of the flap are crucial to achieve a stable condition. Furthermore, it is possible to decrease the magnitude of the hinge moments of the flap, sizing the overhang. This approach reduces the variability of the aeroelastic frequency of the flap deflection toward the wind speed and it can be useful to achieve the desired performance.

Notice that the aerodynamic balance is a parameter useful to reduce the interaction between the passive device and the control system. The standard control activity has to be ensured, therefore the passive flap must not contrast with the pitch actuator. The aerodynamic balance allows to reduce the aerodynamic hinge moment magnitude, decoupling the flap motion and the rotation of the blade about the pitch axis and limiting the noise on the activity of the controller.

In this project the aerodynamic derivatives are estimated by the thin airfoil theory, considering aerodynamic balance [97]. This approach is really simple, allowing the evaluation of the aerodynamic coefficients by analytical equations. The results are usually consistent if the entire airfoil is considered, but a special attention should be paid if a flap is investigated. The aerodynamic derivatives of the flap are strictly related to the local geometry of the joint between the flap and the fixed part of the airfoil and to the effects of the flow viscosity. For these reasons the the results provided by the thin airfoil theory can be considered only as an estimation. During an advanced project phase, a verification of these data will be mandatory by Computational Fluid Dynamic (CFD) techniques or by an experimental setup, defining the real geometry of the system that satisfies the estimated performance.

4.2.3 Interaction with control system

This analysis aims at understanding how the installation of the passive flap affects the AEP, providing a preliminary measurement of the interaction between the appended device and the active control system of the wind turbine. Obviously the tuning procedure of the passive flap tries to minimize the interference with the pitch actuators, as reported in 4.2.2, however this phenomenon can not vanish completely, so an estimation should be provided. A reliable evaluation must consider the trim condition and the behavior of the control system that prescribes the regulation strategy. The 2D linear typical section model does not take into account the control strategy, so it can not assess the effect of the noise introduced by the passive flap. For this reason, the AEP variations are examined by the collective-pitch nonlinear wind turbine reduced model, reported in

Sect. 2.3.5 that includes the controller and rotor dynamic. In this case two additional terms are considered when the aerodynamic thrust F_a and torque T_a are evaluated.

$$T_a = \frac{1}{2}\rho AR\frac{C_P(\lambda,\beta_e,V)}{\lambda}\left(V_w - \dot{d}\right)^2 + T_{a,flap} \tag{4.19}$$

$$F_a = \frac{1}{2}\rho AC_F(\lambda,\beta_e,V)\left(V_w - \dot{d}\right)^2 + F_{a,flap} \tag{4.20}$$

where ρ is the air density, A is the rotor area, R is the rotor radius and λ is the tip speed ratio. The aerodynamic coefficients C_P and C_F are obtained by static `Cp-Lambda` analyses, without considering the passive flap installation. Finally $T_{a,flap}$ and $F_{a,flap}$ are the contributions to aerodynamic forces and moments due to the passive flaps. These contributions are computed by the 2D unsteady sectional model described in Sect. 4.2.1, using the data obtained by `Cp-Lambda` dynamic analyses of a standard blade configuration. Obviously the motion of the passive flaps is influenced by β_c and T_{el_c} imposed by the trim controller. However, it is made the assumption that the aerodynamic forces, obtained by the 2D typical section analyses, are representative of the flap behavior over the entire power production range even if the β_c and T_{el_c} imposed by the trim controller are varied. This hypothesis allows to precompute the flap response for each blade with the typical section model, considering the original time histories for α_w and β obtained by `Cp-Lambda` simulations. By this approach, the time histories of $T_{a,flap}$ and $F_{a,flap}$ are precomputed by the aerodynamic distributed loads otained by the 2D typical section analyses. The aerodynamic distributed loads are assumed constant toward the span-wise extension of the flap. $T_{a,flap}$ and $F_{a,flap}$ are obtained by the superposition of the forces generated by each passive flap, projected into normal and tangent direction to the rotor plane. The pre-calculated effects of the flaps are then applied to nonlinear the reduced model by $T_{a,flap}$ and $F_{a,flap}$ terms, during power production simulations that include the trim controller.

It is possible to simulate the entire operative range, linking the nonlinear wind turbine model with an LQR controller synthetized as reported in [62]. These simulations are compared with the measurements obtained by the reduced system, when the terms $T_{a,flap}$ and $F_{a,flap}$ are switched off, providing a rough estimation of the passive flap effects on the reference conditions and on the AEP. Further developments will include the dynamic of the passive flaps into the nonlinear reduced model, linking the noises $T_{a,flap}$ and $F_{a,flap}$ to the rotor dynamic and to the trim controller.

4.3 Applications and results

In the current section the passive flap performance is investigated. The first analysis aims at validating the model, comparing the results of different implementations. Then the maximization of the performance is considered, focusing on the robustness of the results and the stability of the system. Taking into account the optimal configuration, the behavior of the system is investigated by the frequency response. Then the outputs of the system are evaluated, by considering the the inputs provided by realistic wind turbine simulations. The results in frequency domain and time domain are examined, exploring all the operative range. Finally the effects on DEL and power production are considered.

4.3.1 Procedure validation

In order to validate the procedure, a stability analysis is performed on the typical section by the frequency approach and the time approach reported in Sect. 4.2.1. Considering the system defined in the frequency domain by Eq. (4.1), the p-k iterative method is used to calculate the eigenvalues [99]. On the other side, using the state space representation of the system of Eq. (4.18), a direct calculation of the eigenvalues of the $\boldsymbol{A}$ matrix can be easily performed. These computations are performed for different wind speed values to estimate the variability of the aeroelastic modes toward the wind speed. The parameters used in this preliminary study are not yet optimized, since the model validation is required before the system analysis. Figure 4.3, shows the root loci of the eigenvalues for varying the speed values from 0 to 80 m/s, where the latter bound is obtained by considering a rotor speed of 1.2 times the rated value.

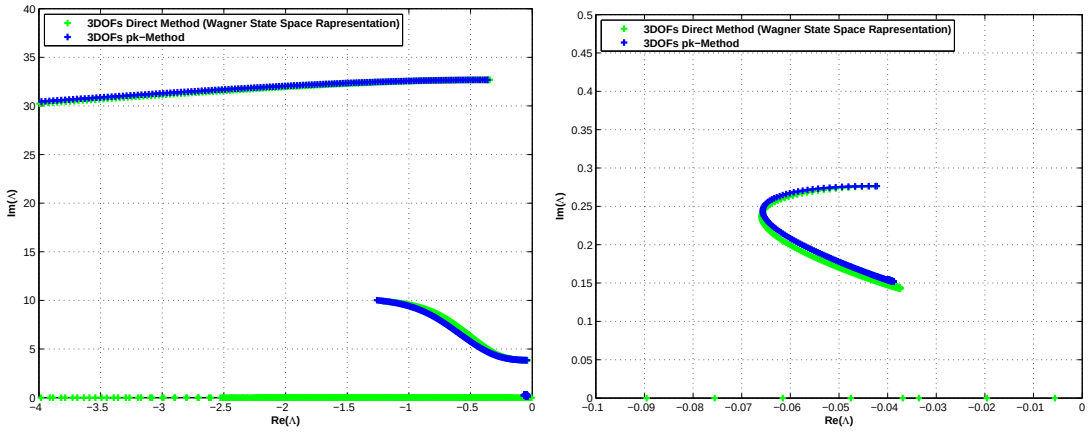

(a) *Torsional mode and plunge mode* **(b)** *Flap deflection mode*

Figure 4.3: *Eigenvalues analysis for procedure validation: plunge and torsional modes (left) and flap deflection mode (right)*

A standard control theory representation is adopted: the abscissas are the real part of the eigenvalues while the ordinates are the imaginary part. The green markers represent the eigenvalues calculated by the direct method with the time domain approach while the blue ones are the eigenvalues obtained by the p-k method. Figure 4.3a displays the torsional and the plunge modes, while the deflection mode of the flap is highlighted on Fig. 4.3b. There is a good agreement between the aeroelastic modes identified by the two approaches. This result and other successful correlations with `MSC Nastran` aeroelastic module provide a reliable validation of the typical section model. Notice that purely real eigenvalues are visible only in the results provided by the time domain approach because they are related to the state space representation of the aerodynamics. Therefore, this difference is due to the modeling approach and it does not affect the verification procedure.

4.3.2 Flap optimization and final configuration

The span-wise position of the passive flap is fixed at 75% of the blade length. This choice aims at a simplification of the analysis and it could be removed in the future.

The blade data at this nondimensional coordinate are reported in Tab. 4.1. The data are obtained by the original configuration of the DTU 10MW RTW [92].

Table 4.1: *Blade data of 2D sectional model*

Parameter	Value
Chord [m]	3.25
Plunge frequency [Hz]	0.62
Torsional frequency [Hz]	4.95
Plunge damping factor [-]	0.01
Torsional damping factor [-]	0.01
Blade mass m_b [Kg/m]	186
Blade moment of inertia J_b [Kg m]	94.1
EA position a	-0.29
Static moment x_α [-]	0.125

To identify the best passive flap configuration, the DEL is evaluated modifying the values of the lumped damper of the flap, the structural modal frequency of the flap and the flap chord length. These analyses show that if the flap chord is reduced, the effectiveness of the flap is also decreased, that results in a low DEL reduction. Furthermore, if the flap chord-wise extension is too short, the installation can be difficult due to the reduced thickness of the airfoil blade at the trailing edge region. On the other hand, the passive system is more effective with higher values of flap chord. The best performance is achieved by imposing the flap chord equal to 8% or 10% of the chord of the overall section. Figure 4.4 reports the contours of the DEL percent reduction, fixing the flap chord value and varying the other parameters.

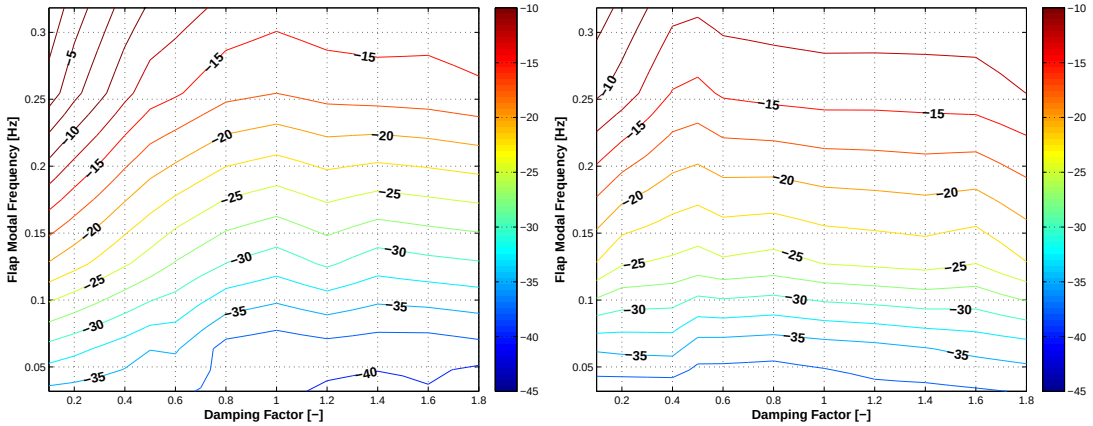

(a) *Flap chord 8% of airfoil chord* **(b)** *Flap chord 10% of airfoil chord*

Figure 4.4: *DEL percent reduction of the system with flap toward the system without flap.*

Looking at the value of flap modal frequency, a common trend is identified in both diagrams: a consistent reduction of the DEL is visible if this value is reduced. However the stability requirement imposes a lower bound to this value, so a good trade-off is achieved by setting the flap modal frequency to 0.032 Hz.

Examining the effects of the flap damping factor, the best results are obtained by

considering a nondimensional damping value higher than unit value and a flap chord of 8% of the airfoil chord. Despite this is the best achievable performance, a more robust configuration is considered by setting the flap chord equal to 10% of the airfoil chord and a damping factor equal to 0.5. This configuration limits the damping required and it is characterized by a smooth area on the DEL reduction surface. The tuned parameters are reported in Tab.4.2, while the allowable flap deflections are shown by the picture nearby.

Table 4.2: *Passive flap configuration (left) and geometric boundaries of the flap motion (right)*

Parameter	Value
Chord c_f [m]	0.32
Modal frequency [Hz]	0.032
Damping factor [-]	0.50
Mass m_f [Kg/m]	5.6
Static moment x_δ [-]	-0.16
Moment of inertia J_f [Kg m]	2.02
Overhang OH/c_f [-]	0.32

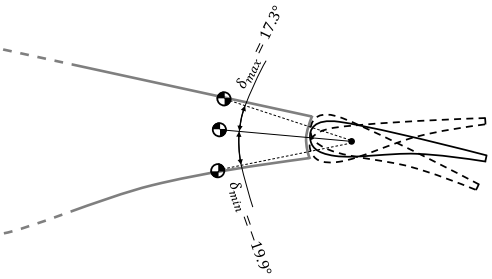

4.3.3 Stability analysis

The the stability analysis for the optimized configuration is performed by the state space model. The root loci is reported in Fig.4.5, considering a variation of the wind speed from 0 to 80 m/s. In this analysis, the regulation trajectory of the wind turbine has been considered. For each wind speed, the corresponding reference conditions have been taken into account, including the blade centrifugal stiffening due to rotor speed. The analysis highlights that the system is always stable within the velocity range considered.

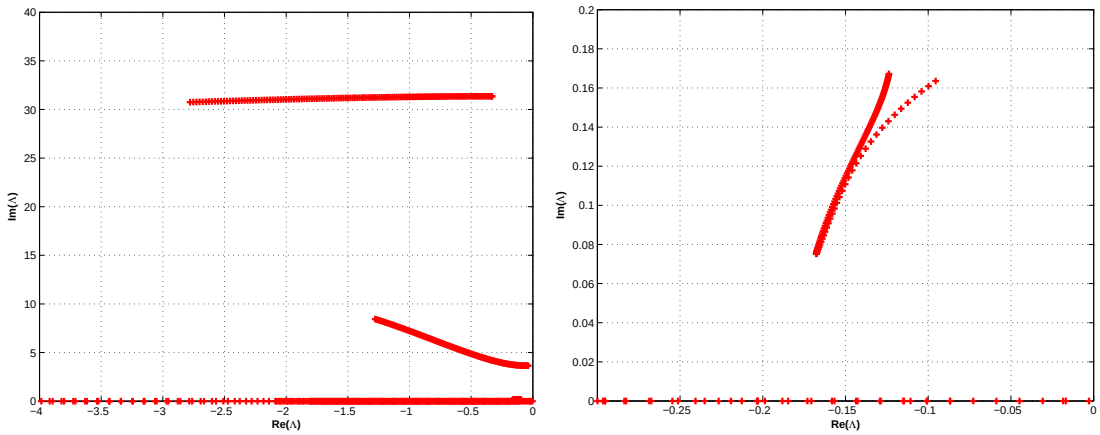

(a) *Torsional mode and plunge mode* **(b)** *Flap deflection mode*

Figure 4.5: *Stability analysis for the optimized configuration. The centrifugal stiffening effect is included.*

4.3.4 Transfer functions analysis

The transfer functions of the state variables with respect to the turbulent fluctuations are computed by Fourier transform of Eq. 4.18. Figure 4.6 shows a transfer function at a value of the hub wind speed close to the rated one.

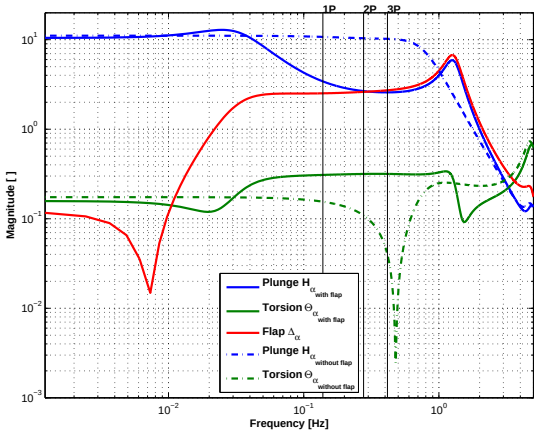

Figure 4.6: *Transfer function at mean hub wind speed of 11 m/s*

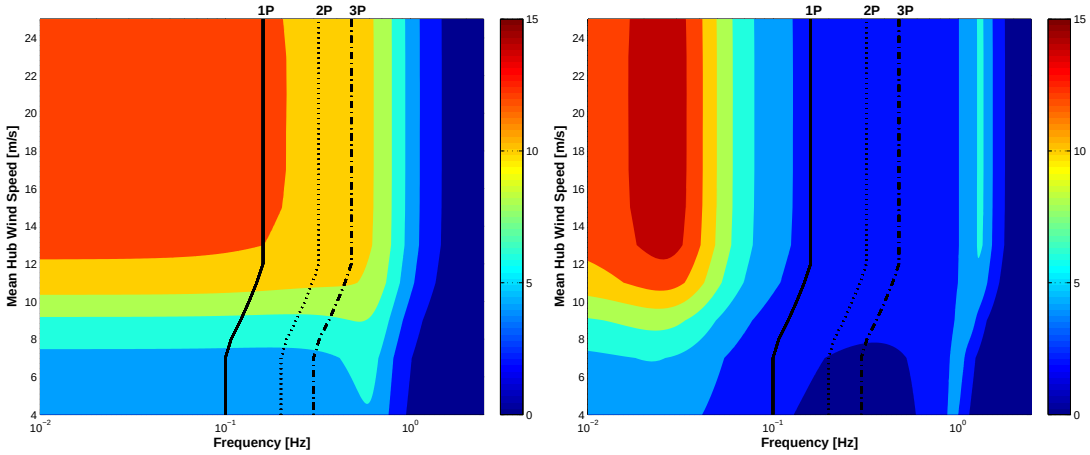

(a) *2D section without passive flap* **(b)** *2D section with passive flap*

Figure 4.7: *Transfer functions between the turbulent fluctuation and plunge motion*

The transfer functions of the system with passive flap are reported by solid lines, while the system without flap is represented by dash-dotted lines. The blue lines represent the plunge motion, the green lines are the torsional motion and the red curve is the rotation of the flap. Looking at the the blue lines, a reduction of magnitude is due to the passive device in the bandwidth bounded by 1P and 3P. This behavior is reported for all the operative range by representing the frequency response of the plunge motion toward the wind speed, Fig. 4.7. Comparing the results of the system without flap to the results of the system with passive flap, a considerable reduction of the plunge amplitude can be noticed. The flap mode interacts as a notch filter with the plunge mode, splitting the plunge modal frequency of the 2D section in two peaks, one before the 1P

and one after the 3P.

As reported in Sec. 4.2.2, an aerodynamic balance is considered to limit the interaction between the passive flap and the active pitch control system. This is highlight in Fig. 4.6, focusing on the low values of the frequency. The solid lines and the dash-dotted curves are very close and the flap deflection is limited. The responses of the two systems are similar, so the average loads as well as the mean power output are preserved.

4.3.5 Section response analysis

The response of the system is analyzed by considering the turbulent fluctuations and the collective pitch angle time histories computed with `Cp-Lambda`. DLC 1.1 are simulated from the cut-in wind speed of 4m/s to cut-out wind speed of 25m/s, as prescribed by [51], taking into account a wind turbine without appended devices. These simulations provide the input data for the linear system of Eq. (4.18). System responses are evaluated for the typical section with the passive flap and for the clean configuration, in order to estimate the flap effects.

Figure 4.8 shows the system responses for three different values of the mean hub wind speed. The reported conditions are close to the cut-in wind speed, the rated condition and the cut-out status, focusing on the time histories with mean hub wind speed of 5 m/s, 11 m/s and 25 m/s.

Fourier Transform (FT) of the plunge response of the system with and without passive flap are reported on the left side. A reduction of the loads is visible when the flap is considered. The time histories of the inputs and the flap rotation are reported on the right. The turbulent fluctuations of the angle of attack and the pitch angle exhibit different trends toward the mean wind speed due to the the regulation policy. Looking at the diagrams that report the time histories of the flap deflection, the black dashed lines represent the limit to the rotation imposed by manufacturing requirements, Fig.4.2. The magnitude of the rotation of the flap achieves very seldom these bounds. In these situation the motion is bounded, providing responses that are compliant to the manufacturing constraints.

4.3.6 Damage equivalent load evaluation

The DEL are evaluated from the system responses, considering the 2D system with and without flap. The aim of these analyses is to estimate the effectiveness of the passive flap on the fatigue damage. Notice that during these calculations, the physical bounds for the flap motion are considered.

The results of DEL calculation are illustrated in Fig. 4.9, where the results of the clean configuration are reported by blue bars, while the passive flap configuration is displayed by red bars. Also in this case the plunge motion is considered as an indicator of the flap bending moment on the overall blade. The histogram on the left reports the DEL evaluated for each wind speed: a considerable reduction is visible along the operative range. The same DEL values multiplied by Weibull probability density function are reported on the right diagram, showing the importance of the operative conditions close to the rated wind speed.

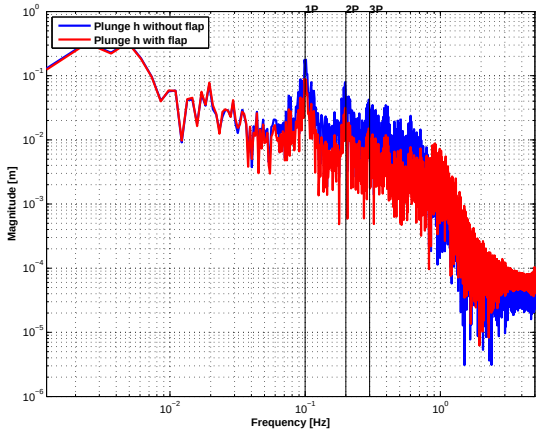

(a) *FT of the plunge response at hub wind speed of 5m/s*

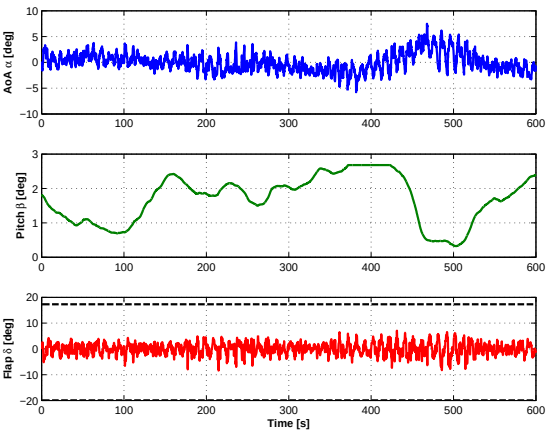

(b) *Time histories of inputs and flap response at 5 m/s*

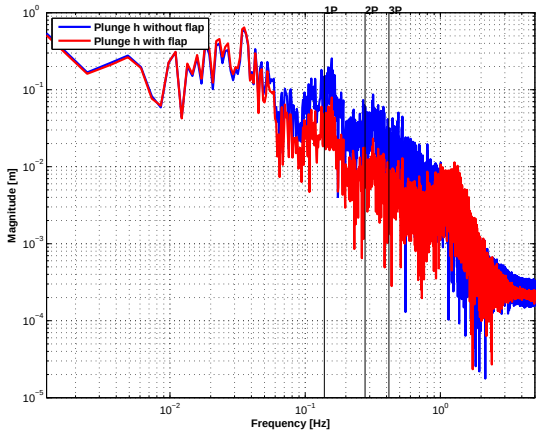

(c) *FT of the plunge response at hub wind speed of 11m/s*

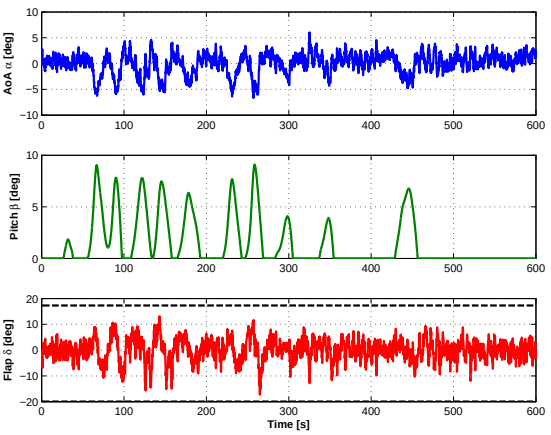

(d) *Time histories of inputs and flap response at 11 m/s*

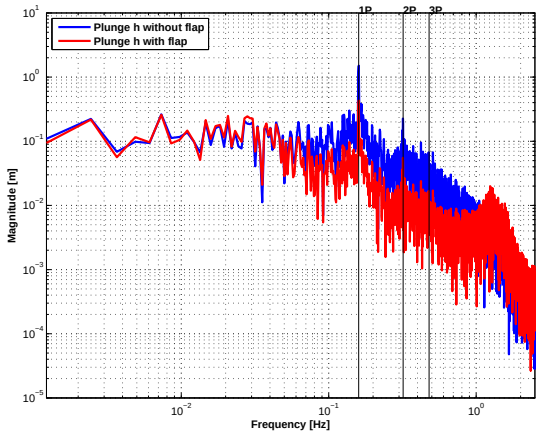

(e) *FT of the plunge response at hub wind speed of 25m/s*

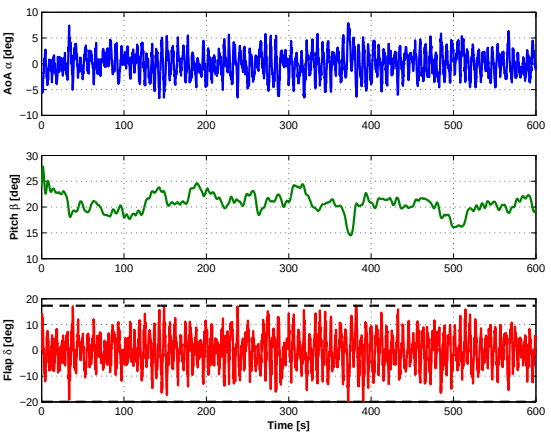

(f) *Time histories of inputs and flap response at 25 m/s*

Figure 4.8: *Analysis of the system responses toward mean hub wind speed*

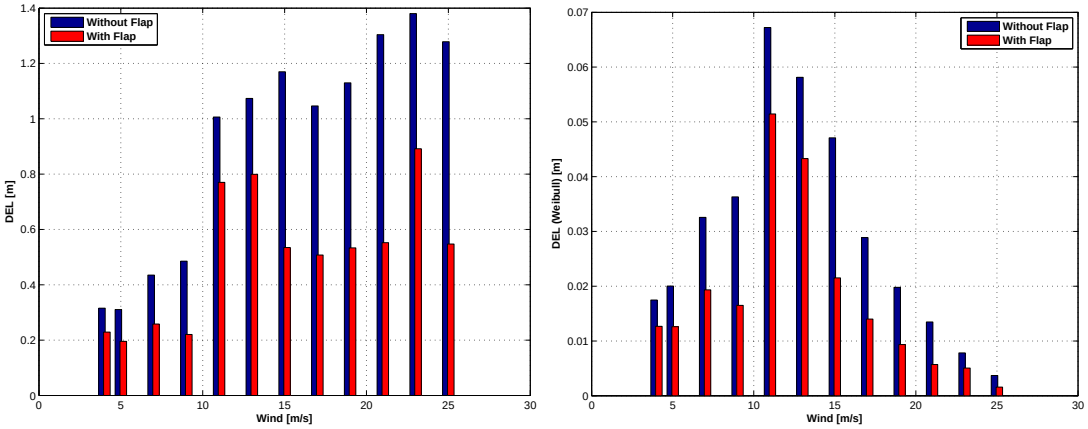

(a) *Damage equivalent loads toward wind speed* **(b)** *Weighted damage equivalent loads toward wind speed*

Figure 4.9: *Damage equivalent loads in plunge direction*

4.3.7 Effects on power production

The effects on power production are estimated by the nonlinear wind turbine reduced model described into Sect. 4.2.3. Normal Turbulence Model (NTM) wind fields with different values of mean hub wind speed are considered. For each wind speed, the dynamic analyses of the system are performed by time domain integration. When the installation of passive flap is taken into account, the pre-computed noises $T_{a,flap}$ and $F_{a,flap}$ are considered accordingly. The dynamic simulations explore all the power production range, allowing to assess the variation of AEP due to the noise induced by the passive flap. The results of these analyses are reported in Fig. 4.10, where the mean value of the electrical power is reported towards mean hub wind speed. This estimation predicts a slight reduction of the power when the passive flaps are considered.

The reduction of the power is reflected also into AEP evaluation as shown by Tab. 4.3, in which the AEP values, in turbulent condition with and without passive flaps, are reported. This analysis shows a limited per cent variation of AEP, but a further validation with a complete model is worthiness.

Table 4.3: *AEP evaluation with and without passive flap by nonlinear wind turbine reduced model*

Reference model	Passive flap model	Per cent variation
47.54 GWh/year	47.38 GWh/year	-0.33%

4.4 Uncertainty in aerodynamic properties

The potentialities of the passive flap configuration are investigated by thin airfoil theory. This is a useful approximation because it provides a fast estimation of the aerodynamic properties of the typical section model. Obviously, the real configuration is different, so a preliminary estimation of the uncertainty that affects the static and dynamic aerodynamic data should be provided.

The static aerodynamics is considered at first, focusing on the most critical element:

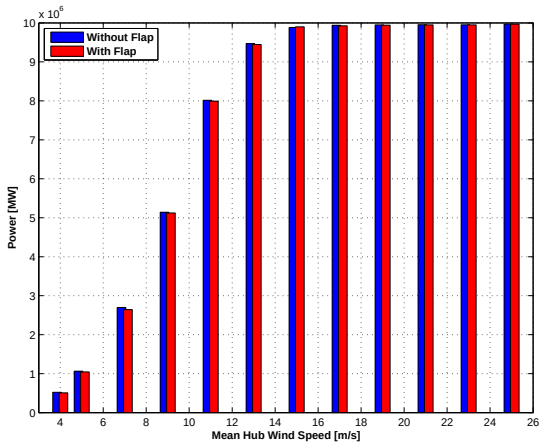

Figure 4.10: *Power production in turbulent wind conditions: standard configuration vs passive flap configuration*

the hinge moment coefficient. The importance of this analysis is magnified by the aerodynamic balance that is introduced to decoupling the flap motion and the aerodynamic hinge moment. Different methods are available to estimate the effect produced by the aerodynamic balance, among these, the empirical method is considered at first. This technique provides a fast estimation of the flap overhang effects by an interpolation of experimental data.

Figure 4.12 compares the estimation of the variability on the hinge moment coefficients provided by the thin airfoil theory with the experimental data from [100]. The ratio of the aerodynamic derivative with and without aerodynamic balance is reported in ordinate, while the balance ratio is reported in abscissa. Following the nomenclature of Fig. 4.11, the balance ratio is defined as:

$$BalanceRatio = \left[\left(\frac{c_b}{c_f}\right)^2 - \left(\frac{t_h}{2c_f}\right)^2\right]^2$$

Considering the thin airfoil theory, the balance ratio is computed by imposing the thickness t_h equal to zero.

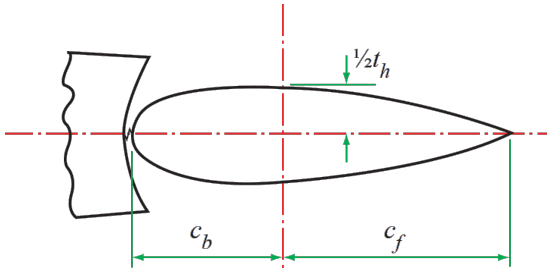

Figure 4.11: *ESDU nomenclature to estimate aerodynamic balance effects (source [100])*

The mean trend is correctly estimated by the thin airfoil theory, however the experimental data exhibit a scatter due to various effects. The dispersion of the data is encompassed by an uncertainty of 0.1 at low balance ratio and of 0.3 at high balance ratio. Notice that the tested airfoils have a thickness value that is lower than the one of

the airfoils for wind energy applications. Moreover, the variability of the experimental data due to the shape of the leading edge of the control surface is undeniable. For these reasons, the estimation of the hinge moment coefficients should be related to a detailed aerodynamic design. This is unacceptable during preliminary design because it requires expensive computations or wind tunnel test. Nevertheless a detailed verification has to be performed in an advanced phase of the project, if a mismatch is identified, suitable corrections can be applied to the original configuration.

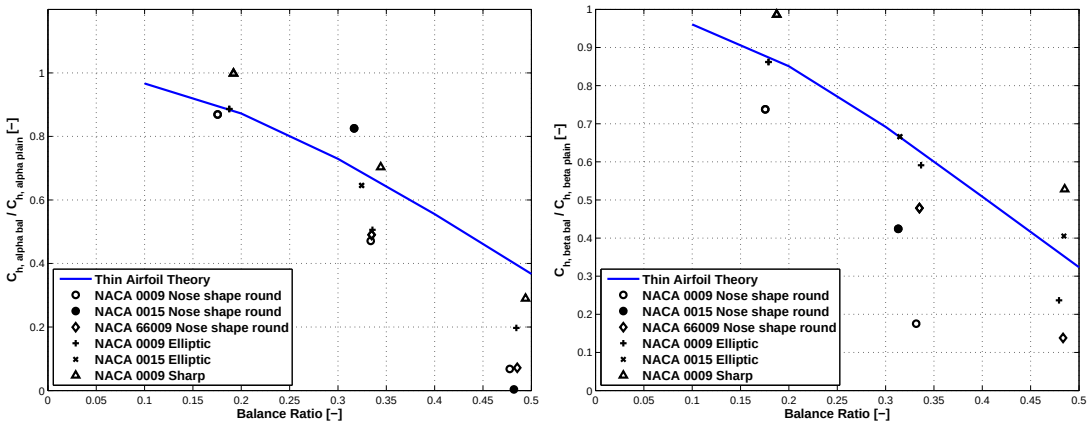

(a) *Effects on hinge moment derivative vs angle of attack* **(b)** *Effects on hinge moment derivative vs flap deflection*

Figure 4.12: *Variation of the hinge moment coeffcient due to aerodynamic balance: comparison of thin airfoil theory with ESDU data [100]*

The limits of the empirical methods can be overcome by CFD analyses. An applicative aeronautical example of this evaluation can be found in Fig. 4.13, from [101]. The contour and the stream lines show the complexity of the flow field, highlighting the critical aspects of numerical computation. To achieve a reliable result, this evaluation has to consider the viscosity of the fluid and the accurate prediction of flow separation, as reported by [102]. The high computational cost and the complexity of these analyses are mainly related to these requirements, allowing the CFD application in an advance project phase. Notice that the hinge moment coefficients can be also measured by wind tunnel tests. Usually, these are validations of CFD results, therefore this approach is considered unfeasible for a preliminary study.

Considering the time varying behavior of the aerodynamic forces, the estimation of the indicial response is fundamental to obtain a reliable result. R.T. Jones approximation of the Wagner function provides a result coherent with thin airfoil theory. However, it turns out to be a good results also for airfoils with finite thickness, as reported in [103]. A correction of the indicial response related to the thickness of the airfoil value turns out to be optional and it is not applied.

Another dynamic approximation is related to upwash caused by gust, that is considered chord-wise constant for the evaluation of the hinge moment. This approximation allows to apply also in this case the R.T. Jones expression of Wagner function. The small values, much less than unity, of the reduced frequency involved in the current project allow to adopt this approximation, producing a negligible error of the flap dynamic response [98].

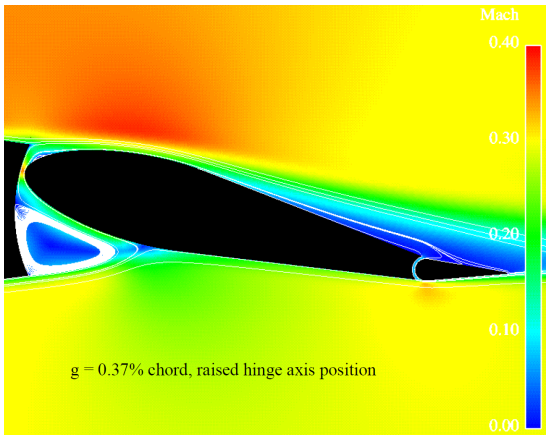

Figure 4.13: *CFD analysis of aerodynamically balanced flap: Mach number contour and stream lines (source [101])*

These considerations allow to neglect the uncertainty related to the time varying aerodynamic properties during this preliminary assessment of the passive flap. Obviously a validation has to be performed by advanced numerical models, for example multibody approach coupled to CFD techniques, or by experimental test in a controller environment, such as wind tunnel.

The difficulties related to the modeling of a balanced control surface are briefly analyzed in the current section. Despite the multiple sources of uncertainty of the aerodynamic properties, the modeling approach is considered suitable for the preliminary analyses here reported. Since the passive flap configuration has shown interesting results, further resources will be invested in the future to achieve a better estimation of the aerodynamic data and to increase the reliability of the model.

4.5 Conclusions

In this section, a passive flap system for load mitigation has been investigated. The advantage of this technique is that it does not require sensors and actuators because it is moved passively by blade vibrations.

In this preliminary analysis, a typical section of the DTU 10MW RTW blade is considered and two simplified models are developed. The first one is expressed in frequency domain by the classical Theodorsen theory, while the second one is developed in the time domain by the indicial response method. The simplified approach is validated by comparing the results provided by the two formulations and it is applied to evaluate the potentialities of the passive flap concept.

The input data are provided by `Cp-Lambda` analyses, performed on an aeroservoelastic model of a complete wind turbine without flaps. Considering these boundary conditions, an optimization of the layout is performed, tuning the passive flap to obtain a stable configuration that minimizes the DEL of a measurement related to the flap bending moment of the entire blade.

The performance of the optimal configuration is studied, comparing the results given by the typical section with the passive flap or by the plain configuration. The transfer functions are examined at first, highlighting the conditions where the effectiveness of

the flap is maximized. Then the responses of the section in turbulent conditions are taken into account, looking at DLC1.1 with different mean hub wind speed. These results are examined in time and frequency domain, showing a good performance on the power production operative region. Moreover the time histories show a remarkable reduction of DEL when the passive flap is installed. The effect of passive flap on AEP has been estimated by the nonlinear wind turbine reduced model. NTM wind fields with different values of mean hub wind speed are considered. The loss of AEP is limited, but it is necessary to remove the simplifying hypotheses to increase the reliability of this result. Finally the main sources of uncertainty of the aerodynamic properties are listed, examining the critical approximations of the simplified model.

In conclusions the potentialities of the passive flap concept have been highlighted in the current section. However, further investigation of the effects on the CoE variations should be made in order to point out if it would be a successful technology.

CHAPTER 5

Conclusions

5.1 Concluding Remarks

In the current work a general approach to the aero-structural design of wind turbines is presented. The classical layout and the innovative concepts are taken into account. The maximization of the performance is investigated, preserving the reliability requirement that appears to be fundamental in wind energy systems. Different methods are merged in a tool that is able to support an experienced analyst during various phase of aero-structural design. The developed framework can be successfully employed in different tasks: design of new configurations, refinement of existing wind turbines, trade studies and sensitivity analyses.

The aero-structural design procedures are presented in Chap. 2, providing a detailed description of the developed methods. The attention is focused on the aeroelastic properties of the rotor blades and on the structural properties of the support tower. These components are considered the most important aero-structural elements because their characteristics contribute significantly to the definition of the CoE.

All the procedures rely on a common aeroservoelastic simulation environment that allows to evaluate the required measurements. General analysis methodologies are considered in each phase of the design, including into the sizing process and into the requirement evaluations all the fundamental effects. Furthermore, at the end of design process, the complete model of the wind turbine is automatically available, allowing the calculation of different conditions to verify the solution or to design different sub-components.

Initially the multidisciplinary optimization problem is divided in mono-disciplinary optimizations. This approach reduces the computational time and it provides independent software apt to conduct aerodynamic or structural sizing of the wind turbine components. Furthermore this simplification is required to understand the pros and cons of

the various design approaches. When the single modules are explored, the unification of the procedures into aero-structural optimization is performed.

5.1.1 Aerodynamic optimal design

The aerodynamic optimization is considered at first. This technique follows a well known approach an it is reported for completeness. The maximization of the AEP is achieved by optimizing the chord and twist distribution along the blade span. A general description of the optimization algorithm is provided, highlighting the pseudo-code representation and the model parametrization. The requirements of the final configuration are included by a set of constraint equations. The evaluation of the AEP is performed by considering the real regulation policy on the entire operative range. The regulation trajectory is computed by the aerodynamic characteristics of the complete wind turbine that are provided by an aeroelastic model.

5.1.2 Structural optimal design

The optimal structural design of the rotor blades and the tower is investigated. This coupled methodology is developed in the current thesis, starting from a tool able to optimize the sole blade. Moreover the original parametrization of the blade structure is extended by the inclusion of the root reinforcement and the third web components. A further improvement regards the merit figure that is identified by a CoE model, discarding the original measurement of the structural performance: the blade mass. This choice allows to evaluate the sensitivity of each variable on the global configuration of the wind turbine. The CoE model merges the different contributions in a unique value, allowing the application of the mono-objective optimization techniques. Obviously the code permits the structural optimization of the single components. However, if the maximum performance is desired, the design should consider the couplings between these elements due to the requirements, such as blade-tower clearance. The structural optimization algorithm involves a multi-level description of the components. The optimal design is performed at coarse-level that relies on efficient structural models, allowing fast evaluation of the merit figure and of the constraints. When an optimal configuration is achieved, a refinement analysis at fine-level can be performed.

The coarse-level analyses are based on a nonlinear geometrically exact beam formulation that is able to take into account all the couplings due to orthotropic materials. The beam properties and the stress/strain fields are evaluated by sectional analyses based on anisotropic beam theory. This approach allows to evaluate all quantities required by the optimization with a limited computational cost. The design procedure is base on the automatic management of the simulations and the data processing. The dynamic load cases, the Campbell diagram, the regulation policy and the tuning of control laws are only some examples of the simulation capabilities. The fundamental measurements and the model updating required by the optimization routines are obtained without user's participation in a fully automatic way. This is a primary characteristic of the proposed approach, involving code developing and correct technical choices. Also in structural optimization the design requirements are included by a set of constrain equations. Constraints related to strength of the structural configuration are introduced, involving ultimate loads, fatigue damage, buckling requirement, modal properties and blade-tower

clearance. Moreover manufacturing requirements allows to generate a feasible configuration. The main idea, that drives this approach, is that only an a priori inclusion can consider the intrinsic interactions and can allow to avoid an a posteriori correction activity. Obviously the procedure can be extended easily by incorporating further requirements that have been here neglected.

5.1.3 Refinement analysis

The refinement level is developed entirely during the current project, focusing on the entire blade and on the detailed analysis. The fine verifications involve the structural properties of the blade so they can be performed after structural or aero-structural optimization. The fine-level analysis is based on the automatic generation of 3D FEM from a detailed 3D NURBS-based CAD model. All the principal constitutive components are modeled by either shell or solid elements. The meshing procedure is automatic as well as the association of the properties for anisotropic composite layered materials and loading conditions from the multibody aero-servo-elastic analyses. Complete reanalysis of the entire blade is performed at fine 3D FE description level. All the requirements are evaluated, considering the constraints included at coarse-level. If some of the requirements are not satisfied, heuristic corrections are applied at coarse-level by updating the design constraints considering the amount of violation. The loop closure is performed iteratively between the two modeling layers and it allows to include the effects in the coarse-level optimization. If the resolution of the 3D FEM of the entire blade is not sufficient, the critical blade regions can be magnified by 3D FE local analyses. This approach is similar to the analysis of the entire blade, therefore the local effects can by included into the coarse-level by heuristic scaling of the design requirements.

5.1.4 Aero-structural optimal design

When the mono-disciplinary optimization techniques are validated, the attention is focused on aero-structural design of the rotor blades, fixing the overall wind turbine configuration. Various algorithms are presented and analyzed, showing the pros and cons of each method. In addition to the reciprocal validation, this approach supplies different methodologies that can be tailored to the analyst's needs.

The first algorithm is defined as Pre-Assumed Aerodynamic Shape (PAAS) method, it was released before this thesis and it is usefully applied to validate the new approaches developed during the current project: EAIS and MLU algorithms. PAAS method generates a population of optimal blades that is characterized by relevant aerodynamic macro-parameters chosen by the analyst. Aerodynamic and structural optimizations are applied sequentially, sampling the solution domain. The best solution is obtained by the interpolation on the different designs. This approach is robust and it has a reduced computational cost, but it requires the user's active participation.

The External Aerodynamic/Internal Structure (EAIS) approach overcomes the PAAS method, automating the aerodynamic parametrization of the model. The external optimization routine handles the aerodynamic variables, while the internal optimization function generates the optimal structure for each aerodynamic configuration imposed by the external optimization routine. The analyst's workload is reduced at a price of a higher computational cost.

The Monolithic with Load Updating (MLU) approach unifies the aerodynamic and the structural variables in a monolithic algorithm. The sensitivity of the constraint equations to aerodynamic variables is estimated by simplified models, while an iterative procedure recalibrates the absolute value of the design requirements. The algorithm is faster but less robust than the EAIS approach.

Although the skills of an experienced analyst is irreplaceable when conducting the design of complex engineering systems such as a wind turbine, the proposed highly automated design tools are believed to be able to streamline the design process and help in the exploration of the design space, relieving the burden of the most complex and error-prone tasks and allowing the user to focus on the understanding of the various design trade-offs to come to the best possible solution.

5.1.5 Results and applications

After presenting the optimal design methods, several applications are shown in Chap.3. All the reported examples are developed throughout this thesis to highlight the various aspects of each implemented technique.

The multi-level structural optimization procedure is demonstrated on a 2MW wind turbine. After a first coarse-level optimization, detailed stress and fatigue analyses conducted on the fine-level 3D model reveal significant stress concentrations between the root and the maximum chord regions. These effects are not captured by the coarse-level beam model, which is blind to highly three-dimensional variations and abrupt changes in the stress field. Furthermore, the modal analysis of the 3D model shows the violation of a frequency constraint condition, while the buckling analysis highlights the presence of skin instability under the maximum tip deflection loading condition. By tightening the respective constraint bounds for the subsequent coarse-level iteration, it is shown that convergence can be obtained very rapidly by iterating between the coarse and fine levels.

Then the optimal structural design of a 10MW HAWT is considered. In this case, the estimation of nonstructural mass distribution and the design of the blade root bolted joint are studied. The effects of these details are included into the coarse-level optimization, defining a solution that is compliant to the requirements.

The combined design of the rotor blades and the tower is successfully applied to two different cases: 2MW standard machine and 10MW research configuration. The results of both cases are in good agreement, showing the importance of the blade-tower clearance. This parameter influences the blade and tower structural design, therefore it requires further attention. Considering macro-parameters, that affect the value of the clearance, trend studies are performed to identify the optimal wind turbine layout. The CoE model allows to compare different configurations, identifying the optimal value for rotor cone angle and nacelle uptilt angle of both wind turbines.

Finally, the aero-structural design methods are applied to a conceptual 10MW HAWT test case. A good agreement in term of optimal configurations is identified looking at the results of the various methods. The PAAS approach delimits the position of the optimum, while the EAIS approach and the MLU approach are able to identify the best solution automatically. The consistency of the results verifies the coherence of the assumptions of each aero-structural algorithm, giving a practical proof of convergence of the different methods.

The results from the three approaches show that the aero-structural optimization for the wind turbine configuration used in this project favors a rotor design with higher values of solidity and maximum chord. This allows to meet a higher structural efficiency without depressing significantly the aerodynamic performance. Compared to the Baseline configuration, the aero-structural optimum achieves a reduction of 9.41% of blade mass with a reduction of AEP of 0.16%. This results in CoE savings for 0.33%. These results show that the aero-structural approach allows to obtain the best performances of wind turbine rotor blades, even if the advantage in term of CoE is limited. In order to obtain a more remarkable reduction of CoE, the parameters that define the wind turbine configuration must be included into the design procedure, as suggested by Sect.5.2.

5.1.6 Passive distributed control

The potentialities of the passive flap system for load alleviation are investigated in Chap. 4. Although the aeronautical application of passive aerodynamic appended devices are known, the exploitation in wind energy systems is almost unexplored. Therefore the reported application of this concept can be considered a novel idea at the author's knowledge. Despite the simplicity of the mathematical models, various analyses explore all the fundamental situations encountered in the operative range of the wind turbine. Furthermore the decoupling of the aerodynamic hinge moment and the motion of the flap is achieved by the introduction of the flap overhang. This properties is crucial to avoid an interference with the control system and it is a further innovative contribution of this work.

The studied appended device is moved by the loads due to the motion of the blade, without requiring sensors and actuators. Furthermore, it is a distributed mechanism able to react to local fluctuations of loads applied on each blade. Notice that reliability reduction of the wind turbine due to the flap installation is limited because of the passive nature of this solution.

Preliminary analyses are performed on a 10MW HAWT, developing two simplified models. The first one is a typical section useful to evaluate the response of the system. The second model is a reduced order model of the rotor that allows to estimate the interference between this passive concept and the control system of the wind turbine. The input conditions are provided by an aero-servo-elastic simulation environment, considering the turbulent dynamic simulations of a complete wind turbine without passive flaps.

Initially a tuning procedure is performed, maximizing the reduction of the DEL due to the flap installation. The tuning procedure is fundamental since the effectiveness of the appended device only depends on its aero-structural properties. The stability of the control surface is ensured on the entire operative range. Furthermore, the interference with the pitch control system is minimized by the introduction of an aerodynamic balance to reduce the dependance of the hinge moment derivatives to the angle of attack.

The entire operative range is examined by the simplified models, highlighting the effectiveness of this passive system in load alleviation. The effects on power production are also considered, reporting a limited reduction of 0.4% of the AEP value. Notice that this is a preliminary results that should be validated by all-comprehensive simulations. Finally some considerations about the uncertainty of the aerodynamic properties are reported, focusing on the estimation of the aerodynamic hinge moment coefficients.

5.2 Future Work

Various modifications of the design tool can be considered to improve the implemented procedures. First of all, the sensitivity studies about wind turbine configuration could be enhanced by considering the couplings between the macro-parameters that define the wind turbine layout. This procedure would allow to identify the best trade-off for the design of the blades and tower structure. Furthermore, other structural components can be included into the optimization, as a straightforward generalization of the design method. This procedure mainly influences the initial capital cost, but it has a limited effect on the CoE value.

More interesting results can be achieved if the attention is focused on the optimal sizing of the aero-structural properties of the wind turbine. Looking at the analysis of the aero-structural optimization methods, it can be seen that a slight reduction of CoE is obtained, despite the multidisciplinary approach. In order to get a more remarkable reduction, the parameters that define the wind turbine configuration must be included into the design procedure. For this reason, future developments consider also the data that heavily affect the global wind turbine configuration, such as rotor radius, rotor cone angle, blade pre-bend and nacelle uptilt angle. The coupling between rotor aeroelastic design and tower sizing are also examined, looking for a further reduction of CoE. In this case the tower height should be included to identify the best trade-off in connection with the layout of the rotor assembly.

Another interesting contribution could be the inclusion of the blade airfoils design into the aero-structural optimization. This approach leads to a free-form optimization, in which the entire blade shape ensues from the design. This approach allows the arising of special configurations without any assumptions. An example would be the study of low induction rotors in a general framework, investigating this innovative concept and proving if it would be a successful solution.

To increase the reliability of the results, the cost model that provides the blade cost has to be generalized. Future developments consider specific models that take into account materials, labor content, and equipment of the blade manufacturing process [104]. This analysis aims at removing the assumptions that support the statistical estimation of the blade cost, focusing on the specific case considered by the aero-structural design.

Looking at the passive distributed load alleviation techniques, the promising results have to be validated in a general simulation environment, such as `Cp-Lambda`. This approach removes all the hypotheses and approximations, providing dependable results. Also the aerodynamic data estimated by thin airfoil theory should be validated by considering CFD techniques or experimental setup. Static and dynamic properties of the aerodynamic data have to be investigated to minimize the uncertainty. If these verifications prove to be successful, a further generalization is the inclusion of the passive flap design into the aero-structural optimization procedures. This approach is required by the perturbations due to the passive flap system, regarding the loads and the aeroelastic properties of the rotor. Obviously the best result can be achieved if the design of the standard blade layout is coupled with the appended devices definition. This appears to be the the best way to transform the advantages due to the passive flap installation into a CoE reduction. Notice that also in this case an updating of the blade cost model is

worthiness to consider the structural modifications required by the embedding of the distributed device.

Bibliography

[1] Manwell J.F., McGowan J.G., Rogers A.L. *Wind Energy Explained: Theory, Design and Application*. John Wiley & Sons, 2nd edition, 2009.

[2] Burton T., Jenkins N., Sharpe D., Bossanyi E. *Wind Energy Handbook*. John Wiley & Sons, 2nd edition, 2011.

[3] Ning A., Damiani R., Moriarty P. Objectives and constraints for wind turbine optimization. In *51st AIAA Aerospace Sciences Meeting*, Grapevine, Texas, US, 2013. DOI:10.2514/6.2013-201.

[4] Lee D., Hodges D.H., Patil M.J. Multi-flexible-body dynamic analysis of horizontal axis wind turbines. *Wind Energy*, 5:281–300, 2002. DOI:10.1002/we.66.

[5] Bauchau O.A., Bottasso C.L., Nikishkov Y.G. Modeling rotorcraft dynamics with finite element multibody procedures. *Mathematical and Computer Modelling*, 33:1113–1137, 2001. DOI:10.1016/S0895-7177(00)00303-4.

[6] Bottasso C.L., Croce A. *Cp-Lambda: User's Manual*. Dipartimento di Ingegneria Aerospaziale, Politecnico di Milano, via La Masa 34, 20156, Milano, 2006–2013.

[7] Larsen T.J., Hansen A.M. How 2 HAWC2, the user's manual. Technical Report Risø-R-1597(ver. 3-1)(EN), Risø National Laboratory, Roskilde, Denmark, 2007.

[8] Jonkman J.M., Buhl Jr M.L. FAST user's guide. Technical Report NREL/EL-500-38230, National Renewable Energy Laboratory, Colorado, USA, 2005.

[9] Bladed. GL Garrad Hassan www.gl-garradhassan.com.

[10] RotorOpt perfects rotor design. LM Glasfiber, News Letter, September 2007, p. 5.

[11] Fuglsang L. Integrated design of turbine rotors. In *European Wind Energy Conference & Exhibition EWEC 2008, 31 March – 3 April*, Brussels, Belgium, 2008.

[12] Duineveld N.P. Structure and possibilities of the FOCUS design package. In *Dutch Wind Workshops*, Delft, the Netherlands, 2008. TU Delft.

[13] Jonkman J. NREL structural and aeroelastic codes. In *Wind Turbine Workshop*, Sandia National Laboratories, Albuquerque, NM, USA, 2008.

[14] Bottasso C.L., Campagnolo F., Croce A. Multi-disciplinary constrained optimization of wind turbines. *Multibody System Dynamics*, 27(1):21–53, 2012. DOI:10.1007/s11044-011-9271-x.

[15] Giavotto V., Borri M., Mantegazza P., Ghiringhelli G. Anisotropic beam theory and applications. *Computers & Structures*, 16(1–4):403–413, 1983. DOI:10.1016/0045-7949(83)90179-7.

[16] Bauchau O.A. *Flexible Multibody Dynamics*, volume 176. Springer, solid mechanics and its applications edition, 2011.

[17] Maki K., Sbragio R., Vlahopoulos N. System design of a wind turbine using a multi-level optimization approach. *Renewable Energy*, 43:101–110, 2012. DOI: 10.1016/j.renene.2011.11.027.

[18] Bak C., Zahle .F, Bitsche R., Kim T., Yde A., Henriksen L.C., Hansen M.H., Blasques J.P.A.A., Gaunaa M., Sørensen N.N. Developing the basis for the design of a 10MW lightweight rotor. In *Proceding IQPC Conference - Advances in Rotor Blades for Wind Turbines*, Bremen, Germany, 2013.

[19] Chen J., Quan Wang Q., Shen W.Z., Pang X., Li S., Guo X. Structural optimization study of composite wind turbine blade. *Materials and design*, 46:247–255, 2013. DOI: 10.1016/j.matdes.2012.10.036.

[20] Fischer G.R.. Kipouros T., Savill A.M. Multi-objective optimization of horizontal axis wind turbine structure and energy production using aerofoil and blade properties as design variables. *Renewable Energy*, 62:506–515, 2014. DOI: 10.1016/j.renene.2013.08.009.

[21] Buckney N., Pirrera A., Green S.D., Weaver P.M. Structural efficiency of a wind turbine blade. *Thin Walled Structures*, 67:144–154, 2013. DOI: 10.1016/j.tws.2013.02.010.

[22] Berg J.C., Resor B.R. Numerical Manufacturing And Design Tool (`NuMAD` v2.0) for Wind Turbine Blades: User's Guide. Technical Report SAND2012-7028, Sandia National Laboratories, 2012.

[23] Hoyt D.M., Graesser D. Rapid fea of wind turbine blades – summary of NSE composites' structural analysis capabilities for blade `NSE blademesher` in-house software. Technical report, NSE Composites, 1101 North Northlake Way, Suite 4, Seattle, WA 98103, 2008.

[24] Ashwill T. Sweep-twist adaptive rotor blade: Final project report. Technical Report SAND2009-8037, Sandia National Laboratories, Albuquerque, NM, 2010.

[25] Jureczko M., Pawlak M., Mężyk A. Optimisation of wind turbine blades. *Journal of Materials Processing Technology*, 167:463–471, 2005. DOI:10.1016/j.jmatprotec.2005.06.055.

[26] Tegen S., Lantz E., Hand M., Maples B., Smith A., Schwabe P. 2011 Cost of wind energy review. Technical Report NREL/TP-5000-56266, NREL National Renewable Energy Laboratory, March 2013.

[27] Negm H.M.,Maalawi K.Y. Structural design optimization of wind turbine towers. *Computers and Structures*, 74:649–666, 2000. DOI:.

[28] Uys P.E., Farkas J., Jármai K., van Tonder F. Optimization of a steel tower for a wind turbine structure. *Engineering Structures*, 29:1337–1342, 2007. DOI: 10.1016/j.engstruct.2006.08.011.

[29] Lavassas I., Nikolaidis G., Zervas P., Efthimiou E., Doudoumis I.N., Baniotopoulos C.C. Analysis and design of the prototype of a steel 1MW wind turbine tower. *Engineering Structures*, 25:1097–1106, 2003. DOI: 10.1016/S0141-0296(03)00059-2.

[30] Jiang W., Fan Q., Gong J. Optimization of welding joint between tower and bottom flange based on residual stress considerations in a wind turbine. *Energy*, 35:461–467, 2010. DOI: doi:10.1016/j.energy.2009.10.012.

[31] Zwick D., Muskulus M., Moe G. Iterative optimimization approach for the design of full-height lattice towers for offshore wind turbines. *Energy Procedia*, 24:2012, 297–304. DOI: 10.1016/j.egypro.2012.06.112.

[32] Gutiérrez E., Primi S., Taucer F., Caperan P., Tirelli D., Mieres J., Calvo I., Rodriguez J., Vallano F., Galiotis C., Mouzakis D. A wind turbine tower design based on the use of fibre-reinforced composites. Technical Report Megawind Project, ENK5-CT-2000-00328, European Commission Joint Research Centre, 2003.

[33] Quilligan A., O'Connor A., Pakrashi V. Fragility analysis of steel and concrete wind turbine towers. *Engineering Structures*, 36:270–282, 2012. 10.1016/j.engstruct.2011.12.013.

[34] Bottasso C.L., Croce A., Sartori L., Grasso, F. Free-form design of rotor blades. In *Proceedings of The Science Of Making Torque From Wind*, Copenhagen, June 2014.

[35] Vesel Jr. R.W., McNamara J.J. Performance enhancement and load reduction of a 5MW wind turbine blade. *Renewable Energy*, 66:391–401, 2014. DOI: 10.1016/j.renene.2013.12.019.

[36] Kenway G., Martins J.R.R.A. Aerostructural shape optimization of wind turbine blades considering site-specific winds. In *12th AIAA/ISSMO Multidisciplinary Analysis and Optimization Conference*, Victoria, British Columbia, Canada, September 10th-12th, 2008. DOI: 10.2514/6.2008-6025.

[37] Ashuri T., Zaaijer M.B., Martins J.R.R.A., van Bussel G.J.W., van Kuik G.A.M. Multidisciplinary design optimization of offshore wind turbines for minimum levelized cost of energy. *Renewable Energy*, 68:893–905, 2014. DOI: 10.1016/j.renene.2014.02.045.

[38] Buhl T., Gaunna M, Bak C. Potential load reduction using airfoils with variable trailing edge geometry. *Journal of Solar Energy Engineering*, 127:503–516, 2005. DOI:10.1115/1.2037094.

[39] van Wingerden J.W., Hulskamp A.W., Barlas T., Marrant B., van Kuik G.A.M., Molenaar D.P., Verhaegen M. On the proof of concept of a 'smart' wind turbine rotor blade for load alleviation. *Wind Energy*, 11:265–280, 2008. DOI:10.1002/we.264.

[40] Barlas T.K., van Kuik G.A.M. Review of state of the art in smart rotor control research for wind turbines. *Progress in Aerospace Sciences*, 46:1–27, 2010. DOI:10.1016/j.paerosci.2009.08.002.

[41] Lobitz D.W., Veers P.S., Eisler G.R. The use of twist-coupled blades to enhance the performance of horizontal axis wind turbines. Technical Report Draft SAND2001-1303, Sandia National Laboratories, 2001.

[42] Donely P., Shufflebarger C.C. Test of a gust-alleviating flap in the gust tunnel. Technical Report 745, NACA, 1940.

[43] Bielawa R.L. Analytic investigation of helicopter rotor blade appended aeroelastic devices. Technical Report 166525, NASA Ames Research Center, 1984.

[44] Stroub R.H. An analytical investigation of the free-tip rotor for helicopters. Technical Report Tech. Memorandum 81345,, NASA, 1982.

[45] Young L.A. The evaluation of a number of prototypes for the free-tip rotor constant-moment controller. Technical Report Tech. Memorandum 86664, NASA, 1986.

[46] Lambie B., Jain M., Tropea C. Passive camber change for wind turbine load alleviation. In *AIAA Aerospace Sciences Meeting including the New Horizons Forum and Aerospace Exposition*, Orlando, Florida, 2011. DOI:10.2514/6.2011-637.

[47] Arrieta A.F., Bilgen O., Friswell M.I., Hagedom P. Passive load alleviation bi-stable morphing concept. *AIP Advances*, 2, 2012. DOI:10.1063/1.4739412.

[48] Arrieta A.F., Kuder I.K., Rist M., Waeber T., Ermanni P. Passive load alleviation aerofoil concept with variable stiffness multi-stable composites. *Composite Structures*, 116:235–242, 2014. DOI:10.1016/j.compstruct.2014.05.016.

[49] Bottasso C.L., Campagnolo F., Croce A., Tibaldi C. Optimization-based study of bend-twist coupled rotor blades for passive and integrated passive/active load alleviation. *Wind Energy*, 16(8):1149–1166, 2012. DOI:10.1002/we.1543.

[50] Anonymous. *Wind Turbines — Part 1: Design Requirements, Ed. 3*. International Standard IEC 61400-1, 2005.

[51] Anonymous. *Guideline for the Certification of Wind Turbines, Ed. 2010*. Germanischer Lloyd Industrial Services GmbH, Renewables Certification, Brooktorkai 10, 20457 Hamburg, Germany, 2010.

[52] Bottasso C.L., Croce A., Savini B., Sirchi W., Trainelli L. Aero-servo-elastic modeling and control of wind turbines using finite-element multibody procedures. *Multibody System Dynamics*, 16(3):291–308, 2006. DOI:10.1007/s11044-006-9027-1.

[53] Bottasso C.L., Campagnolo F., Croce A., Dilli S., Gualdoni F., Nielsen M.B. Structural optimization of wind turbine rotor blades by multi-level sectional/multibody/3D-FEM analysis. *Multibody System Dynamics*, 32(1):87–116, 2014. DOI:10.1007/s11044-013-9394-3.

[54] Bauchau O.A., Epple A., Bottasso C.L. Scaling of constraints and augmented lagrangian formulations in multibody dynamics simulations. *Journal of Computational and Nonlinear Dynamics*, 4(2), 2009. DOI:10.1115/1.3079826.

[55] Bauchau O.A., Bottasso C.L., Trainelli L. Robust integration schemes for flexible multibody systems. *Comput. Meth. Appl. Mech. Eng.*, 192(3-4):395–420, 2003. DOI:10.1016/S0045-7825(02)00519-4.

[56] Hansen M.O.L. *Aerodynamics of Wind Turbines*. Earthscan, 2nd edition, 2008.

[57] Pitt D.M., Peters D.A. Theoretical prediction of dynamic inflow derivatives. *Vertica*, 5:21–34, 1981.

[58] Peters D.A., He C.J. Finite state induced flow models–part II: Three-dimensional rotor disk. *Journal of Aircraft*, 32(2):323–333, 1995. DOI:10.2514/3.46719.

[59] Kelley N., Jonkman B. NWTC computer-aided engineering tools: Turbsim. ulr: http://wind.nrel.gov/designcodes/preprocessors/turbsim/.

[60] Gill P.E., Murray W.,Wright M.H. *Pratical Optimization*. Academic Press, 1981.

[61] `Matlab`. The MathWorks Inc. www.mathworks.com.

[62] Bottasso C.L., Croce A., Nam Y., Riboldi C.E.D. Power curve tracking in the presence of a tip speed constraint. *Renewable Energy*, 40(1):1–12, 2012. 10.1016/j.renene.2011.07.045.

[63] Bottasso C.L., Croce A. Power curve tracking with tip speed constraint using LQR regulators. Technical Report DIA-SR 09-04, Politecnico di Milano, 2009.

[64] Fingersh L., Hand M., Laxson A. Wind turbine design cost and scaling model. Technical Report NREL/TP-500-40566, NREL National Renewable Energy Laboratory, 2006.

[65] Lindenburg C., de Winkel G.D. Buckling load prediction tools for rotor blades. Technical Report ECN-C-05-103, Energy research Centre of the Netherlands, 2005.

[66] Anonymous. *European Standard Eurocode 3: Design of steel structures - Part 1-6: Strength and stability of shell structures*. European Committee for Standardization, rue de Stassart, 36, B-1050 Brussels, 2007.

[67] Philippidis T.P., Vassilopoulos A.P. Complex stress state effect on fatigue life of GRP laminates. part I, experimental. *International Journal of Fatigue*, 24(8):813–823, 2002. DOI:10.1016/S0142-1123(02)00003-8.

[68] Philippidis T.P., Vassilopoulos A.P. Complex stress state effect on fatigue life of GRP laminates. part II, theoretical formulation. *International Journal of Fatigue*, 24(8):825–830, 2002. DOI:10.1016/S0142-1123(02)00004-X.

[69] Anonymous. *European Standard Eurocode 3: Design of steel structures - Part 1-9: Fatigue*. European Committee for Standardization, rue de Stassart, 36, B-1050 Brussels, 2005.

[70] Hong E.P., You B.J., Kim C.H., Park G.J. Optimization of flexible components of multibody systems via equivalent static loads. *Structural and Multidisciplinary Optimization*, 40(1–6):549–562, 2010. DOI:10.1007/s00158-009-0384-2.

[71] Park G.J. Technical overview of the equivalent static loads method for non-linear static response structural optimization. *Structural and Multidisciplinary Optimization*, 43(3):319–337, 2011. DOI:10.1007/s00158-010-0530-x.

[72] Riboldi C. *Advanced control laws for variable-speed wind turbines and supporting enabling technologies*. PhD thesis, Aerospace engineering, 2012. url:www.politesi.polimi.it.

[73] Géradin M., Cardona A. *Flexible Multibody Dynamics – A Finite Element Approach*. John Wiley & Sons, 1st edition, 2001.

[74] Anonymous. *MD/MSC NASTRAN 2010 Quick Reference Guide*. MSC Software Corporation, 2011.

[75] Laird D., Montoya F., Malcolm D.J. Finite element modeling of wind turbine blades. In *AIAA/ASME Wind Energy Symposium*, volume AIAA-2005-0.195, p. 9–17, Reno, Nevada, USA, 2005.

[76] Resor B. Integrated design and analysis at Sandia. In *2010 Sandia Wind Turbine Blade Workshop*, Albuquerque, NM, USA, 2010. Sandia National Laboratories.

[77] Federov V.A., Dimitrov N., Berggren C., Krenk S., Branner K., Berring P. Investigation of structural behaviour due to bend-twist couplings in wind turbine blades. In *Proceedings of International Conference on Composite Materials ICCM-17*, volume p. 27–31, Edinburgh, Scotland, 2009.

[78] Berry D. and Ashwill T. Design of 9-meter carbon-fiberglass prototype blades: Cx-100 and tx-100. Technical Report SAND2007-0201, Sandia National Laboratories, Albuquerque, NM, 2007.

[79] Chen J., Hallett S., Wisnom M.R. Modelling complex geometry using solid finite element meshes with correct composite material orientations. *Computers & structures*, 88(9):602–609, 2010. DOI:10.1016/j.compstruc.2010.02.004.

[80] Anonymous. *MSC NASTRAN Element Reference Manual*. MSC Software Corporation, 2011.

[81] Piegl L., Tiller W. *The NURBS Book (Monographs and Visual Communications)*. Springer-Verlag, New York, 2nd edition, 1996.

[82] Lee E.T.Y. Choosing nodes in parametric curve interpolation. *Computer-Aided Design*, 21(6):363–370, 1989. DOI:10.1016/0010-4485(89)90003-1.

[83] Anonymous. *MD/MSC NASTRAN 2011 Linear Static Analysis User's Guide*. MSC Software Corporation, 2011.

[84] Drela M. Youngren H. `Xfoil`, subsonic airfoil development system. ulr: web.mit.edu/drela/Public/web/xfoil.

[85] Bishop N.W.M., Sherratt F. *Finite Element Based Fatigue Calculations*. National Agency for Finite Element Methods & Standards (NAFEMS), Great Britain, 2000.

[86] Sullins R.T., Smith G.W., Spier E.E. *Manual for Structural Stability Analysis of Sandwich Plates and Shells*. NASA, Washington DC, USA, Contractor Report NASA CR-1457 edition, 1969.

[87] Bruhn E.F. *Analysis and Design of Flight Vehicle Structures*. Jacobs Pub., 2nd edition, 1973.

[88] `Tcl` developerxchange. www.tcl.tk.

[89] Anonymous. *MD/MSC NASTRAN 2011 MD Demonstration Problems*. MSC Software Corporation, 2011.

[90] Anonymous. *VDI 2230 RICHTLINIEN: Systematic calculation of high duty bolted joints*. Verein Deutscher Ingenieure, Düsseldorf, 2003.

[91] DTU 10MW Reference Wind Turbine Project Site. dtu-10mw-rwt.vindenergi.dtu.dk.

[92] Bak C., Zahle F., Bitsche R., Kim T., Yde A., Henriksen L.C., Andersen P.B., Natarajan A., Hansen M.H. Design and performance of a 10MW wind turbine. *Wind Energy*, 2014. To be accepted.

[93] Hansen M.H., Henriksen L.C. Basic DTU wind energy controller. Technical Report E-0018, DTU Wind Energy, 2013.

[94] Bielawa R.L. *Rotary wind structural dynamics and aeroelasticity*. AIAA Educational series, 1810 Alexander Bell Drive, Reston, VA 20191, 2nd edition, 2006.

[95] Theodorsen T. General theory of aerodynamic instability and the mechanism of flutter. Technical Report 496, NACA, 1935.

[96] Leishman J.G. *Principles of Helicopter Aerodynamics*. Cambridge University Press, Cambridge, England, 2nd edition, 2006.

[97] Theodorsen T., Garrick I.E. Nonstationary flow about a wing-aileron-tab combination including aerodynamic balance. Technical Report 736, NACA, 1942.

[98] Kanda A., Dowell H. Worst-case gust-response analysis for typical airfoil section with control surface. *Journal of Aircraft*, 42(4):956–962, 2005. DOI:10.2514/1.8931.

[99] Karpel M. Design for active and passive flutter suppression and gust alleviation. Technical Report Cont. Rep. 3482, NASA, 1981.

[100] Anonymous. Effect of nose balance on two-dimensional control hinge-moment coefficients. Technical Report ESDU Controls 04.01.03, IHS ESDU, 2003. ulr:https://www.esdu.com.

[101] Soinne E. Aerodynamic and flight dynamic simulations of aileron characteristics. Technical Report 2000-12 ISSN 0280-4646, Department of Aeronautics Royal Institute of Technology, 2000.

[102] Grismer M., Kinsey D., Grismer D. Hinge moment predictions using CFD. In *18th AIAA Applied Aerodynamics Conference AIAA 2000-4325*, Denver, CO, 14-17 August 2000.

[103] Bergami L., Gaunaa M., Heinz J. Indicial lift response function: an empirical relation for finite-thickness airfoils, and effects on aeroelastic simulations. *Wind Energy*, 16:681–693, 2013. DOI: 0.1002/we.1516.

[104] Griffith D.T., Johanns W. Large blade manufacturing cost studies using the Sandia blade manufacturing cost tool and Sandia 100-meter blades. Technical Report SAND2013-2734, Sandia, 2013.